

INFN-12-17(T)/LNF
3rd october 2012

**A STUDY OF MATERIALS USED FOR MUON CHAMBERS AT THE CMS
EXPERIMENT AT THE LHC: INTERACTION WITH GAS, NEW
MATERIALS AND NEW TECHNOLOGIES FOR DETECTOR UPGRADE**

S. Colafranceschi

Abstract

This thesis lays its foundation in both technological and theoretical studies carried out between several aspects of applied engineering. There are several original contributions within the material science. The first is the detailed studies about the CMS RPC gas filters, which required an intense 3 years data-taking and ended up with a complete characterization of purifier materials. On top of this a stable ad – hoc setup (GGM) has been developed for the CMS Experiment in order to monitor the RPC muon chamber working point. Finally a complete new detector has been designed, build and tested using new technology and new electronics establishing the word's record in size for this kind of detector, which is taken under consideration for the upgrade of the high- β region of the CMS Experiment.

A study of materials used for muon chambers at the CMS
Experiment at the LHC: interaction with gas, new
materials and new technologies for detector upgrade

Stefano Colafranceschi

February 16, 2012

Reviewers

Stefano Bianco

Labortori Nazionali di Frascati INFN - Frascati, Italy.

Giovanna Saviano

Università degli studi di Roma - La Sapienza, Rome, Italy.

Archana Sharma

Physics Department, CERN - Geneva, Switzerland.

Day of the defense: 16 February 2012

Abstract

This thesis lays its foundation in both technological and theoretical studies carried out between several aspects of applied engineering. There are several original contributions within the material science. The first is the detailed studies about the CMS RPC gas filters, which required an intense 3 years data-taking and ended up with a complete characterization of purifier materials. On top of this a stable *ad – hoc* setup (GGM) has been developed for the CMS Experiment in order to monitor the RPC muon chamber working point. Finally a complete new detector has been designed, build and tested using new technology and new electronics establishing the word's record in size for this kind of detector, which is taken under consideration for the upgrade of the high- η region of the CMS Experiment.

Preface

The test of all knowledge is experiment. Experiment is the sole judge of scientific truth¹. Science is an enterprise that builds and organizes knowledge in the form of testable explanations and predictions about the world². The source of science is knowledge, but knowledge itself has an undefined nature. To produce knowledge we need experiments, but where do nature's laws come from? In this work I have studied issues, problems and upgrades in the basic and applied physics research field from an engineering point of view. In the former human kind is just led by inspiration and imagination to better understand the universe in which we live; in the latter we look for practical solutions to common problems using the knowledge we have collected in a smart way. On the one hand base physics research is towing technology in order to design and develop more advanced instruments, stronger protocols, more efficiency software and so on.. on the other hands base physics experiments are already making an intense use of the state-of-the-art of the technology, improving it also with the creation of custom applications where needed. Merging knowledge coming from many different areas improves and guides the technological stride, and this is reason why this thesis is focused on both technological and theoretical studies carried out between several aspects of applied engineering. Material Science has been fruitfully applied to the muon system of the CMS (Compact Muon Solenoid) Experiment, located at the LHC (Large Hadron Collider) at CERN, the biggest proton-proton collider ever designed and built up to now. An intensive study has been carried out about materials involved in the "Closed Loop" gas system of the RPC (Resistive Plate Chambers)

¹Feynman, Leighton, Sands. "The Feynman Lectures On Physics", California Institute of Technology, 1964.

²K. Popper, Karl, "The Logic of Scientific Discovery", 1952 New York, NY: Routledge Classics.

installed in CMS, and their upgrade project, which uses new technologies that have been developed and tested.

In the chapter 1 and 2 the Large Hadron Collider (LHC) and Compact Muon Solenoid Experiment (CMS) are introduced underlining the role of Resistive Plate Counters (RPC) detectors within the CMS muon system especially about the gas system showing performance and open problems that are studied in detail in a twin scaled-down setup at the ISR laboratory at CERN Meyrin site. CMS is one of the largest particle physics detectors ever built; it aims to explore physics at the TeV scale, in particular to discover the Higgs boson, to look for evidence of physics beyond the standard model, such as supersymmetry, or extra dimensions to study aspects of heavy ion collisions. Higgs Boson is particularly important because it is the only one missing particle being predicted to exist by the Standard Model (SM) but not yet discovered.

Chapter 3 is the core of the original work carried at the ISR lab where gas system performance, detector behaviour and gas mixture contaminants were kept under control for 3 years with several data-taking setups. The motivation is the basic characterization of purifiers performance along with RPC detector behaviour. Thanks to the intense data-taking, within the thesis activity, we have clarified the role of gas filters and their performance. Moreover in this chapter a new approach based on neural network is introduced as a possible way to model the RPC behavior. This way to build a model could take into account really several parameters such as environmental variables, material properties and gas pollutants. To track and spot gas system contaminants an *ad-hoc* monitoring has been developed: the Gas Gain Monitoring system (GGM). The system aims to recognize any interaction between gas mixture and materials used in the gas system. The GGM system is actually installed at CMS experiment on the surface area (SGX5, the gas building). The GGM has been fully integrated into the CMS Detector Control System (DCS) Experiments and takes care of the CMS RPC muon chamber working point monitoring. The developed software for both the Detector Control System and the analysis tool constitute

an original work performed during this thesis.

Chapter 4 also shows an original and completely new work on a new detector, designed and built in 1 year from scratch. This detector relies on a new technology and the built and working full-size prototype represents the world's record in size at the moment. This detector is a candidate for the CMS muon upgrade in an area where RPC could not sustain the very hard environment in terms of radiation (the high- η forward region). This detector has been fully tested under many point of view in a beam test that successfully ended up with very positive results shown in this thesis. All the developed software and hardware solutions, which allowed the construction and characterization of this prototype, constitute a very original work.

Acknowledgements

This thesis finds base in the teamwork of several groups of people which effectively shared the knowledge and the know-how with each other. In particular the CERN CMS-RPC community, CERN gas group, the L.N.F Frascati equipe, the GEMs for CMS collaboration, the RD51 collaboration and the University of Rome “La Sapienza” heavily contributed in all aspects of this work.

Contents

List of Figures	vii
List of Tables	xv
Glossary	xvii
1 The CMS Experiment and the LHC accelerator	1
1.1 The CMS Experiment	2
1.2 The Large Hadron Collider	5
2 The CMS muon detectors and the RPC detector	9
2.1 The CMS muon System	10
2.2 The Resistive Plate Counters detector, working principle and performance.	12
2.3 Gas purity and RPC behavior	16
2.4 The Closed Loop gas system	18
3 Materials and their interaction with RPC gas mixture	21
3.1 An overview	22
3.2 The scaled-down closed loop experimental setup	24
3.2.1 Motivation	24
3.2.2 Description of involved materials	24
3.2.2.1 Bakelite	24
3.2.2.2 The Zeolite filter	25
3.2.2.3 Metallic filters	28
3.2.2.4 Material and detector quality control	29
3.2.3 Preliminary analysis	31
3.2.3.1 Setting up the chemical setup	31

CONTENTS

3.2.3.2	Filter studies	32
3.2.4	Experimental Setup	35
3.2.4.1	Hardware Setup	35
3.2.4.2	F ⁻ sensors as monitoring device	41
3.2.4.3	Start-up	42
3.2.4.4	The ISR checklists	43
3.2.4.5	Software setup and further developments	44
3.2.5	Results	46
3.2.5.1	RPC performance	46
3.2.5.2	Surface defects	57
3.2.6	Conclusions	59
3.3	A device for monitoring gas-material interactions	61
3.3.1	Introduction	61
3.3.2	Construction and commissioning	62
3.3.3	Software development, Data-Taking and Analysis	69
3.3.4	Results and conclusions	72
3.4	Towards a theoretical model of gas-material interactions	78
3.4.1	Introduction	78
3.4.2	The Artificial Neural Network simulation code	79
3.4.3	Environmental variables and datasets	80
3.4.4	Results	80
3.4.5	Conclusions	90
3.5	A proposal for new materials	91
3.5.1	Introduction	91
3.5.2	Preliminary tests	91
3.5.3	Results	92
3.5.4	Conclusions	94
4	Beyond RPC, Gas Electron Multipliers detector	95
4.1	An overview	96
4.2	Introduction	97
4.2.1	MPGD and GEM detector	98
4.2.2	Double and single-mask technology	101

4.3	Candidate Technology	103
4.4	CMS high- η environment	104
4.5	Small size prototypes	106
4.6	Large detector construction	113
4.6.1	Full-size detector construction - GE11_I (2010)	113
4.6.2	Full-size detector Construction - GE11_II (2011)	118
4.7	The beam test experimental setup	120
4.8	Software Development	124
4.9	Data analysis and performance	127
4.10	Summary and Conclusion	139
5	Conclusion	141
A	RPC Appendix	143
B	Radiation damage	151
C	ISR checklist	155
D	RPC performance during the ISR data-taking	159
	References	169
	Index	174

CONTENTS

List of Figures

1.1	Conceptual design of the CMS Experiment.	2
1.2	Schematic section of CMS Experiment.	4
1.3	A view of LHC with biggest experiments.	5
2.1	Conceptual layout of CMS Experiment	10
2.2	Conceptual layout of a Resistive Plate Chamber.	12
2.3	Conceptual layout of the Resistive Plate Chamber working point.	13
3.1	Bakelite conceptual schema	25
3.2	3D views of Zeolite-A structure.	26
3.3	Zeolite structure showing Van der Waals force (represented as spheres).	26
3.4	Software development for the new RPC cosmic stand.	30
3.5	Element trends in the zeolite purifier.	33
3.6	Pollutants found in the zeolite purifier.	33
3.7	Pollutants found in the zeolite purifier.	33
3.8	Pollutants in the Ni metallic filter.	34
3.9	Pollutants in the Ni metallic filter.	34
3.10	Pollutants in the Ni ₂ Al ₃ metallic filter.	34
3.11	Pollutants in the CuZn metallic filter.	35
3.12	A photo of the ISR Closed Loop test.	35
3.13	The setup of the ISR Closed Loop test.	36
3.14	Schema of adopted filters at ISR Closed Loop gas system	37
3.15	ISR Closed Loop: Chemical setup	38
3.16	Chemical setup sampling points	39

LIST OF FIGURES

3.17	ISR Closed Loop: temperature distribution inside and outside the experimental hut.	40
3.18	ISR Closed Loop: relative humidity inside and outside the experimental hut.	40
3.19	Calibration curves of fluorine monitoring sensors.	42
3.20	Software development at ISR.	45
3.21	Dark currents increase in the up-stream gap and not in the down-stream gap, correlated to the detection of contaminants in gas.	49
3.22	Concentration of Na^+ , Ca^{++} and K^+ in cycle 1-2-3-4 of the first run. . .	49
3.23	F^- production during first run (unused filters) and second run (used filters) 50	
3.24	Concentration of various metallic compounds found in the teflon pre-filter installed in the HV61-62-64-66 during cycle 1-2.	51
3.25	Concentration of various metallic compounds found in the teflon pre-filter installed in the HV61-62-64-66 during cycle 3-4.	52
3.26	Teflon filters contaminants: Ca (first row left), Cu (first row center), Al (first row right), C (second row left) Cu (second row middle) Si, Ca and Al (second row right), Si (Third row left), Ti (third row center), S (third row right).	53
3.27	Total current during all runs with F^- production	55
3.28	Filter performance in run1(red) and run2(black)	56
3.29	Filter behavior comparison	56
3.30	Depolymerized linseed oil, due to aging effects.	57
3.31	Section and prospective view of NaF defect	58
3.32	Dendrite defect $100\mu\text{m}$ and 1mm	58
3.33	Simulation about the effect of a pollutant drop (1mm diameter 0.2mm height) respect to the electrical field inside the RPC 2mm gap.	59
3.34	Layout of GGM experimental setup	61
3.35	A schematic layout of a GGM chamber	63
3.36	Pictures of a GGM gap and chamber. A) A bare gap with the HV and signal cables. B) A completed chamber. The gap is sandwiched between two foam panels and fully covered with a copper shield. C) A section of a chamber with the two foam panels visible.	63

3.37	The electric scheme of the read-out circuit providing the algebraic sum of the two pad signal (PAD + and PAD -).	64
3.38	An oscilloscope screen-shot of the two pad signals (upper traces) which are effected by a coherent noise and are barely visible on the screen. In the lower trace the coherent noise is highly reduced by A3 circuit. The vertical scale is the same for both cases 5 mV/div.	65
3.39	A picture of the GGM system ready to be shipped to CERN. The stack is enclosed into an aluminum box for further shielding.	65
3.40	Typical ADC charge distributions of one GGM chamber at two operating voltages. Distribution (a) correspond to $HV_{eff} = 9.9\text{kV}$ while distribution (b) to $HV_{eff}=10.7\text{kV}$. In (b) is clearly visible the streamer peak around 1900 ADC channels. The events on the left of the vertical line (1450 ADC channels in this case) are assumed to be pure avalanche events.	66
3.41	Efficiency plot (full dots) of GGM chambers as a function of HV_{eff} . The efficiency is defined as the ratio between the number of ADC entries above $3\sigma_{ped}$ and the number of acquired triggers. Open dot plots correspond to the streamer fraction of the chamber signal as a function of HV_{eff}	67
3.42	Average avalanche charge of the eight monitor chamber signal as a function of HV_{eff} . The slope is about 25 ADC ch/10 or 1.2pC/10V. Each point corresponds to 10000 triggers.	68
3.43	Streamer and avalanche yields as a function of HV_{eff} . Each point corresponds to 10000 collected triggers. The solid line has a slope of approximately 130 events/10 V corresponding to a sensitivity of 1.3%/10V.	69
3.44	GGM data flow software and online tools	71
3.45	Stability of GGM against environment variation common to all gaps, such as atmospheric pressure (a), temperature (b), umidity (c). The charge of two gaps is heavily influenced by environment (d, e), while their ratio shows a 2% stability over several weeks (f).	73
3.46	Shift of the working point spotted by the GGM due to a faulty SF ₆ mass flow meter in the main CMS gas mixer.	74
3.47	GGM with HV feedback for stable operation. In black a channel working at $HV=10\text{kV}$, in red a channel working at $HV_{eff} = 10\text{kV}$	75

LIST OF FIGURES

3.48	CMS GGM HV feedback as monitored by the PVSS central application. The upper plot shows the atmospheric pressure and temperature while the bottom plot shows the applied HV (on each RPC) which follows the atmospheric variables.	76
3.49	CMS GGM working point.	77
3.50	Example of a simple Neural Network configuration.	79
3.51	Gap 7 trained on 3 - prevision on period 3	81
3.52	Distribution of error for training for all runs.	82
3.53	Distribution of error for predictions for all runs.	82
3.54	Error for training (left) and prediction (right) for all runs. Gaussian fit superimposed.	83
3.55	(Top) pressure (center) temperature (bottom) humidity versus error $\frac{\Delta Q}{Q}$	84
3.56	Distribution of error as a function of the $\ \mathbf{x}\ $ norm for all runs, six chambers and both training and prediction.	85
3.57	Error $\frac{\Delta Q}{Q}$ vs norm $\ \mathbf{x}\ $ after selection cuts.	85
3.58	Distribution of errors for all norms $\ \mathbf{x}\ $. Gaussian fit superimposed, showing large nongaussian tails.	86
3.59	Period 1 training, prediction on periods 2 and 3.	87
3.60	Period 1 training, prediction on periods 2 and 3, fiducial selection.	87
3.61	Period 1 training, prediction on periods 2 and 3, (left) no cuts, (right) fiducial cut, gaussian fit superimposed.	87
3.62	Period 2 training, prediction on periods 3 and 1.	88
3.63	Period 2 training, prediction on periods 3 and 1, fiducial selection.	88
3.64	Period 2 training, prediction on periods 3 and 1, (left) no cuts, (right) fiducial cut, gaussian fit superimposed.	88
3.65	Period 3 training, prediction on periods 1 and 2.	89
3.66	Period 3 training, prediction on periods 1 and 2, fiducial selection.	89
3.67	Period 3, prediction on periods 1 and 2, (left) no cuts, (right) fiducial cut, gaussian fit superimposed.	89
3.68	Experimental setup for the small high-resistivity bakelite RPC.	92
3.69	Surface plot of the small RPC high-resistivity prototype	93
3.70	RPC prototype with high-resistivity bakelite: I-V plot and the efficiency scan with CMS standard gas mixture.	93

3.71 RPC prototype with high-resistivity bakelite: Efficiency scan with CMS standard gas mixture.	94
4.1 CMS section with designed RPC layers.	97
4.2 Charged particles (hadrons and muons) fluxes in the CMS detector and experimental area. The data are from latest Fluka simulation and correspond to LHC peak luminosity ($10^{34}\text{cm}^{-2}\text{s}^{-1}$).	98
4.3 GEM foil pattern (left), electrical field inside the GEM gap (right).	100
4.4 GEM schema of the working principle.	100
4.5 GE11 prototype chamber, dimensions: $990\text{mm} \times (220 - 455)\text{mm}$	103
4.6 Forward region of the CMS Experiment.	104
4.7 Timing-GEM prototype.	107
4.8 Timing-GEM measured gain with gap configuration 3/1/2/1mm and gas mixture Ar/CO ₂ 70:30.	107
4.9 Timing-GEM measured gain with gap configuration 3/1/2/1mm and gas mixture Ar/CO ₂ /CF ₄ 45:15:40.	108
4.10 SingleMask-GEM measured gain with gap configuration 3/1/2/1mm and gas mixture Ar/CO ₂ 70:30.	108
4.11 single-mask cross section.	109
4.12 GEM with honeycomb structure inserted.	109
4.13 Construction phases of the self-stretched chamber.	110
4.14 Gain curve of self-stretched GEM.	111
4.15 Korean GEM inside the X-rays copper box.	112
4.16 Korean-GEM measured gain Ar/CO ₂ 70:30.	112
4.17 GE1/1 exploded CAD view.	113
4.18 GE1/1 Drift plane under HV test in gas box.	114
4.19 GE1/1 First full-size foil produced.	115
4.20 GE1/1 High Voltage sectors.	115
4.21 GE1/1 Gluing spacers on the foil with the glue gun.	116
4.22 GE1/1 PCB readout plane.	117
4.23 GE1/1 HV divider.	117
4.24 Gap configuration for the full size prototype GE11.II.	118
4.25 GE11.II measured gain Ar/CO ₂ /CF ₄ 45:15:40.	119

LIST OF FIGURES

4.26	RD51 triple-GEM based Tracking telescope.	120
4.27	Total Magnetic field of CMS Endcap.	122
4.28	Radial component of the CMS Endcap Magnetic field.	122
4.29	CMS M1 magnet at the SPS-H2 beam line (Prevessin).	123
4.30	Software Development for Data analysis and quality monitoring.	124
4.31	3D Event Displayer, view of the tracking GEM table and GE1/1 proto- type detector.	125
4.32	Data Quality Monitoring for the Test Beam.	126
4.33	Time resolution of the double mask GEM small prototypes.	127
4.34	Convolution between gaussian time distribution coming from the detec- tor and jitter due to asynchronous beam.	128
4.35	Efficiency comparison: single and double mask technology.	129
4.36	Simulated efficiency with LHC bunch crossing (bx) 25ns.	129
4.37	Honeycomb GEM - Muography at the beam test.	130
4.38	GE11.I Installed at the RD51 H4 experimental beam area showing P1- P3-P5 the sectors fired from the beam line.	131
4.39	Efficiency scan of the GE11.I: P1.	132
4.40	Efficiency scan of the GE11.I: P3.	132
4.41	Efficiency scan of the GE11.I: P5.	132
4.42	Space resolution of the GE11.I: P1.	133
4.43	Space resolution of the GE11.I: P3.	133
4.44	Space resolution of the GE11.I: P5.	133
4.45	GE11.II efficiency performance in the high and low- η	134
4.46	GE11.II performance: space resolution and cluster size in the high and low- η	135
4.47	GE11.II performance inside a strong magnetic field: cluster size.	136
4.48	GE11.II performance inside a strong magnetic field: cluster's displace- ment due to the magnetic field.	136
4.49	Δy distribution for TR_5 and TR_1	137
4.50	Δx distribution for TR_5 and GE11.II.	138
A.1	Tridimensional structure of formaldehyde	145
A.2	Tridimensional structure of Phenol	146

LIST OF FIGURES

A.3	Synthesis of bakelite a) b)	147
A.4	Synthesis of bakelite c) d)	148
B.1	Different ionizing radiations.	152
D.1	Anodic total current Channels 1, 2, 7, 8, 11, 12 in CL during run 1 and 2.	160
D.2	Anodic total current Channels 13, 14, 15, 16, 17, 18 in CL during run 1 and 2.	161
D.3	Anodic total current Channels 9, 10, 19, 21, 22 in OL during run 1 and 2.	162
D.4	Ohmic current Channels 1, 2, 7, 8, 11, 12 in CL during run 1 and 2. . .	163
D.5	Ohmic current Channels 13, 14, 15, 16, 17, 18 in CL during run 1 and 2.	164
D.6	Ohmic current Channels 9, 10, 19, 21, 22 in OL during run 1 and 2. . .	165
D.7	Signal current Channels 1, 2, 7, 8, 11, 12 in CL during run 1 and 2. . .	166
D.8	Signal current Channels 13, 14, 15, 16, 17, 18 in CL during run 1 and 2.	167
D.9	Signal current Channels 9, 10, 19, 21, 22 in OL during run 1 and 2. . .	168

LIST OF FIGURES

List of Tables

2.1	RPC requirements	14
3.1	Chemical setup summary flasks	31
3.2	Preliminary results from efficiency analysis of the chemical setup	32
3.3	Summary table of Closed Loop (CL) and Open Loop (OL) channels. . .	47
3.4	Summary table of Closed Loop (CL) and Open Loop (OL) channels. . .	48
3.5	NN analysis: periods summary table	81
3.6	Synopsis of selection cuts for fiducial volume.	86
3.7	Summary of errors σ_{fwhm} and nongaussian tails (ngt) for various selection cuts and samples.	90
C.1	ISR checklist - Chemical parameters	156
C.2	ISR checklist - Rack parameters	157
C.3	ISR checklist - Chamber values	158

LIST OF TABLES

Glossary

ADC	Analog-to-digital-Converter	GGM	Gas Gain Monitoring System
ALICE	A Large Ion Collider Experiment	IP	Intersection point
ANN	Artificial Neural Networks	ISR	Intersecting Storage Rings
ASIC	Application Specific Integrated Circuit	LEP	Large Electron Proton collider
ATLAS	A Toroidal LHC Apparatus	LEP	Large Electron-Positron collider
CMS	Compact Muon Solenoid	LHC	Large Hadron Collider
CSC	Cathode Strip Chambers	LHCb	LHC beauty experiment
DAQ	Data Acquisition	LINAC	Linear particle Accelerator
DCS	Detector Control System	MPGD	Micro Pattern Gas Detector
DQM	Data Quality Monitoring	NFS	Network File System
DT	Drift Chambers	PAW	Physics Analysis Workstation
GEM	Gas Electron Multipliers	PS	Proton Synchrotron
		PSB	Proton Synchrotron booster
		QDC	Charge-to-digital Converter
		RPC	Resistive Plate Chamber
		SOAP	Simple Object Access Protocol
		SPS	Super Proton Synchrotron
		TDC	Time to Digital Converter
		VFAT	Very Forward Atlas and Totem

LIST OF TABLES

1

The CMS Experiment and the LHC accelerator

1. THE CMS EXPERIMENT AND THE LHC ACCELERATOR

1.1 The CMS Experiment

The CMS Experiment(1) is a huge general purpose particle detector in operation at the LHC proton-proton collider at CERN. A conceptual design is shown in the Fig. 1.1, the greatness comes from the fact that the overall dimensions of CMS are just huge. CMS is 21.6m length with a diameter of 14.6m and a total weight of 12500 tons; each piece and each subsystem was produced and commissioned on the surface and subsequently let down in the cavern located 100m underground. CMS is made of several subsystems in order to achieve the prefixed very ambitious scientific program; these subsystems were fully commissioned in 2007 after several years of designing and building.

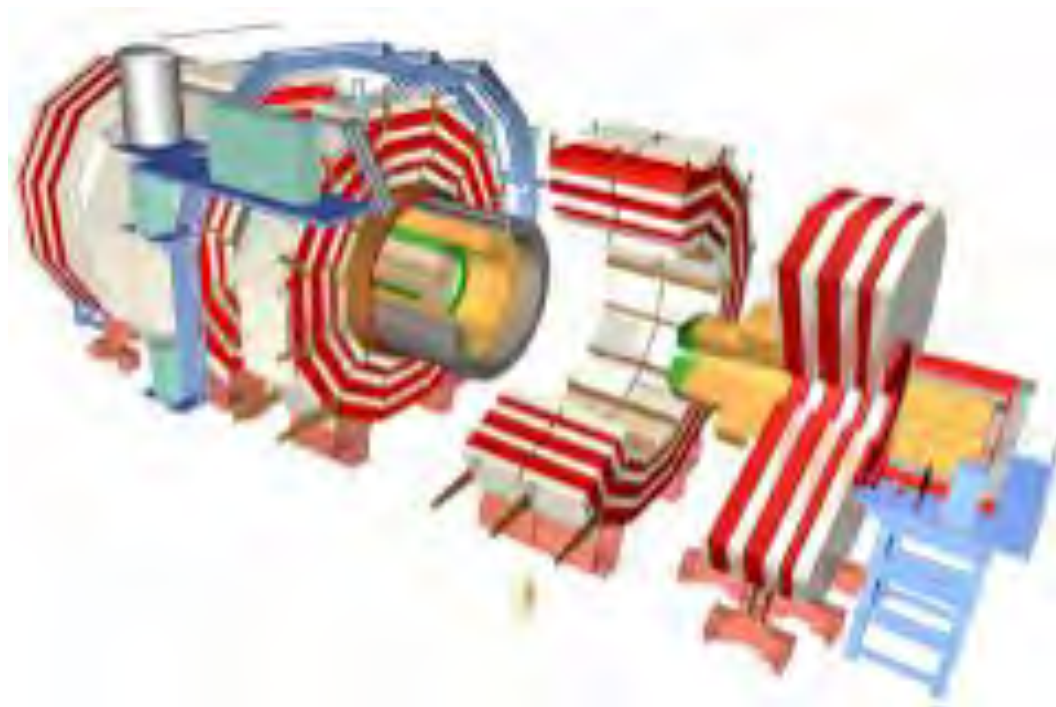


Figure 1.1: Conceptual design of the CMS Experiment.

The superconductive barrel solenoid (Fig. 1.1 dark grey) is playing a key role in the CMS acronym but not only, in practical terms the solenoid is providing a strong magnetic field of 4T; on the other hand the magnetic return yoke (Fig. 1.1 red) is the core of the mechanical structure. Besides in CMS a very wide variety of detector and technologies take place such Pixels (70M channels), Silicon strips (10M channels),

ECAL (76k lead tungstate crystals), HCAL, RPCs (800 chambers), DTs, CSC.

The Trigger is very complicated, at CMS two main levels are employed. The Level-1 Trigger (L1) is implemented using custom hardware processors and is designed to reduce the event rate to 100kHz during LHC operation using information from the calorimeters and the muon detectors. It operates nearly deadtime-free and synchronously with the LHC bunch crossing frequency of 40MHz. The High Level Trigger (HLT) is implemented across a large cluster of commodity computers referred to as the event filter farm, and provides further rate reduction to about 100Hz using filtering software applied to data from all detectors at full granularity.

Outside the magnetic solenoid, for what concerns the muon system, there are 4 stations of RPC and CSC in both barrel and endcap and DT only in the barrel. The muon particle is playing a key role in CMS, the detection of muons is thought to be a sort of signature of interesting processes, that have muons in the final state; this is an example with a candidate channel decay for the Higgs boson H^0 into two Z^0 and finally muons:

$$pp \longrightarrow H^0 \longrightarrow Z^0 Z^0 \longrightarrow \mu^+ \mu^- \mu^+ \mu^-$$

For this reason the muon system is the core of the CMS experiment. The muon detection is performed with RPCs, CSC and DT; three kind of gaseous particle detector that work together in a robust framework covering about 25000m² of detection planes shaped around the solenoid magnet. The muon system is composed by two parts, the barrel and the endcaps. In the Barrel there are five wheels divided in twelve sectors (Wheel +1, Wheel +2, Wheel0, Wheel -1, Wheel -2) and in the endcaps there are four disks (ME1, ME2, ME3, ME4).

1. THE CMS EXPERIMENT AND THE LHC ACCELERATOR

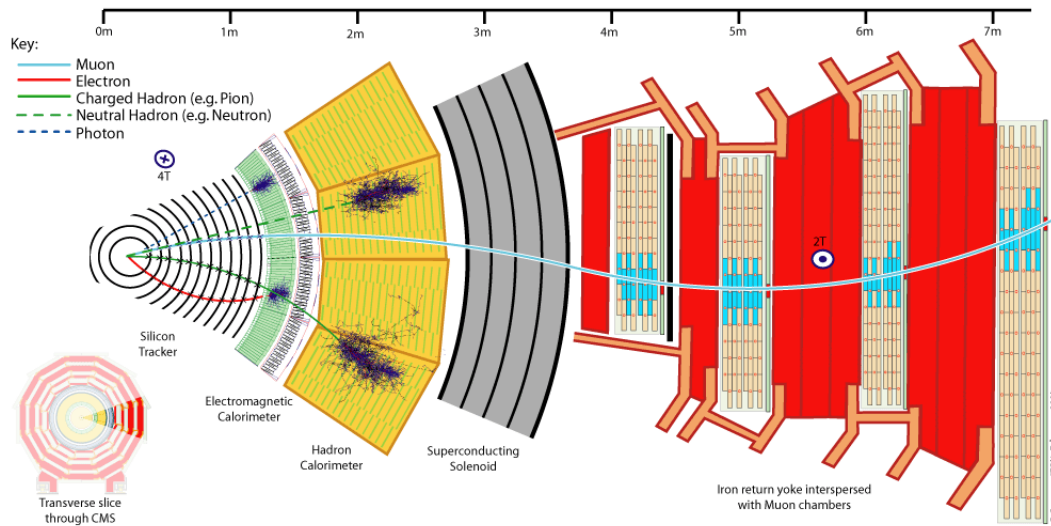


Figure 1.2: Schematic section of CMS Experiment.

In the Fig. 1.2 a transversal section of the CMS Experiment is presented. As usual in the HEP Experiment each layer of a detector is supposed to perform a detection, the overall system itself is also redundant. The muon detection is the last layer, being the muon particles not used to interact with matters the muon system contributes in a very important way to establish the trigger for all other sub-detectors.

1.2 The Large Hadron Collider

The Large Hadron Collider (LHC), in Fig. 1.3, is the largest and most powerful proton-proton (ion-ion) collider ever built. It has been built at CERN in the same tunnel where the LEP (Large electron-positron collider) was installed in 1984. The tunnel is 27km long and is situated 100m underground the Franco-Swiss border near Geneva. LHC uses two superconductive rings to accelerate and collide two proton beams with the scope to answer many of the fundamental questions of physics still open like the nature of the mass, the existence of super symmetry particles and eventually new physics.



Figure 1.3: A view of LHC with biggest experiments.

According to the technical design LHC should have operated with two proton beams of 7TeV at the luminosity of $10^{34}\text{cm}^{-2}\text{s}^{-1}$, nowadays the machine is in operation at lower energy due to a serious accident occurred on 19 September 2008. That day, after 9 days of operation, six tonnes of liquid Helium come out from the cooling plant for a faulty electrical connection, the explosion was so intense that several magnets, 10 tons each, were displaced from their original position; this catastrophic event delayed LHC operation of 1 year. Anyway on 30th March 2010 LHC was able to collide two beams with a total energy of 7TeV which is considered an energy enough safe that should avoid the risk of having further problems while still being high enough to provide good data for Higgs and supersimmetry discovery.

Two transfer tunnels, each approximately 2.5km in length, link the LHC to the CERN accelerator complex that acts as injector. In fact LHC relies on a chain of several particle accelerators, from the protons source to the final step (accelerated

1. THE CMS EXPERIMENT AND THE LHC ACCELERATOR

proton beams); LINAC2, PS, PSB, SPS are used to accelerate and inject proton bunches into LHC machine. The protons originate in a 92keV duoplasmatron source, fed with H_2 gas, yielding a 300mA beam current. The protons from this source are collected as an input to LINAC2, which increases their energy up to 50MeV. This LINAC supplies the PSB with protons for an increase in energy up to 1.4GeV. All protons are then accelerated by the PS, up to 25GeV and subsequently by the SPS, up to 450GeV. The final step of beams acceleration, takes place in LHC. It consists of two circulating beams in separate vacuum chambers which are horizontally spaced by 194mm. Only at about 100m before the interaction point (IP), the two beam pipes join into a single piece. Thanks to 8 resonant cavities, these two pulsed beams are accelerated up to 7TeV. The beams are steered by 1232 cryogenic dipole magnets with a field of $B = 8T$, these dipoles are immersed in a pressurized bath of super-fluid Helium at 1.9K to maintain a superconducting state, storing an energy of about 600MJ.

On the LHC track (shown in Fig. 1.3) four big experiments: ATLAS, ALICE, CMS and LHCb were installed and are at the moment in operation in the relative interaction points. After many years of commissioning with cosmic rays, the intense data-taking started since December 2009 when LHC began delivering collisions. The two LHC symmetrical rings are divided into eight octants and arcs and eight straight sections approximately 528m long; the two high luminosity experimental insertions are located at diametrically opposite straight sections: the ATLAS experiment is located at Point 1 and the CMS experiment at Point 5. The other two large experiments, ALICE and LHCb, are located at Point 2 and at Point 8. The remaining four straight sections do not have beam crossings. The two beams are injected into the LHC in two different octants, octant 2 and octant 8 respectively for clockwise and anticlockwise beam. The octants 3 and 7, instead, contain two collimation systems for the beam cleaning.

The physics programmes of CMS and ATLAS are very broad, ranging from precision electroweak measurements to the potential discovery of a rich zoology of new particles predicted by theories of physics beyond the Standard Model. With two different detector designs and different approaches to data analysis the CMS and ATLAS collaborations will be able to cross-check each others results and to ensure the redundancy of their measurements. LHCb will study CP violation through b-quark physics and make precision measurements of rare decays. ALICE has been designed to study

1.2 The Large Hadron Collider

the physics of heavy ion collisions in specialized LHC runs with beams of lead and gold nuclei.

1. THE CMS EXPERIMENT AND THE LHC ACCELERATOR

2

The CMS muon detectors and the RPC detector

2. THE CMS MUON DETECTORS AND THE RPC DETECTOR

2.1 The CMS muon System

The muon system is one of most important part of the CMS detector. It has been designed to detect, and fast trigger, muons in a redundant way. The muon identification and their momenta measurement rely on three types of gaseous detection technologies: Drift Tubes (DT), Cathode Strip Chambers (CSC) and Resistive Plat Chambers(2) (RPC). The DTs are used for precise trajectory measurements in the central Barrel region where neutron background is quite small $1 - 10\text{Hz}/\text{cm}^2$, while the CSCs are used in the Endcaps where the background rate is around $1\text{kHz}/\text{cm}^2$ and the magnetic field is also more intense than in the barrel. The RPCs provide a very fast and accurate ($\approx 1\text{ns}$) time measurement signal when a muon passes through them; they are installed in both the barrel and the Endcaps.

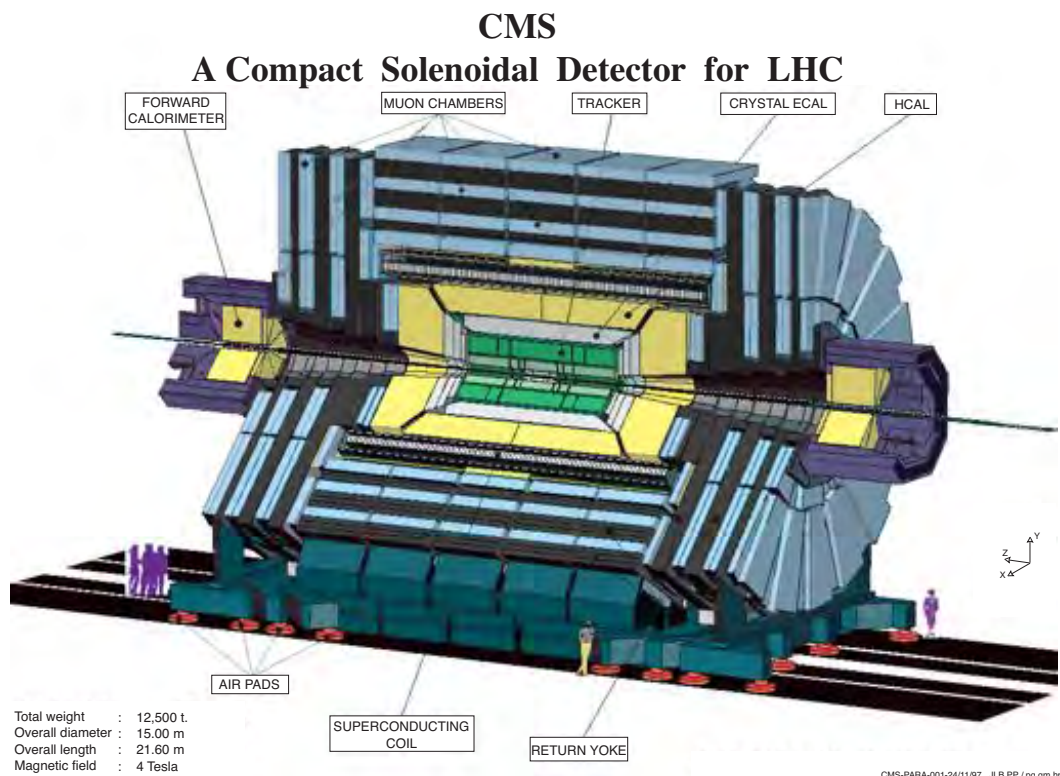


Figure 2.1: Conceptual layout of CMS Experiment

The muon system can be divided into two sub-systems: the Barrel (Fig. 2.1) and two Endcaps. Moreover each sub-system has been assembled in wheels and disks. In particular, the Barrel is composed by 5 independent wheels geometrically segmented into 12 sector, each one containing 4 RPC layers. The second and third layer are equipped with RPC chambers, the last layer is staged, the chamber production is in the starting phase and part of this thesis is devoted to the quality control of materials involved in the new designing and construction of this last RPC layer. The first layer, on the contrary, will be never installed due to many concerns about performance of RPC chambers located in the high- η region, part of this thesis is devoted to the material and technology development of a new large size GEM detector (Chapter) which could sustain operation at high- η and at the same time provide same performance of foreseen RPCs.

2. THE CMS MUON DETECTORS AND THE RPC DETECTOR

2.2 The Resistive Plate Counters detector, working principle and performance.

The Resistive Plate Chambers are gaseous detectors able to detect charged particles thanks to the ionization of the gas mixture that flows inside the chamber themselves. They are widely and extensively employed in many particle physics experiments to detect high energy charged particles especially fast muons; some important features consist in an excellent time resolution along with reasonable space resolution and high rate capability, high gain, simple electronics, robustness and low cost. Thanks to these properties RPCs were adopted at LHC experiments such as CMS(3) and ATLAS(4) covering a total area of 6500m²; on the other hand in big cosmic-ray experiments like ARGO YBJ(5), these RPC chambers arrive covering some km² showing that large area of these developed detectors will make this technology feasible for use in high resolution imaging(6) and tomography as well with a reasonable low budget.

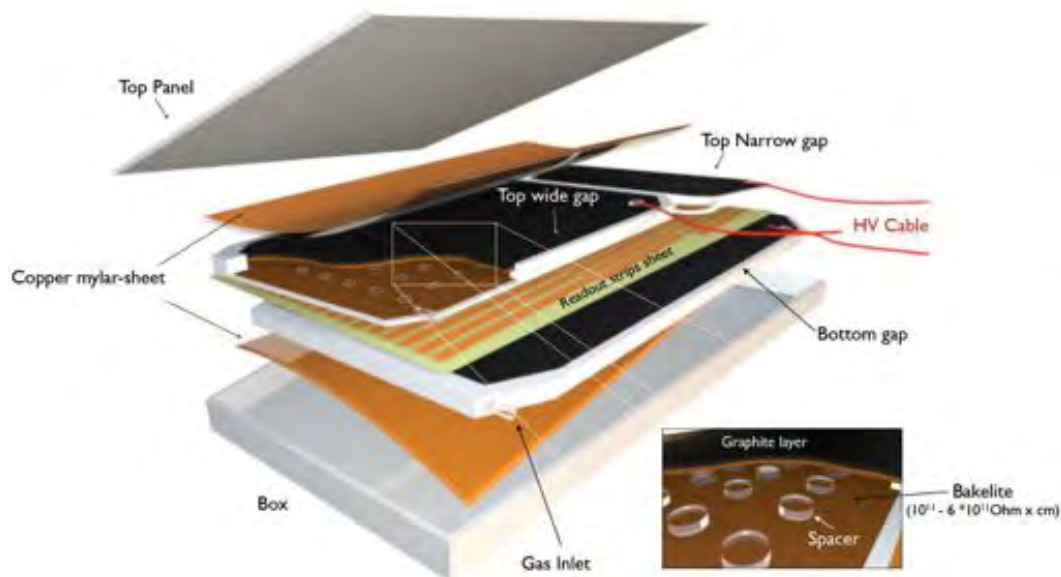


Figure 2.2: Conceptual layout of a Resistive Plate Chamber.

The constituent elements of RPCs are two parallel electrodes, high-resistivity bakelite (discussed in details in sect. 3.2.2.1) plates between which, in a 2mm gap, a gas mixture at ordinary pressure is circulated. A 9.0-10.0kV voltage drop is applied be-

2.2 The Resistive Plate Counters detector, working principle and performance.

tween plates on the outer bakelite surfaces that are coated with graphite to equalize the inner electrical field since bakelite is not conductive.

RPCs use a fluorine-based gas mixture whose main component is Freon. At CMS experiment RPCs are double gap bakelite based chambers; every single gap is formed by two thin bakelite electrode plates with a bulk resistivity of 10^{10}Ohm/cm . These two plates are maintained at a distance of 2mm with plastic (polycarbonate) spacers according to a $10 \times 10\text{cm}^2$ mesh. A ‘‘Double gap’’ is formed with two single gaps placed one on top of the other separated only by a common read-out copper stripped plane. At CMS Experiment the gas composition is 95,2% Freon, 4,5% Isobutane, 0,3% SF_6 and inside the chamber is applied a strong electrical field generated by high voltage (HV) applied, typically 9.4kV, to the two resistive bakelite based electrodes.

The bakelite is the most common material used in the RPCs, it is a composite material made by plastic laminate, cotton and paper fibers and phenolic resin. Thanks to the polymerization of phenolic resin the bakelite has a rigid mechanical structure. Several problems related to the quality control regards the bakelite panels, which due to their nature are difficult to produce identically with same characteristic, this is the reason why every single panel has to be carefully checked in terms of bulk and surface resistivity before any application. In the Fig. 2.2 it is shown a conceptual layout of an RPC chamber.

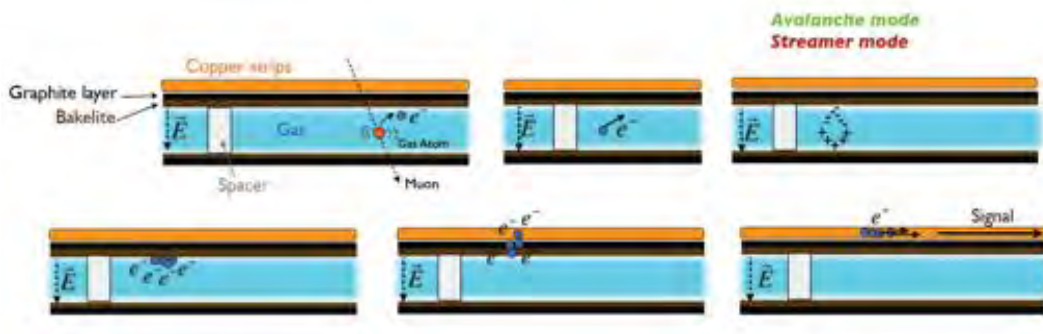


Figure 2.3: Conceptual layout of the Resistive Plate Chamber working point.

The bakelite inner surface is treated with linseed oil to make the surface smooth without defects. In the past it was demonstrated(7) that this treatment decreased the dark current by factor 3 and the single rate by factor 10. The RPC gap is 2mm thick

2. THE CMS MUON DETECTORS AND THE RPC DETECTOR

Table 2.1: RPC requirements

Item	CMS requirement
Time resolution	2ns
Efficiency	> 95%
Rate capability	1kHz/cm ²
Intrinsic noise rate	5Hz/cm ²
Operational environmental humidity	< 40 – 50%
Operational environmental temperature	< 19 – 22°C
Streamer probability	< 10%
High Voltage Plateau	> 300V

and is filled with the gas mixture, thanks to the HV applied, an avalanche¹ signal (as in Fig. 2.3) is generated if a charge particle pass through the chamber. This signal is transferred to copper strips, installed on a separate layer (insulated from graphite by means of Mylar), and with sufficiently fast front-end electronics the signal can be used as a trigger. Each chamber is divided into four η -partitions and each one has independent strips and independent electronics. The front-end boards receive signals from the readout and send LVDS signals to the CMS logic units, called link-board.

RPCs are chosen in the muon system at CMS because they can combine an adequate spatial and time resolution comparable to that of scintillators (order of ns) but using relatively simple technology and inexpensive materials. The table 2.1 shows a summary of requirements for RPC at CMS.

To achieve these performance RPC are working in avalanche mode that ensures few deposit charge on electrodes, fast signals and short dead time. For these reasons a very good front-end electronics is required to handle with signals of amplitude of few pC. The incredibly fast signal makes the RPC capable of tagging the time of an ionizing event in a much shorter time than the 25ns between two consecutive LHC bunch crossings. In the Barrel 480 rectangular RPC chambers were installed between 7

¹The electron avalanche is a process in which a number of free electrons in a medium, usually gas, are subjected to strong acceleration by an electric field, ionizing the medium's atoms by collisions. Thereby forming "new" electrons to undergo the same process in successive cycles. Electron avalanches are essential to the dielectric breakdown process within gases. The process can culminate in corona discharge, streamers, in a danger spark or in a continuous arc that maybe completely short the gap.

2.2 The Resistive Plate Counters detector, working principle and performance.

wheels (W-2, W-1, W0, W+1, W+2); each wheel is then divided into 12 sectors (such as the clock numbers) and 6 layers. The trigger algorithm is designed to be efficient with only four station, for redundancy reasons there are two more stations. RPCs are really fundamental for CMS, for the muon detection; the choice of RPC is based on the fact that this detector is very reliable, in fact due to mechanical constraints at CMS is not simple at all to replace a chamber, even if it could be possible a short a localized intervention in the foreseen maintenance period. The basic idea is that such a detector installed at CMS has to be reliable without any problem for a long time, orders of tens of years. However RPCs, as other gas detectors, are suffering aging if irradiated with high particle flux. Even if RPCs stand very well the aging process, still a decreases of performance is expected in several years of operations. Another critical factor is the gas quality that, specially if the gas is recirculating, can damage the bakelite surface collecting contaminants like radicals and pollutants that damage the inner surface modifying the electrical field distribution up to destroy region of the chamber; these mechanisms will be discussed in the chapter 3.

2.3 Gas purity and RPC behavior

The gas mixture contamination is really danger for the RPC detectors. The reason why the gas mixture contamination is utmost important is related to the very strong field present in the gas gap chamber. Any surface defect of the bakelite due to some contaminant will affect locally the electric field creating the possibility to have sparks. Fundamentally a different gas mixture can shift the working point of a gas detector and even completely change the behavior response of the detector itself.

Due to the large gas volume and high costs, the RPC detectors, in CMS, use a recirculation gas system ("Closed Loop") with gas purifiers. This configuration places a big issue concerning the fact that small amount of pollutants could be collected into the Closed Loop up to certain values which could represent a dangerous concentration. The absence of gas contaminants(8), (9) is of paramount importance in all gas detectors, but specially in RPC detectors where a fluorine-based gas mixture has been adopted it is mandatory to keep the gas as much as possible clean due to the high reactivity of the F^- ions created inside RPC chambers during their operations. At the moment CMS is using purifiers with an unclear performance and characterization, therefore the Closed Loop recirculation mode, at certain stages, might be critical to operate: the solution that has been found relies on a very frequent replacement of the filters cartridges.

The F^- contamination starts inside the chamber during the normal operation of the RPC detector. Due to the high voltage applied, and the consequent ionization inside the gas mixture there are several chemical aspect to be considered, for example the HF produced by SF_6 or $C_2H_2F_4$ molecular breaks-up and generates further fluorine recombinations. In fact, during the ionization process, the Freon based gas mixture can create free radicals, as the fluorine, that can react with the bakelite modifying the mechanical and physical properties of the resistive electrodes. This alteration most likely regards the surface and could be not reversible causing the death of the chamber. Besides, it is not trivial task to make a theoretical model of these reactions due to the fact that it is necessary to take into account many variables which concern the gas and the mechanical properties. To manage with this intricate situation, a system purifier has been developed starting with a general purpose purifier configuration to ensure clean gas mixture in the Closed Loop system.

2.3 Gas purity and RPC behavior

The operation of the CMS RPC system is strictly correlated to the ratio of the gas components, and to the presence of pollutants that can be produced inside the gaps during discharges, accumulated in the Closed Loop, or by pollution that can be present in the gas piping system (tubes, valves, filters, bubblers, etc.) and flushed into the gaps by the gas flow. Therefore is utmost mandatory a monitoring of the presence of these contaminants, as well as the gas mixture stability to avoid an RPC working point shift, damages and to ensure thee overall correct functionality. For these reasons in the Sect 3.3 it is described an online monitoring system developed within this thesis for the CMS experiment.

2.4 The Closed Loop gas system

CMS has adopted a Closed Loop gas system, this system is providing gas to hundreds of chambers, the whole volume is around 16m^3 . In the ISR laboratory, at the Meyrin CERN site, it was installed a twin Closed Loop gas system equipped with several devices such as GasChromatograph (GC), chemical sampling points, and big hut containing working RPC detectors with cosmic rays. The ISR gas system is composed of a mixer that combine the three main components: 1,1,1,2-Tetrafluoroethane (CH_2FCF_3), Isobutane (C_4H_{10}) and Sulfur hexafluoride SF_6 ; two racks are dedicated to the Closed Loop gas operation with a pump, flow meter controls and humidifiers for the closed and open loop mode. In one rack of the ISR gas system, scaled-down standard CMS filters are installed; these purifiers are filled with the same material present at CMS. Close to the gas racks eleven double gaps are installed in an hut which is kept under controlled environment: temperature is maintained at $20 \pm 1^\circ\text{C}$ and relative humidity at $40 \pm 5\%$ during all seasons of the year by means of an air conditioning unit, dehumidifier and humidifier. In the Closed Loop system three filters were adopted; this combination was designed by a task force, years ago, who established an experimental setup to test performance filters. The first filter is a molecular sieve made with Zeolite 90% 3A, and Zeolite 10% 5A. The second and third filter are metallic based. The second filter is made of copper for 50% and copper/zinc for the rest (R3 11G BASF e R3 12 BASF). The third filter is filled with nickel and aluminium (6625 Leuna). From the chemical point of view filters were thought to remove oxygen and water. Chemical aspects involved in the gas purification are still not well understood and object of this thesis is to characterize filters performance in terms of lifetime and efficiency. One of the main issue of the Closed Loop test is to evaluate purifiers lifetime and efficiency after regeneration process. This is fundamental for the CMS experiment in order to have an efficient schedule of the purifier material replacement and regeneration.

The main goal remains to operate the RPC chambers in a reliable and safe way, so purifiers must be always efficient and in operation without suffering any saturation effect.

Bakelite is a composite material that “feels” the gas mixture, it has been observed that used bakelite has less amount of Cu, Ni, As, Cr, e Sb elements that go in the

2.4 The Closed Loop gas system

gas mixture due to complex chemical reactions. The other point is that bakelites are damaged by heavy metal and HF.

2. THE CMS MUON DETECTORS AND THE RPC DETECTOR

3

Materials and their interaction with RPC gas mixture

3. MATERIALS AND THEIR INTERACTION WITH RPC GAS MIXTURE

3.1 An overview

This chapter illustrates detailed studies on materials involved in the CMS RPC gas system. Obtained results consist in a complete behavior characterization of CMS RPC gas filters and detector response in presence of gas contaminants. Original results show important consequences on the RPC operation considering gas and material parameters. Several experimental setups were kept under control for long-time data-taking; this implied software development and maintenance and *ad – hoc* tools written for the data-analysis.

In the Sect. 3.2 the scaled-down Closed Loop experimental test is described detailing the hardware and software setup (Sect. 3.2.4), explaining preliminary considerations about main involved materials (Sect. 3.2.2) and finally showing the obtained results in the Sect. 3.2.5. This test was aiming to study gas-RPC material interactions in a clone CMS closed loop gas system. For more than 2 years an intense data-taking has been faced collecting a really important and complete dataset which includes RPC performance data, environmental variables and chemical analysis.

Moreover in the Sect. 3.3 the Gas Gain Monitoring system (GGM) is introduced underlining the original work that has been performed within this thesis for the CMS Collaboration. The GGM is an online monitoring for CMS and actually its scope is to spot and track possible contamination of the CMS gas system. With the GGM we have developed a system that can immediately recognize interactions between materials present in the gas system (gas lines, filters and several other devices) with the RPCs. The GGM software framework has been developed in order to work inside the CMS environment, moreover we have integrated the GGM into the main Detector Control System (DCS) of the CMS Experiment so that this online monitoring is fully visible to the shifter and easily accesible remotely. Further details about the software development will be discussed in the Sect. 3.3.3

In Sect. 3.4 a new theoretical approach has been invented to model the RPC behavior. This model has been validated with environmental variables only, but the approach is quite generale and flexible since it uses neural network. So given this way to study the problem more parameters could be added to the model in order to enlarge the phase-space where the model can predict correctly RPC behavior.

Finally in Sect. 3.5 new bakelite material is presented delivering innovative ideas in this field. This new material has been tested experimentally with very positive results with cosmic rays at the ISR laboratory.

3. MATERIALS AND THEIR INTERACTION WITH RPC GAS MIXTURE

3.2 The scaled-down closed loop experimental setup

3.2.1 Motivation

The Resistive Plate Counters (RPC) (10) are part of the muon spectrometer of the Compact Muon Solenoid (CMS) Experiment(1). RPCs utilize a gas recirculation system called “Closed Loop” (CL) (11), (12) to cope with large gas mixture volumes and costs.

A systematic study of Closed Loop gas purifiers has been carried out since 2008 at the ISR experimental area of CERN with the use of RPC chambers exposed to cosmic rays with currents monitoring and gas analysis(13) performed in several sampling points. Goals of the study(14) were to observe the release of contaminants in correlation with the dark current increase in RPC detectors, to measure the purifier lifetime, to observe the presence of pollutants and to study the regeneration procedure. Previous results had shown the presence of metallic contaminants, and an incomplete regeneration of purifiers(15).

3.2.2 Description of involved materials

3.2.2.1 Bakelite

Bakelite is a kind of hard mouldable plastic, widely used in several different fields. Dr. Leo Baekeland¹ after a long investigation about reactions of phenol and formaldehyde managed to obtain a tough, light, rigid and chemically resistant solid from two inexpensive ingredients. He presented this new material at the American Chemical Society in 1909²; the patent was then deposited few years later (Patent1233298, 17 July 1917). In the Appendix bakelite is described in depth.

The RPCs are made of bakelite, the Fig. 3.1 shows the schema of one bakelite sheet to be used for RPCs. More information about the RPC working principle are discussed in Sect. 2.2.

A single gap RPC is made of two sheet of the bakelite (shown in Fig. 3.1) kept at 2mm distance with plastic spacers. The area in between spacers is filled with a gas mixture which acts as ionizing gas. Bakelite resistivity is utmost important and, during the production, one must keep under control several parameters to tune the resistivity

¹Amato Ivan (29 March 1999). "Leo Baekeland". Time 100. TIME.

²"New Chemical Substance". The New York Times. February 6, 1909.

3.2 The scaled-down closed loop experimental setup

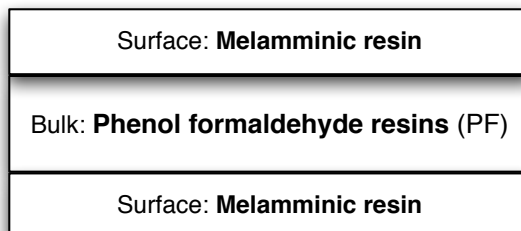


Figure 3.1: Bakelite conceptual schema

to the correct value since, as already discussed in the Sect. 2.2, the resistivity affects the chamber operation.

3.2.2.2 The Zeolite filter

Zeolites are microporous, aluminosilicate minerals commonly used as commercial general purpose adsorbents. The general formula of Zeolites is:



The term Zeolite was originally coined in 1756 by Swedish mineralogist Axel Fredrik Cronstedt, who observed that upon rapidly heating the material stilbite, it produced large amounts of steam from water that had been adsorbed by the material. Based on this, he called the material Zeolite, from the Greek ζέω (zeo), meaning "boil" and λίθος (lithos), meaning "stone". The interest on Zeolites is constantly increasing; they are widely used in many different things, especially by industries for example as molecular sieve for gas purifiers. The Zeolite porous structure can accommodate a wide variety of cations as for example Na^+ , Ca^{++} , Mg^{++} . These elements are then mechanically trapped into the Zeolite sieve. This term refers to the ability of selecting molecules by their size. This is due to a very regular pore structure of molecular dimensions as in Fig. 3.2 and Fig. 3.3.

3. MATERIALS AND THEIR INTERACTION WITH RPC GAS MIXTURE

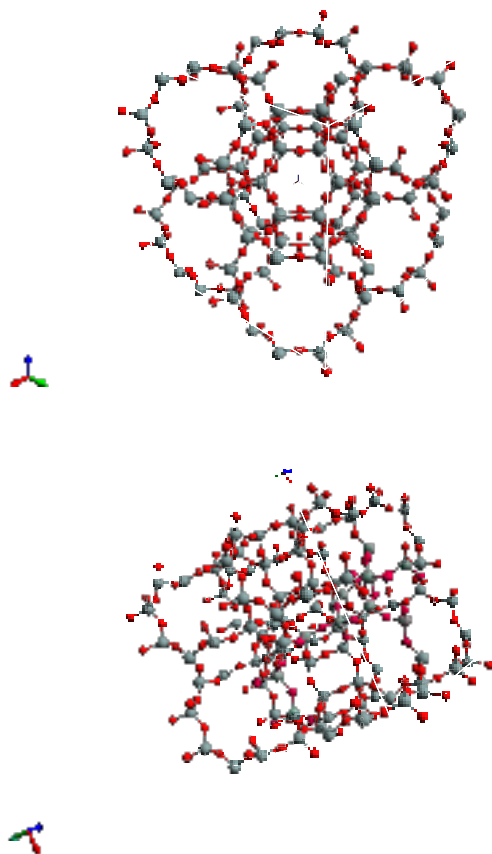


Figure 3.2: 3D views of Zeolite-A structure.

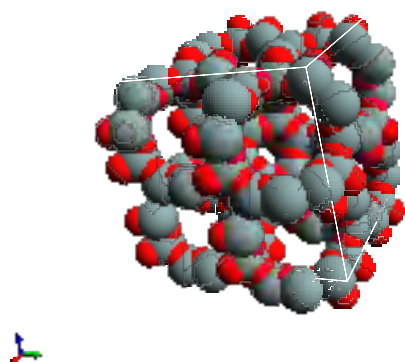


Figure 3.3: Zeolite structure showing Van der Waals force (represented as spheres).

3.2 The scaled-down closed loop experimental setup

The maximum size of the molecular or ionic species that can enter the pores of a Zeolite is controlled by the dimensions of the channels conventionally defined by the ring size of the aperture. Natural Zeolites are limited in number (40 known structures) and normally are contaminated by other minerals. One of the most common process from where the natural Zeolite comes, consists in the reaction of volcanic rocks, ash layers and alkaline groundwater. On the contrary there are much more than hundreds types of synthetic Zeolite that can be produced by a process of slow crystallization of a silica-alumina gel in the presence of alkalis and organic templates. Synthetic Zeolite clearly have several advantages over their natural analogs, in fact from the artificial synthetic process it is easy to obtain an uniform, phase-pure state. Moreover it is possible to design Zeolite structure which does not exists in nature. One of the important processes used to carry out Zeolite synthesis is sol-gel processing. The product properties depend on reaction mixture composition, pH of the system, operating temperature, pre-reaction 'seeding' time, reaction time as well as the templates used. In sol-gel process, other elements (metals, metal oxides) can be easily incorporated. The silicalite sol formed by the hydrothermal method is very stable. Also the ease of scaling up this process makes it a favorite route for Zeolite synthesis.

Due to the presence of alumina, zeolites exhibit a negatively charged framework, which is counter-balanced by positive cations resulting in a strong electrostatic field on the internal surface. These cations can be exchanged to ne-tune the pore size or the adsorption characteristics. For instance, the sodium form of zeolite type A has a pore opening of approximately 4\AA , and it is called called a 4A molecular sieve. If the sodium ion is exchanged with the larger potassium ion, the pore opening is reduced to approximately 3\AA . Calcium ion could replaces two sodium ions, thus, the pore opening increases to approximately 5\AA . Ion exchange with other cations is sometimes used for particular separation purposes. Zeolite A, like other zeolites, is synthesized in a gelling process. Sources of alumina (usually sodium aluminate) and silica (usually sodium silicate) are mixed in basic water solution to give a gel. The alkali agent can be NaOH or solutions of quaternary ammonium salts, amines, or other polar organics. The gel is then heated to $70 - 300^{\circ}\text{C}$ to crystallize the zeolite. The zeolite is normally synthesized in the Na^+ form. This can account for Na presence in the 5A zeolite LINDE Type A, and the non-complete ion exchange of Na^+ by Ca^{++} can justify a 5% of NaO in CL

3. MATERIALS AND THEIR INTERACTION WITH RPC GAS MIXTURE

molecular sieve. Chemical composition of standard LINDE Type A zeolite is:



ZEOCHEM(16) Molecular Sieve type 5A is an alkali alumino Silicate, and it is the calcium form of the Type A crystal structure. Typical chemical formula is:



Type 5A has an effective pore opening of 5Å. It is especially suitable for Pressure Swing Adsorption (PSA) applications where it may be used for the separation of normal- and iso-paraffins (C₄ to C₆ species), in PSA hydrogen purification and in oxygen concentrators. It is an excellent adsorbent to remove water, CO₂, H₂S from sour natural gas streams, while minimizing COS formation. Light mercaptans (CH₃SH) are also adsorbed. It is also used for production of high purity N₂, O₂, H₂ and inert gases from mixed gas streams. ZEOCHEM molecular sieve Type 5A can be regenerated by either heating in the case of thermal swing processes; or by lowering the pressure in the case of PSA processes. To remove moisture from a 5A molecular sieve, a temperature of 250 – 300°C is required. A properly regenerated molecular sieve can give moisture dew points below –100°C, or mercaptan or CO₂ levels below 2 ppm.

3.2.2.3 Metallic filters

The BASF(17) Catalyst R3 12 finds application in the petrochemical industry thanks to two main key factors: very good mechanical properties and extremely fine crystal dimensions, which provides a very large active area. This purifier is designed for removal of Arsine, Phosphine, H₂S and COS in the treatment of processes and product streams. Moreover is widely used in the purification of polymer grade propylene, and in guard beds to protect noble metal catalysts from Arsenic and Sulphur. They react with the Cu and Zn constituents in the catalyst to form stable metal complexes which do not migrate or desorb off of the catalyst, therefore making R3-12 not totally regenerable. The composition is nominally 40 wt.% CuO, 40 wt.% ZnO, and 20 wt.% Al₂O₃. Zinc is not reduced by the Hydrogen before than 550°C (differently from the Copper), the presence of ZnO is justified by the fact that it can remove efficiently Arsenic, Phosphates and Sulfurs.

3.2 The scaled-down closed loop experimental setup

BASF(17) Catalyst R3-11G is designed for regenerative removal of O, CO, H and others from industrial gases and liquids.

LEUNA(18) Catalyst Ni – AlO₃ filter type 6525 (not produced anymore) is used for hydrogenation of benzene, phenols and cresols, reduction amination of alcohols, aldehydes and ketones into the corresponding amines, methanations. This filter was introduced with the scope to remove O₂ from gas mixture containing mostly nitrogen, argon, neon or CO₂. The catalyst consists of approximately 60 wt.% Ni in alumina tablet form. It is declared vulnerable to humidity, and the presence of very fine dusty particulates which calls for a particulate filter. The nickel's reduction is not reversible up to 1000°C, several studies have been performed about this reaction since it has a relevance in the extraction of the Nickel itself.

Since all these metals used as purifier materials are oxidized during their operations, before the usage in the Closed Loop system, they must be activated performing an initial regeneration to purify them from ambient air absorbed.

3.2.2.4 Material and detector quality control

The RPC chamber production is a process that involves several steps, different materials and technologies; the quality control scheduled at CERN site is utmost important because it validates the entire detector in terms of material and performance which must be compliant with strict CMS requirements. A big part of the RPC chambers are produced in Italy while the rest comes from: Pakistan, China and India; the assembly is typically done at CERN.

The first item which must be validated before any chamber construction is the bakelite performances; this normally happens close to the construction site since a part of the production is not taken in consideration commonly due to wrong obtained resistivity value. As discussed in Sect. 2.2 the resistivity value is really important for the chamber performances. Then the second step concerns the chamber construction which implies the gas tightness of the detector, the stable anodic current measurement and a controlled resistivity along time. The latest quality control is at the level of efficiency, cluster size, noise and other several crucial aspect of the detector which describe its behaviour. At CERN, precisely in the Forward muon Lab at the ISR experimental area and at 904 building the quality control tests have been performed. Within this task the work has been organized following an uniform schedule with the goal to standardize

3. MATERIALS AND THEIR INTERACTION WITH RPC GAS MIXTURE

the evaluation of chamber performances. The main measurements are efficiency and cluster size evaluation along with noise studies and dark current long term stability.

At the Forward ISR Lab was in operation a general purpose cosmic stand with the possibility of testing several chambers at same time. We have used this already existing system to test and qualify spare chamber for the CMS experiment providing summary datasheets with detailed plots in order to fully characterize the detector. In 2010 the CMS collaboration decided to complete the muon system installed in the cavern with the latest layer, the so called *RE4* project. Then in 2011, after the some trial dummy bakelite production and test, it was needed a cosmic stand to validate this new production. The activity of building a new powerful cosmic telescope was running in parallel with others with the objective to build a cosmic stand with new standard NIM-VME electronics modules and a new Detector Control System, in such a way to guarantee fast and reliable detector quality control.

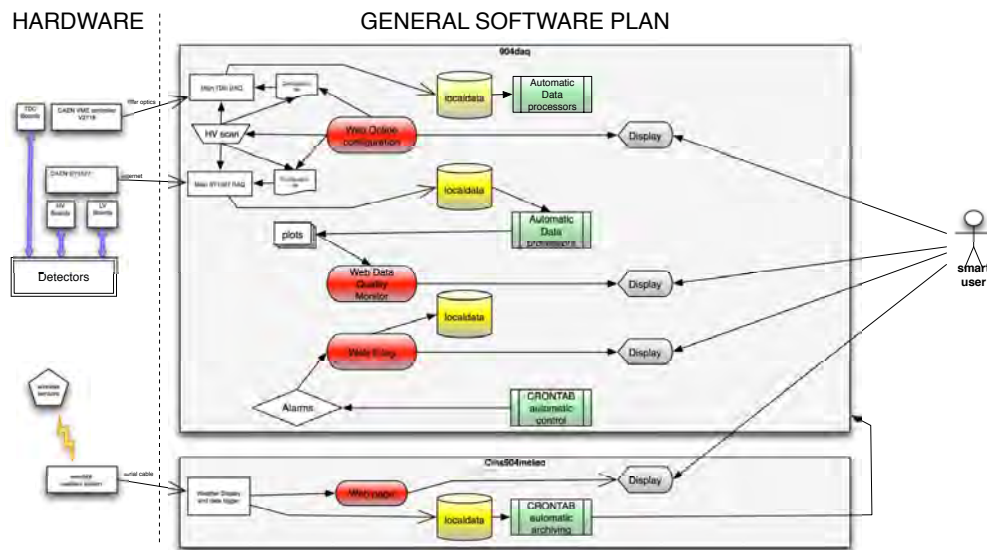


Figure 3.4: Software development for the new RPC cosmic stand.

In Fig.3.4 a schema of the developed software is shown, hardware electronics is still under installation and it will be ready and operational by the March 2012. The developed framework foresees an online recording of environmental and detector variables such as current, applied HV and settings of the power supply. All these information

3.2 The scaled-down closed loop experimental setup

are saved automatically in files according to a configuration file which is written by a very user friendly web-application. Moreover the main TDC DAQ is also set via web and data are automatically organized and ready to be stored into a database.

3.2.3 Preliminary analysis

3.2.3.1 Setting up the chemical setup

To determine the efficiency absorption of F^- , by means of using LiOH solutions, an experimental setup has been adopted using 5 flasks in series, as summarized in the Tab. 3.1. The first bottle was filled with ultra-pure water and high HF concentration (50g/l), while the remaining bottles with LiOH solution (pH=11). An argon gas flow of 10ml/min has been set in order to flush the bottles containing lithium idroxide with gas containing HF.

Table 3.1: Chemical setup summary flasks

Flask 1	190ml water plus HF (50000mg/l)
Flask 2	200ml LiOH (pH=11)
Flask 3	200ml LiOH (pH=11)
Flask 4	200ml LiOH (pH=11)
Flask 5	200ml LiOH (pH=11)

After the system was sealed and the mass flow measured in input and output we run the system for 91 hours (51.8l); at the end all flasks were open for analysis. From every flask 2ml were prelevated for the ionic cromatography analysis and we obtained results shown in Tab. 3.2

The F^- ions appeared only in the Flask 2, this means that the absorption efficiency of this system is close to 100%, at least up to 13.35 ± 0.07 mg/l of F^- in a bottle with a pH up to 7.72 ± 0.2 (measured at the very end of the experiment). A very high concentration of Cl^- was found in all flasks, this is explainable considering that bottles are made of PVC. For precaution in the ISR data-taking all flasks were washed several times with ultra-pure water before any usage.

3. MATERIALS AND THEIR INTERACTION WITH RPC GAS MIXTURE

Table 3.2: Preliminary results from efficiency analysis of the chemical setup

Sample (mg/l)	F ⁻ (mg/l)	Cl ⁻ (mg/l)	F ⁻ (mg)	Cl ⁻ (mg)
Supply	50628±480	< 500	9650±92	< 100
Flask 1	49075±1022	< 500	9226±192	< 100
Flask 2	13.35±0.04	1.76±0.08	2.52±0, 01	9.30±0.02
Flask 3	< 0.02	1.55±0.07	< 0.004	7.69±0.01
Flask 4	< 0.03	1.50±0.00	< 0.004	7.83±0.00
Flask 5	< 0.04	2.49±0.04	< 0.004	13.07±0.01

3.2.3.2 Filter studies

The zeolite filter, together with metallic filters, is supposed to be initialized at the beginning of its usage. For what concerns the metal filters, the initialization process (called regeneration), works reducing the metals oxidized during their usage. The process is described in Sect. 3.2.4.3. Before starting the data-taking sample of zeolite have been analyzed in order to understand, at first approximation, how the regeneration process could change the purifier composition, especially about the possible collected pollutants. In Fig. 3.5, 3.6, 3.7, 3.8, 3.9, 3.10 and 3.11 summary histograms of pollutants's filters are shown. In particular it seems that the regeneration process does not purify totally the filters; moreover the fluorine concentration is really accumulated dangerously during the filter usage and only partially removed by the filter initialization. In the Sect. 3.2.4.2 a lot of emphasis has been put on the fluorine trend since F⁻ is very electronegative and of course reactive.

Bakelite could suffer about the presence of such ions and Sect. 3.2.5.2 depicts several experimental results where the bakelite inner surface shows several defects related to aggressive and very chemically active ions.

3.2 The scaled-down closed loop experimental setup

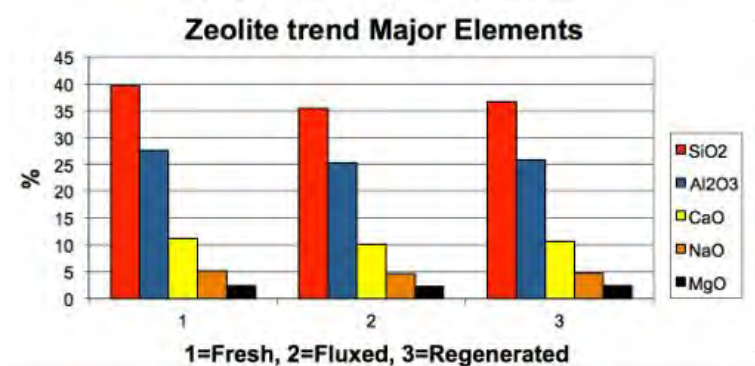


Figure 3.5: Element trends in the zeolite purifier.

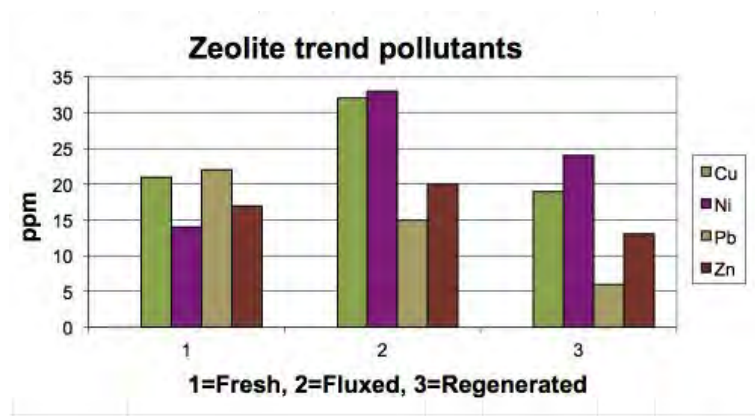


Figure 3.6: Pollutants found in the zeolite purifier.

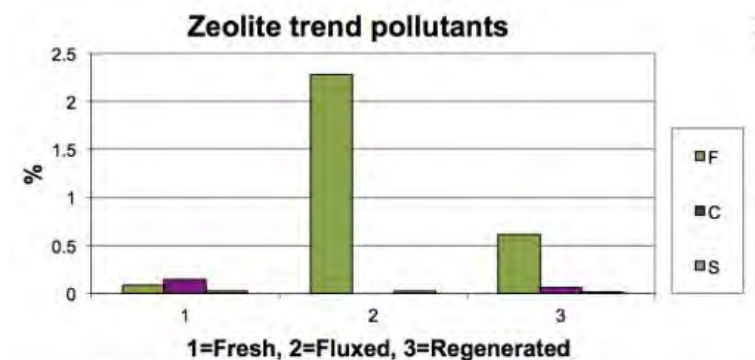


Figure 3.7: Pollutants found in the zeolite purifier.

3. MATERIALS AND THEIR INTERACTION WITH RPC GAS MIXTURE

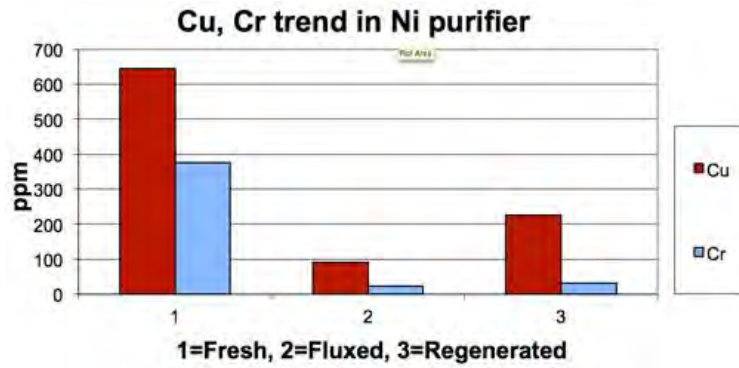


Figure 3.8: Pollutants in the Ni metallic filter.

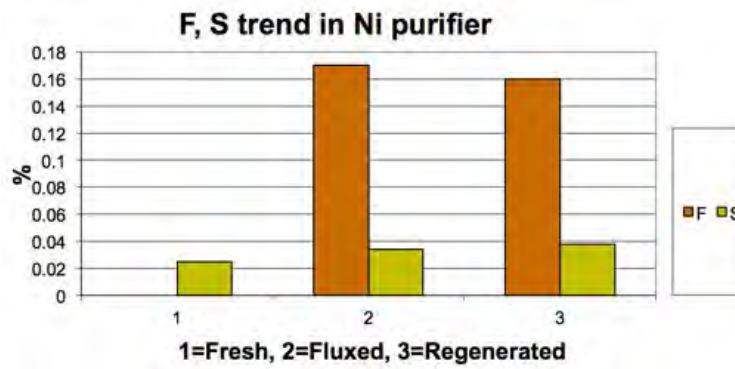


Figure 3.9: Pollutants in the Ni metallic filter.

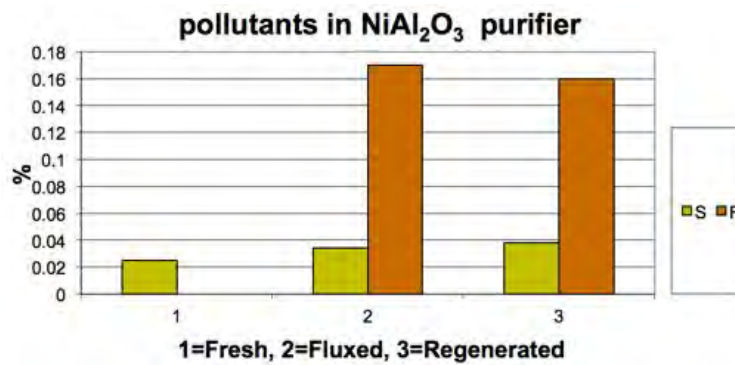


Figure 3.10: Pollutants in the Ni₂Al₃ metallic filter.

3.2 The scaled-down closed loop experimental setup

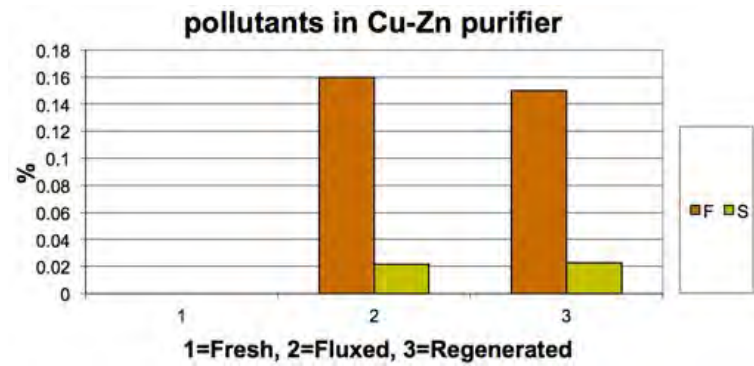


Figure 3.11: Pollutants in the CuZn metallic filter.

3.2.4 Experimental Setup

3.2.4.1 Hardware Setup

The experimental setup (Fig. 3.12) is composed of a CL system and an open mode gas system(19) as indicated by the schema at Fig. 3.13. The CL is composed of mixer, purifiers (Fig.3.14), recirculation pump and distribution gas lines that supply the RPC detectors. Eleven double-gap RPC detectors are installed, nine in recirculation regime and two in open mode.



Figure 3.12: A photo of the ISR Closed Loop test.

3. MATERIALS AND THEIR INTERACTION WITH RPC GAS MIXTURE

Each RPC detector has two gaps (up-stream and down-stream) whose gas lines are serially connected. RPC detectors ($200 \times 100\text{cm}^2$) are operated at 9.2kV by means of the CAEN(20) SY1527 power supply. Currents and applied HV are recorded online along with environmental conditions, logged by an Oregon Scientific WMR968 meteo station. Gas sampling points, before and after each filter, in the Closed Loop allow to keep under control the gas composition with gaschromatography and *ad-hoc* chemical analysis discussed in details in Sect. 3.2.5.

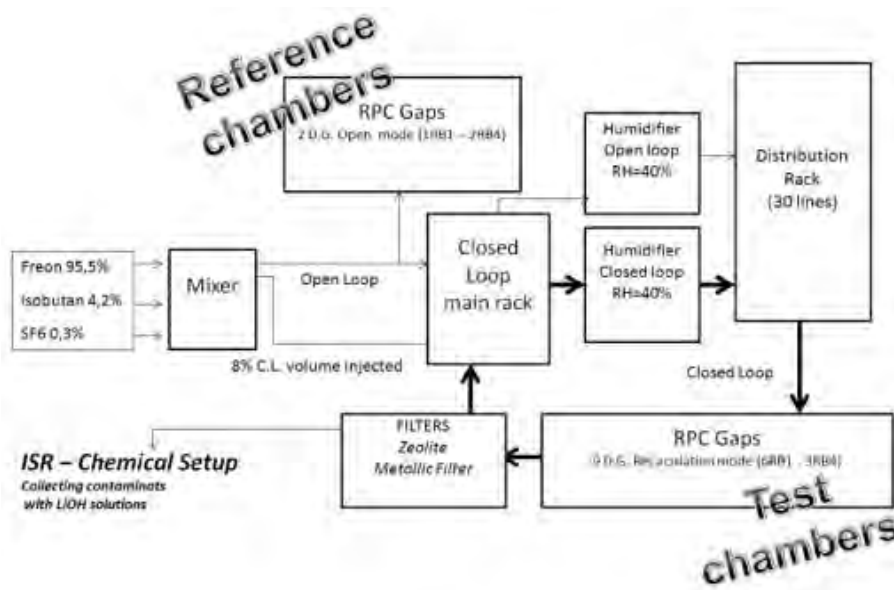


Figure 3.13: The setup of the ISR Closed Loop test.

In the CL system gas purity is guaranteed by a multistage purifier system (Fig. 3.14) (16), (17), (18), (21), (22):

- PURIFIER 1 consisting of a cartridge filled with 5\AA (10%) and 3\AA (90%) Type LINDE molecular sieve manufactured by ZEOCHEM;
- PURIFIER 2 consisting of a cartridge filled with 50% Cu-Zn filter type R12 manufactured by BASF and 50% Cu filtre type R3-11G manufactured by BASF;
- PURIFIER 3 consisting of a cartridge filled with Ni AlO_3 filtre type 6525 manufactured by LEUNA;

3.2 The scaled-down closed loop experimental setup

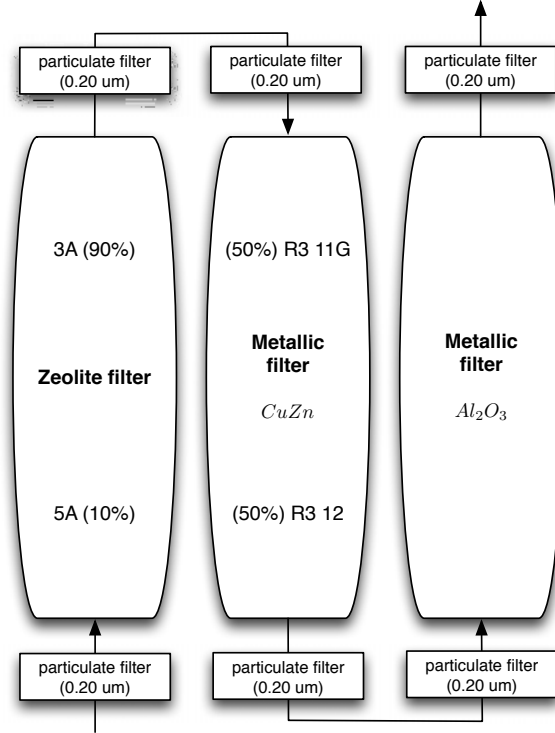


Figure 3.14: Schema of adopted filters at ISR Closed Loop gas system

About the metallic filters, actually installed in the Closed Loop CMS gas system, it was decided to adopt general purpose industrial purifiers to remove oxygen. The first metallic filter(17) contains NiAl_2O_3 while the second uses CuO and ZnO . Metallic particulate filters are made of 17% Cr, 69% Fe, 12% Ni and 2% Mo and are installed before and after each purifier cartridge. The oxygen is blocked due to metallic oxidation of the filter, then before the installation each purifier must be reduced by means of a hot (215°C) noble gas flux. This gas is a mixture (called Noxal) of Ar and H_2 (80:20).

Chemical analyses have been performed in order to study the dynamical behaviour of dark currents increase in the double-gap RPC chambers to correlate the presence of contaminants, measure lifetime of unused purifiers, and identify contaminants in correlation with the increase of currents.

3. MATERIALS AND THEIR INTERACTION WITH RPC GAS MIXTURE

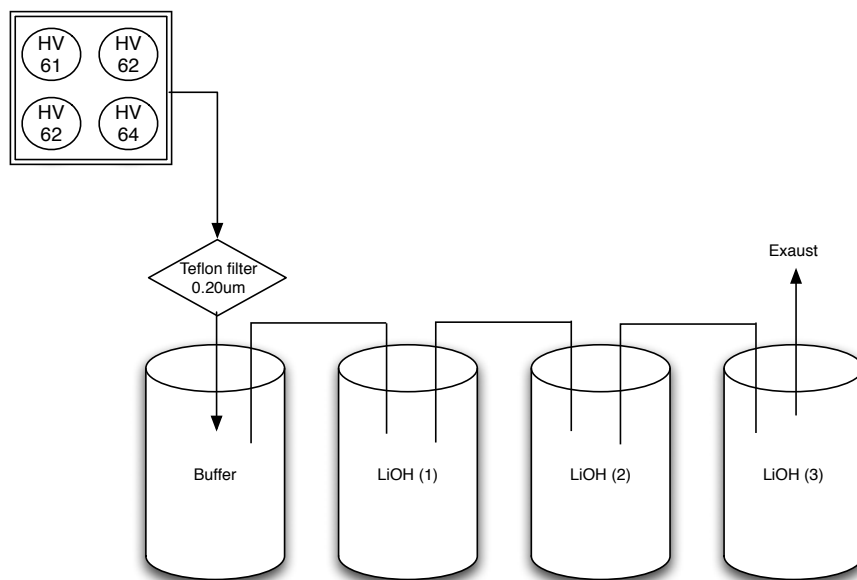


Figure 3.15: ISR Closed Loop: Chemical setup

In the chemical analysis setup, as shown in Fig. 3.15, the gas is sampled before and after each CL purifier, and bubbled into a set of PVC flasks. The first flask is empty and acts as a buffer, the second and third flasks contain 250ml solution of LiOH (0.001mol/l corresponding to 0.024g/l, optimized to keep the the solution at pH=11). Before the flasks the gas is filter by a PTFE¹ filter 0.20µm to remove particulate. PTFE membrane are among the most efficient filters used in industrial air/gas filtration applications. The bubbling of gas mixture into the two flasks allows to capture a wide range of elements that are most likely to be released by the system, such as Ca⁺, Na⁺, K⁺, Cu⁺⁺, Zn⁺⁺, Ni⁺⁺, F⁻. At the end of each sampling line the flow is measured in order to evaluate the total amount of gas for the whole period of sampling. The sampling points (Fig. 3.16) are located before filters (HV61), after Zeolite (HV62), after Cu – Zn filter (HV64) and finally after the Ni filter (HV66).

¹Polytetrafluoroethylene (PTFE) is a synthetic fluoropolymer of tetrafluoroethylene commercially sold with the name Teflon by DuPont. PTFE is a fluorocarbon solid, as it is a high-molecular-weight compound consisting wholly of carbon and fluorine. PTFE has one of the lowest coefficients of friction against any solid.

3.2 The scaled-down closed loop experimental setup

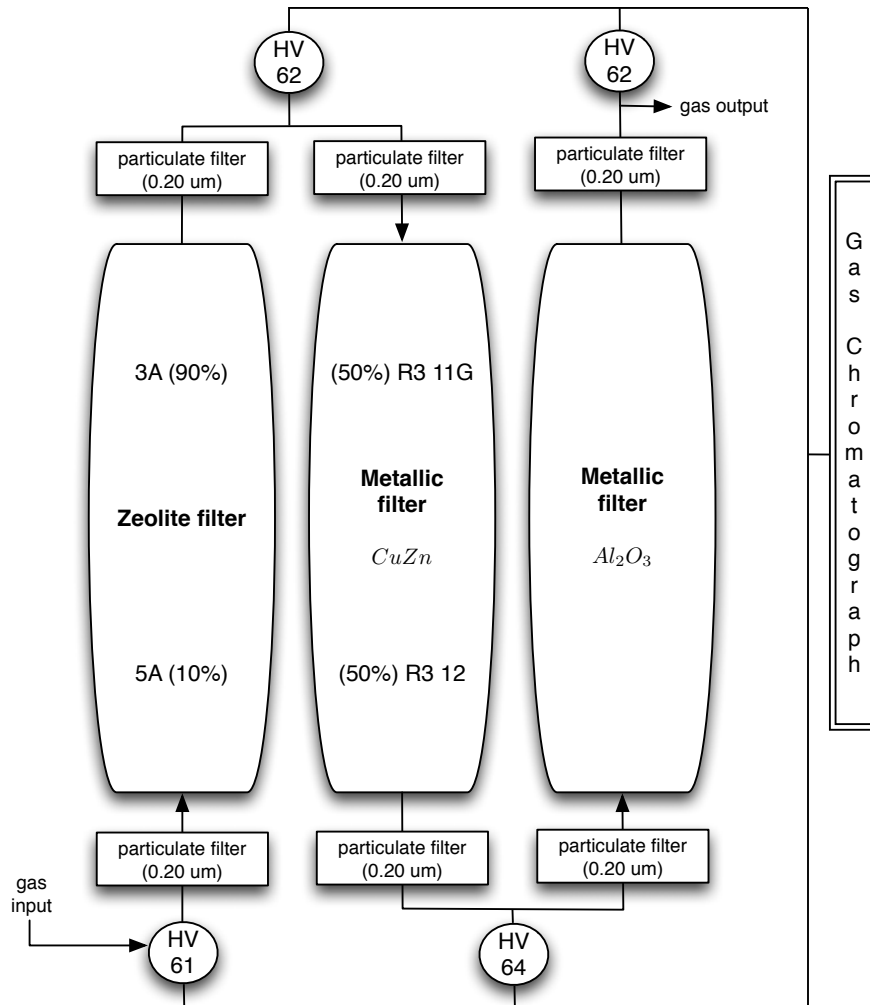


Figure 3.16: Chemical setup sampling points

RPC are very sensitive to environmental parameters (such as atmospheric pressure, humidity, temperature), this study has been performed in environmentally controlled hut with pressure, temperature and relative humidity online monitored (Figs. 3.17, 3.18).

3. MATERIALS AND THEIR INTERACTION WITH RPC GAS MIXTURE

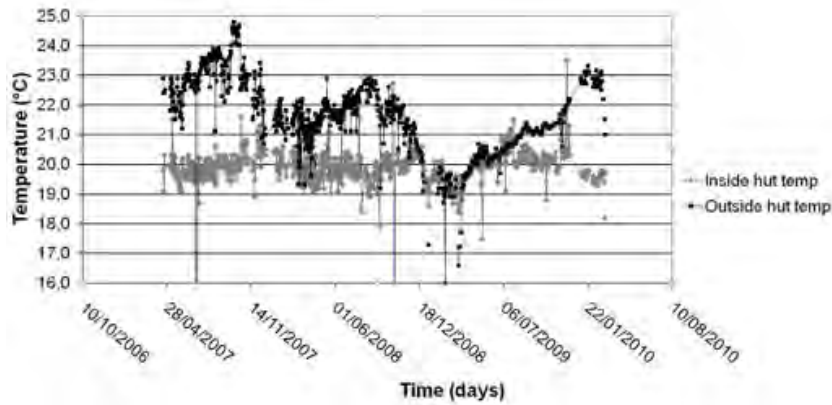


Figure 3.17: ISR Closed Loop: temperature distribution inside and outside the experimental hut.

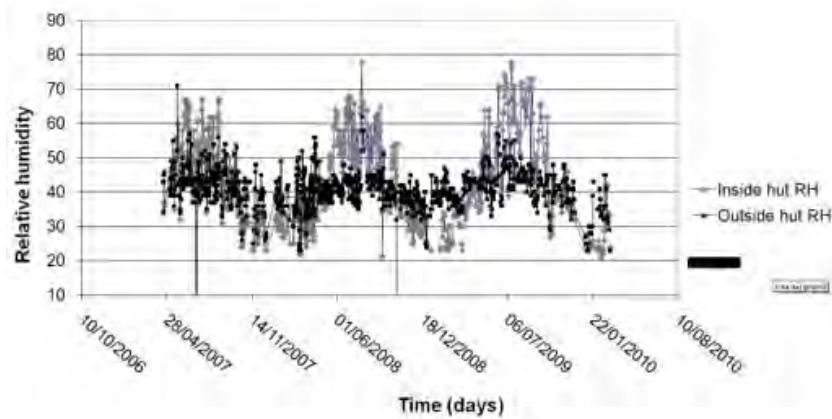


Figure 3.18: ISR Closed Loop: relative humidity inside and outside the experimental hut.

Gas mixture composition has been monitored twice a day by gas chromatograph, which also provided the amount of air contamination; over the entire data taking air was concentration was below 300 (100) ppm in closed (open) loop. The low air contamination was under control thanks to a careful freon bottle purging before usage. At very first run purifiers were operated with unused filter material while in the second run those cartridges were regenerated in order to compare the lifetime of new and used filters.

3.2 The scaled-down closed loop experimental setup

3.2.4.2 F⁻ sensors as monitoring device

As explained in Sect. 3.2.4.1, in the Closed Loop gas system there were several installed sampling points such that the system was completely under control and carefully daily monitored. In the sampling point HV61 and HV62 (before and after the first zeolite filter) a device for monitoring F⁻ production was installed and in operation during the whole data-taking period. The scope of this monitoring was to really evaluate the capacity of the zeolite filter to trap fluorine ions measuring, at same time, the lifetime of the filter itself. For each sampling point a selective electrode¹ was installed to measure the ionic potential, which is directly connected to the ions concentration. The fluoride electrode is a potentiometric device and requires a separate reference electrode to complete its electrolytic circuit. The internal membrane is made of a lanthanum fluoride crystalline pellet which is practically insoluble in the test solutions being measured and produces a potential change due to changes in the samples ion activity. When the ionic strength of the sample is fixed, the signal voltage is proportional to the concentration of fluoride ions in solution and the electrode follows the Nernst equation:

$$E = E_a + \frac{RT}{nF} \cdot \log(C_{\text{ion}})$$

E = Measured voltage

E_a = Reference and fixed internal voltages

R = Gas constant (8.314 J/Kmol)

n = Charge on ion (1-)

C_{ion} = Concentration of analyte

T = Absolute temperature

F = Faraday constant(9.648 × 10⁴C/equivalent)

(3.4)

The selective electrode was monitoring the actual collected amount of ions integrating it over time, thanks to a custom *ad – hoc* software the electrochemical potential was logged every 10 minutes in order to estimate the F⁻ production rate and concentration in the system along with the RPC performance. Both electrodes (reference and

¹We have used the Hanna-Instrument 4010, a solid state half-cell sensor that requires a separate reference like the Hanna-Instruments 5315 a silver-silver chloride double junction half-cell reference electrode.

3. MATERIALS AND THEIR INTERACTION WITH RPC GAS MIXTURE

sensor) were immersed in a diluted TISAB II solution. This increases and stabilizes the ionic strength of the solution making a linear correlation between the logarithm of the concentration of analyte and the measured voltage according to the Eq. 3.4. The calibration of the two selective electrodes was, of course, utmost important; It was performed at the beginning of the run and also during the run itself to double-check a possible shift of the factory settings. For the calibration we have used known solutions containing: 0.001mg/l, 0.005mg/l, 0.01mg/l, 0.10 mg/l, 1.0 mg/l, 10.0 mg/l, 20.0 mg/l, 50.0 mg/l concentration of F^- ; Fig. 3.19 shows the calibration curves.

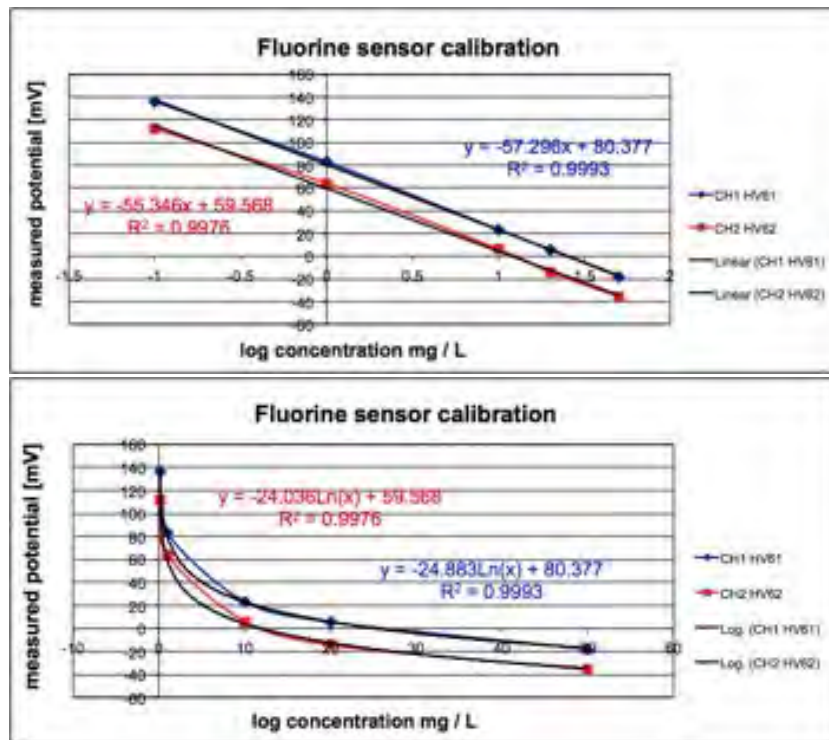


Figure 3.19: Calibration curves of fluorine monitoring sensors.

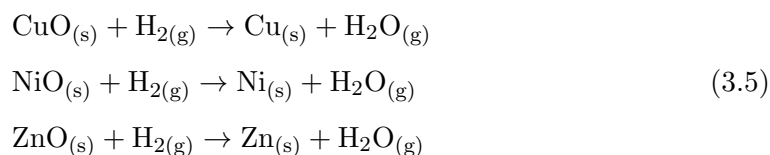
3.2.4.3 Start-up

The Closed Loop system, during the start-up phase, has to be filled with the standard gas mixture paying attention to the air concentration that with the system off is of course very high. Once the system is filled-in and in stable condition, the detectors may be ramped up to the nominal voltages (9.2kV) slowly in steps of 100V (to stabilize the anodic gap current). Several times per day the system is carefully controlled

3.2 The scaled-down closed loop experimental setup

with a checklist in which are noted date/time, gas mixture composition, percentage of fresh gas injected into the loop, temperature/humidity of ambient and gas lines in open and closed loop mode, mass flow values of all gas lines and other several values of the main racks and of the gas distribution panel. Very important is also the gaschromatograph which is used daily to check the gas composition, frequently gas bottles contain impurities which have to be identified and removed promptly.

Before their usage, purifiers must be initialized because filter materials are activated as soon they are in contact with air; a special process is performed just before the filter is installed in the setup. During this special process purifier materials are “regenerated” performing a reduction of the metals and a thermal treatment of zeolites to let trapped water evaporates. For the zeolite the regeneration process consists in heating up to 200°C using an argon flux while for the metal filters also Hydrogen is used in a mixture called “Noxal”. This mixture is flushed for 2 hours increasing gradually the temperature up to 150°C, then the temperature is increased up to 215°C and finally the filters are cooled down to the ambient temperature flushing argon. The chemical reactions are favoured by the temperature and they are summarized here:



3.2.4.4 The ISR checklists

The Closed Loop gas system was installed and in operation at the ISR experimental area. The gas system was composed of 3 main racks and many other equipments in order to control system variables and trigger alarms in case of emergency. Since the gas mixture is declared flammable utmost attention must be paid to any operation. The presence of isobutane required a careful monitoring system and the human presence in order to ensure stable and safe operation. The system then was under human control all the time, while twice a day a dedicated checklist (shown in the in the Appendix C) was supposed to be executed. The purpose of the checklist was to really follow the system in all its parts, since to carry out our long data-taking a very stable operation was mandatory. The data-taking was, in fact, a success also thanks to this very careful control of the hardware. In the Tab. C.1, C.2, C.3 one can identify several blocks; the

3. MATERIALS AND THEIR INTERACTION WITH RPC GAS MIXTURE

main one concerns the variables which define the operating mode of the recirculation system. The gas system in fact can run with different amount of fresh gas injected in the loop and also pressure in different sampling point must be under certain limits not to damage any detector. On the other hand also for stable data-taking all gas fluxes had to be equalized between different lines, this was performed via pressure reducers and rotameters manually adjusted. Another very important task was to keep under control the gas composition by means of gascromatograph mainly to check that the gas composition was actually the same one set on the main supply line and no contaminants were present, in both open and Closed Loop. In the end to complete the picture of the data-taking all variables from the detector performance and from the chemical setup such as pH of LiOH solutions and gas flow through each flask were manually recorded.

3.2.4.5 Software setup and further developments

The DAQ software was already set-up since 2006 and remained untouched. On the contrary the hardware system has seen a lots of changes but any of these modifications had an impact on the data structure which was decided during the developing of the DAQ.

The main module was written in C++; it takes care of monitoring the high voltage, current and status of RPC channels writing them into ASCII files. Each file contains RPC variables and data coming from the weather station installed in the experimental setup. Temperature and humidity of both main gas manifold (open and closed loop) are recorded in two separate files. The gas (open and closed) is also sampled daily with a GC and the spectrum is saved as well in a dedicated file. Finally the F^- concentration is monitored and recorded by a proprietary software which logs via USB values from the Hanna Instrument(23) device H2414; this device reads the electrochemical potential of a solution which is function of F^- concentration.

In Fig. 3.20 is shown the software development for the fine tuned analysis of the data. The “Analysis processor” module reads the files produced by the DAQ according to the user configuration file, which can be turned into an interactive menu. The configuration tells to the processor which runs or periods have to be analyzed. The display routine plots all the correlations and trends according to a predefined schema.

3.2 The scaled-down closed loop experimental setup

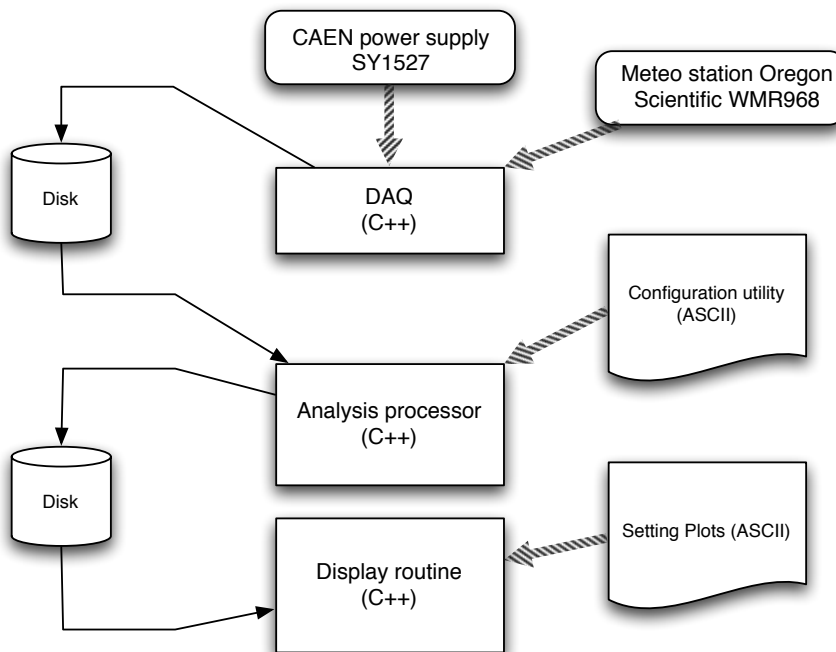


Figure 3.20: Software development at ISR.

A big work has been done concerning the “Analysis Processor” since inside this module all data are going to be processed. The amount of data reached 10Gbyte in the second half of 2011 and C++ with ROOT libraries were chosen as best tool to perform an analysis of such amount of data. Thanks to built-in data mining algorithm inside ROOT framework and the flexibility of C++ the analysis of whole data-set takes less than one hour. The big latency inside the code is the fitting part which is performed on the daily HV scan data. Each channel is ramped up from effective 0-10.2kV and then the software takes care of data-fitting day by day, channel by channel. The chosen fitting function is:

$$y = ax + b(e^{cx} - 1) \quad (3.6)$$

where y represent the detector anodic current, x the applied high voltage and a, b, c fitting variables. The function for non applied voltage returns a null value, this situation represent a switched OFF channel; the first part of the HV scan is dominated by the linear coefficient which represents physically the series resistance of circuit for bakelite

3. MATERIALS AND THEIR INTERACTION WITH RPC GAS MIXTURE

plus gas gap plus graphite plus cables. The second part is dominated by the exponential function which models the avalanche process as explained in Sect. 2.2. Then the total anodic current could be considered as sum of two terms: the linear and exponential part. The first linear term is correlated to the resistivity of the bakelite and the relative current is called “ohmic component”. The second term is almost zero up to 6kV and starts increasing exponentially meaning the chamber is running in Avalanche region and amplification occurs, this second current component is called then “signal current”.

3.2.5 Results

3.2.5.1 RPC performance

The scaled-down CMS Closed Loop gas system was in operation following an intense data taking from 2008 to 2011. As discussed previously, in Sect. 3.2.4, eleven RPCs double gap were installed and monitored. The Tab. 3.3 shows the detailed view of working and dead channels. The RPC current, as detailed before, depends essentially from the gas mixture and environmental conditions such as temperature, pressure and relative humidity. The gas mixture affects the gain and the working point of the detector itself while a possible gas contamination is danger since it may shift the working point up to the level of damaging irreparably the detector. Fluorine is very suspicious pollutant since it is produced and collected in the closed loop system, it is highly reactive. At the ISR since September 2008 a big campaign of measurement started with the goal to characterize the closed loop system. In April 2009 it was noticed an increase in the anodic current of all detectors up-stream in the loop. The very first interesting result was to run with unused filters for 211 days with a total flow of 63l/h and $\approx 11\%$ fresh mixture injected in the loop. For what concerns the fluorine production, during this first run, the system collected $1.1008\mu\text{mol/l}$ so in total in the closed loop accumulated $45452.8\mu\text{mol/l}$. The production rate was almost constant till the system was switched OFF to put down the gap’s currents. In June 2010 it started the second run with used-regenerated filters, the average flux was $\approx 54\text{l/h}$ with an amount of fresh gas injected of 9.8% .

The data-taking was divided into two runs during 3 years. In the first run we have adopted unused material to fill the purifier cartridges while in the second run it was decided to run with old filters regenerated already used in the first run. Before to start

3.2 The scaled-down closed loop experimental setup

Table 3.3: Summary table of Closed Loop (CL) and Open Loop (OL) channels.

HV channel	Gas line	Modality		Status
1	A6	CL	Up-stream	OK
2	A6	CL	Down-stream	OK
3	A6	CL	Up-stream	BROKEN
4	A6	CL	Down-stream	BROKEN
5	A7	CL	Up-stream	OK
6	A7	CL	Down-stream	NOT INSTALLED
7	A7	CL	Up-stream	OK
8	A7	CL	Down-stream	OK
9	A1	OL	Up-stream	OK
10	A1	OL	Down-stream	OK
11	A8	CL	Up-stream	OK
12	A8	CL	Down-stream	OK
13	A8	CL	Up-stream	OK
14	A8	CL	Down-stream	OK
15	A9	CL	Down-stream	OK
16	A9	CL	Up-stream	OK
17	A9	CL	Down-stream	OK
18	A9	CL	Up-stream	OK
19	A10	OL	Up-stream	OK
20	A10	OL	Down-stream	BROKEN
21	A10	OL	Up-stream	OK
22	A10	OL	Down-stream	OK

3. MATERIALS AND THEIR INTERACTION WITH RPC GAS MIXTURE

Table 3.4: Summary table of Closed Loop (CL) and Open Loop (OL) channels.

Run	Cycle	Period	Comment		
1	1	29/08/2008 - 11/10/2008	stable currents	CL	unused filters
1	2	12/10/2008 - 22/01/2009	stable currents	CL	unused filters
1	3	23/01/2009 - 28/04/2009	increasing currents	CL	unused filters
1	4	29/04/2009 - 14/07/2009	increasing currents	CL	unused filters
1	5	15/07/2009 - 27/07/2010	decreasing current	OL	used filters
2	1	28/07/2010 - 07/01/2011	stable currents	CL	used filters
2	2	08/01/2011 - 05/07/2011	increasing currents	CL	used filters

the second run all filters were regenerated performing the same process used in the filter activation at the beginning of the first run. The activation process (described in Sect. 3.2.4.3) consists in flushing with hot (215°C) noble gas like Ar and H₂ (80:20) for half a day. Since the chemical analyses were performed collecting contaminants incrementally, (as detailed in Sect. 3.2.4) to mark different data-taking conditions we used different periods inside each run, as summarized by the tab. 3.4.

Considering the first run: cycle 1 and 2 started with initial stable currents up to the onset of the raise of currents which happened in cycle 3 while cycle 4 has seen a clear and full increase of currents; we terminated in order not to damage permanently the RPC detectors. After high currents cycle the system has been switched in open mode (cycle 5), the dark currents decreased to the initial low value. At that point after a stability period we started the second run. During this run also we had different cycles because in the beginning the currents were low and after some time they started increasing as the first run. The currents of all RPC detectors in open loop were found stable in all cycles. In Fig. 3.21 is shown the typical behaviour of one RPC detector in CL correlated with the concentration of main contaminants, discussed in more detail later in this section.

3.2 The scaled-down closed loop experimental setup

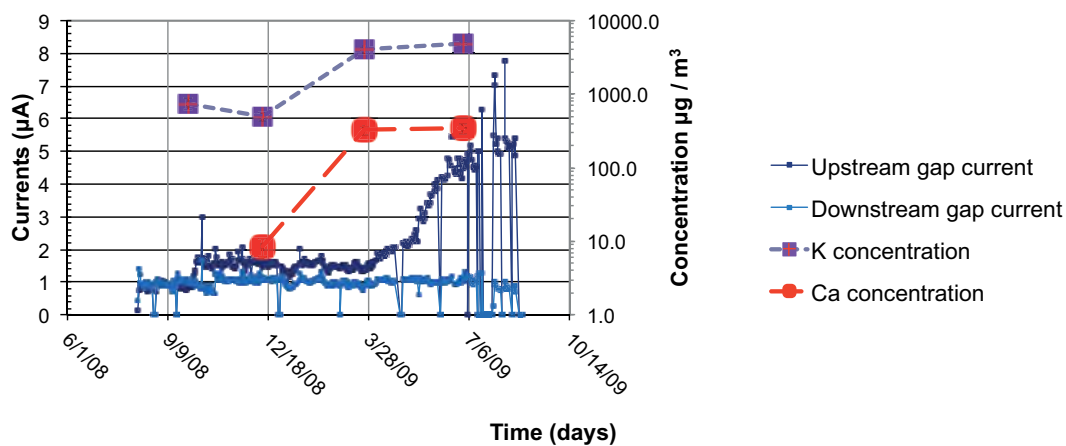


Figure 3.21: Dark currents increase in the up-stream gap and not in the down-stream gap, correlated to the detection of contaminants in gas.

While the current of the down-stream gap is stable throughout the runs, the current of the up-stream gap started increasing after about seven months. Such behaviour is suggestive of the formation of contaminants in the CL which are retained in the up-stream gap, thus causing its current to increase, and leaving the down-stream gap undisturbed.

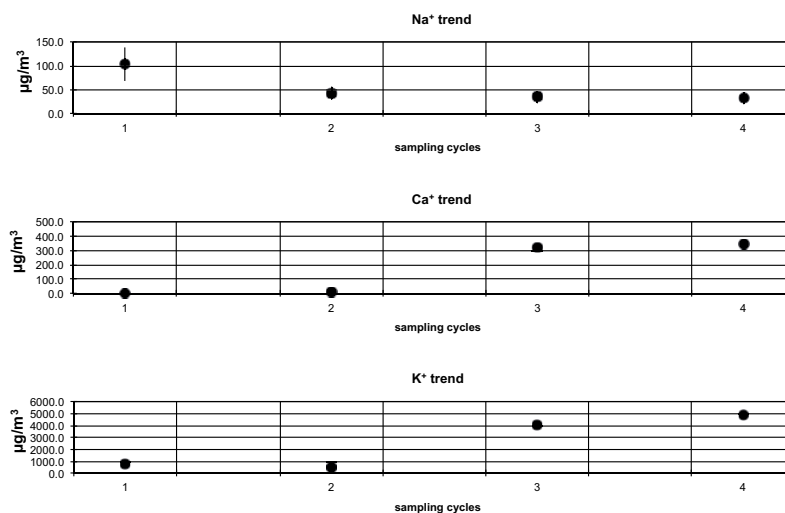


Figure 3.22: Concentration of Na^+ , Ca^{++} and K^+ in cycle 1-2-3-4 of the first run.

3. MATERIALS AND THEIR INTERACTION WITH RPC GAS MIXTURE

While the production of F^- is almost constant during the runs, significant excess of K and Ca is found in the gas mixture in cycles 3 and 4 (Fig. 3.22) The production of F^- is efficiently depressed by the Zeolite purifier as in Fig. 3.23. During the second run the F^- production was sensibly smaller compared to the F^- production occurred during the first run. The observed excess of K and Ca could be induced by the HF which is continuously produced by the system due to the presence of the F^- radical.

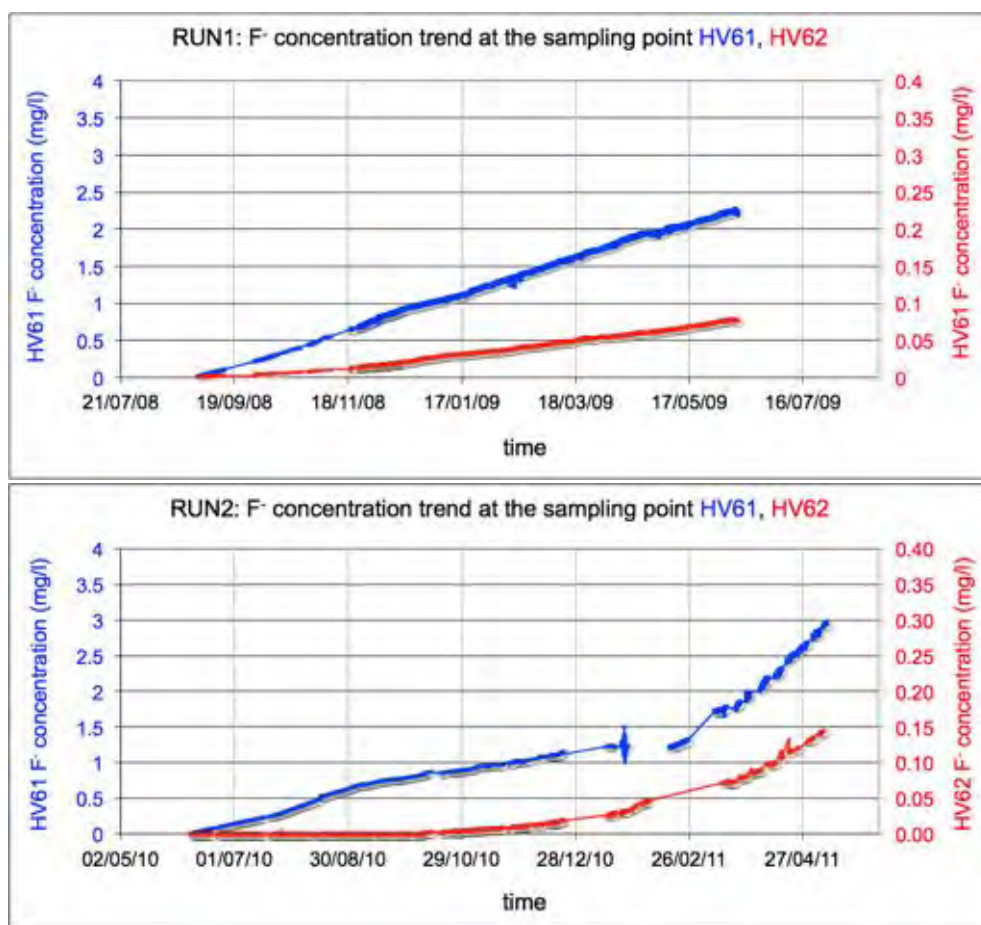


Figure 3.23: F^- production during first run (unused filters) and second run (used filters)

These results show that the lifetime of purifiers using unused material is approximately seven months. Contaminants (K, Ca) are released in the gas in correlation with the dark currents increase. The currents increase is observed only in the up-stream gap. The study suggests that contaminants produced in the system stop in the up-stream

3.2 The scaled-down closed loop experimental setup

gap and affect its noise behaviour, leaving the down-stream gap undisturbed. The presence of an excess production of K and Ca in coincidence with the currents increase also suggests a damaging effect of HF produced in the system on the framework of Zeolites which is based on K and Ca. In Fig. 3.22 the cumulative concentration of Na^+ , Ca^{++} and K^+ are shown in the cycle 1-2-3-4 of the first run. The Fig. 3.22 confirms that concentration of Ca^+ and K^+ is increased in the cycle 3 and 4 in coincidence with high currents of RPCs up-stream gap. In the cycle 1 and 2 RPC currents are still stable and low as the concentrations of Ca^+ and K^+ . Also the teflon filters (installed before the empty buffer flask) were analyzed, results are shown in Fig. 3.24 and Fig. 3.25.

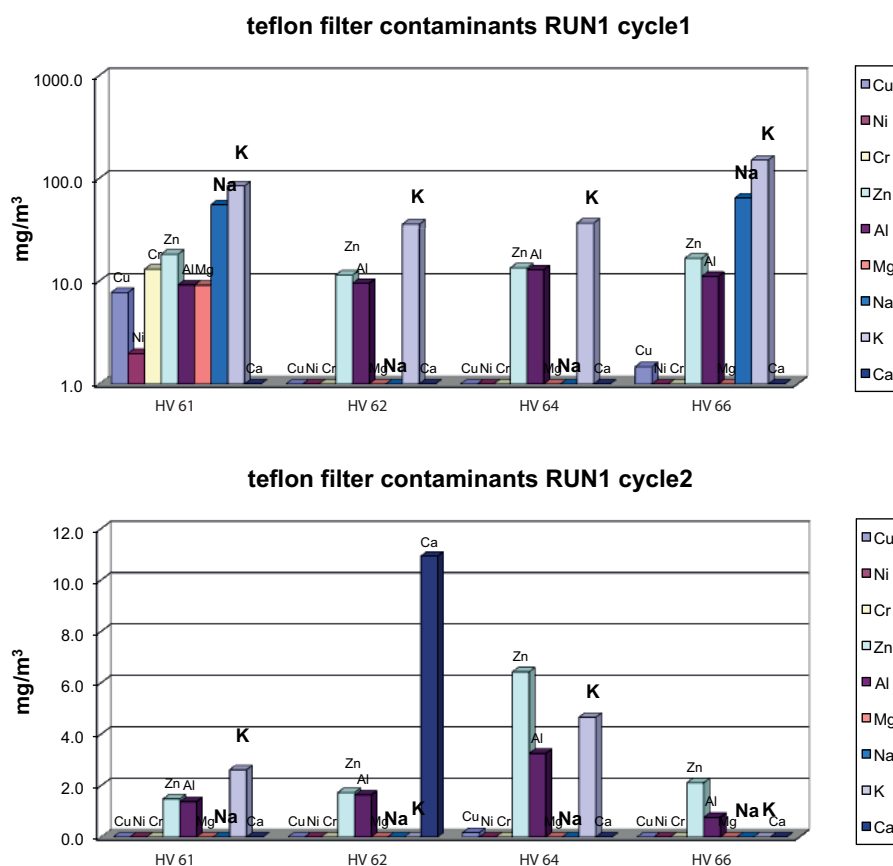


Figure 3.24: Concentration of various metallic compounds found in the teflon pre-filter installed in the HV61-62-64-66 during cycle 1-2.

3. MATERIALS AND THEIR INTERACTION WITH RPC GAS MIXTURE

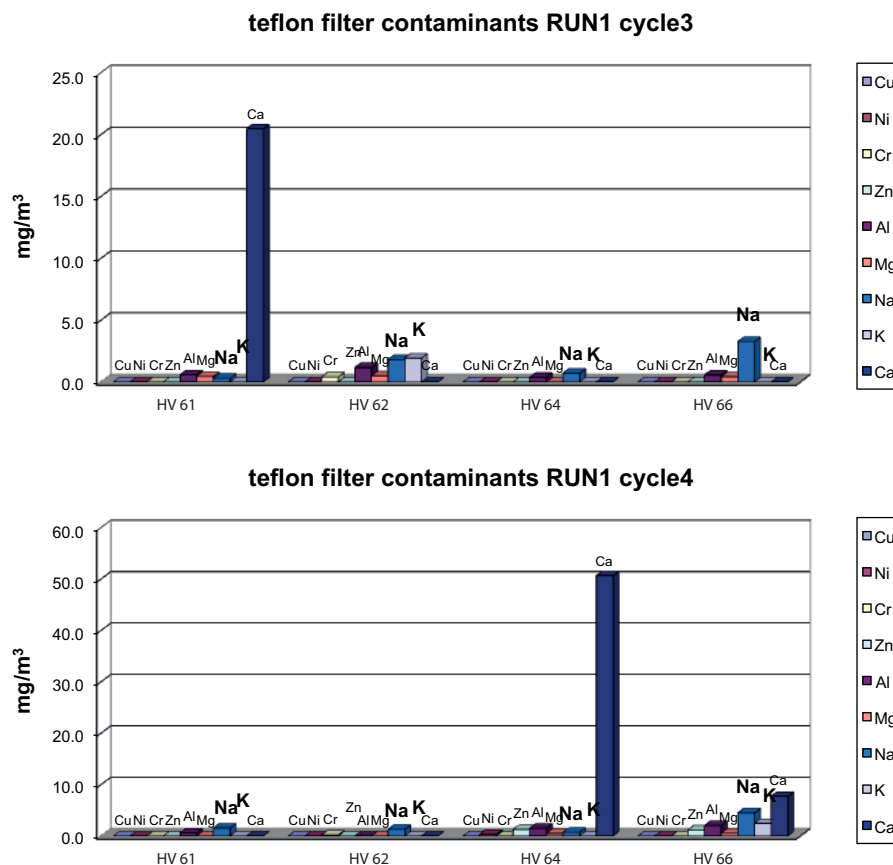


Figure 3.25: Concentration of various metallic compounds found in the teflon pre-filter installed in the HV61-62-64-66 during cycle 3-4.

In the Fig. 3.26 several solid particles found on the teflon filters, are shown. This indicates that even with the metallic particulate filter, dust compounds reach to pollute the gas system.

In Fig. D.1, D.2, and D.3 raw data (currents) from RPC double gap installed in the environmentally controlled hut at the scaled-down CMS closed loop gas system are shown. The data-taking was, as already mentioned, very long, and divided into two runs. In the first run clearly channel 1, 7, 11, 13, 16 and 18 increased the total current after several month of operation in recirculation mode regime. All these channels were up-stream gaps, while all the rest of working channels (down-stream gaps) operated with the same high voltage showed stable currents. In the second run, the test was

3.2 The scaled-down closed loop experimental setup

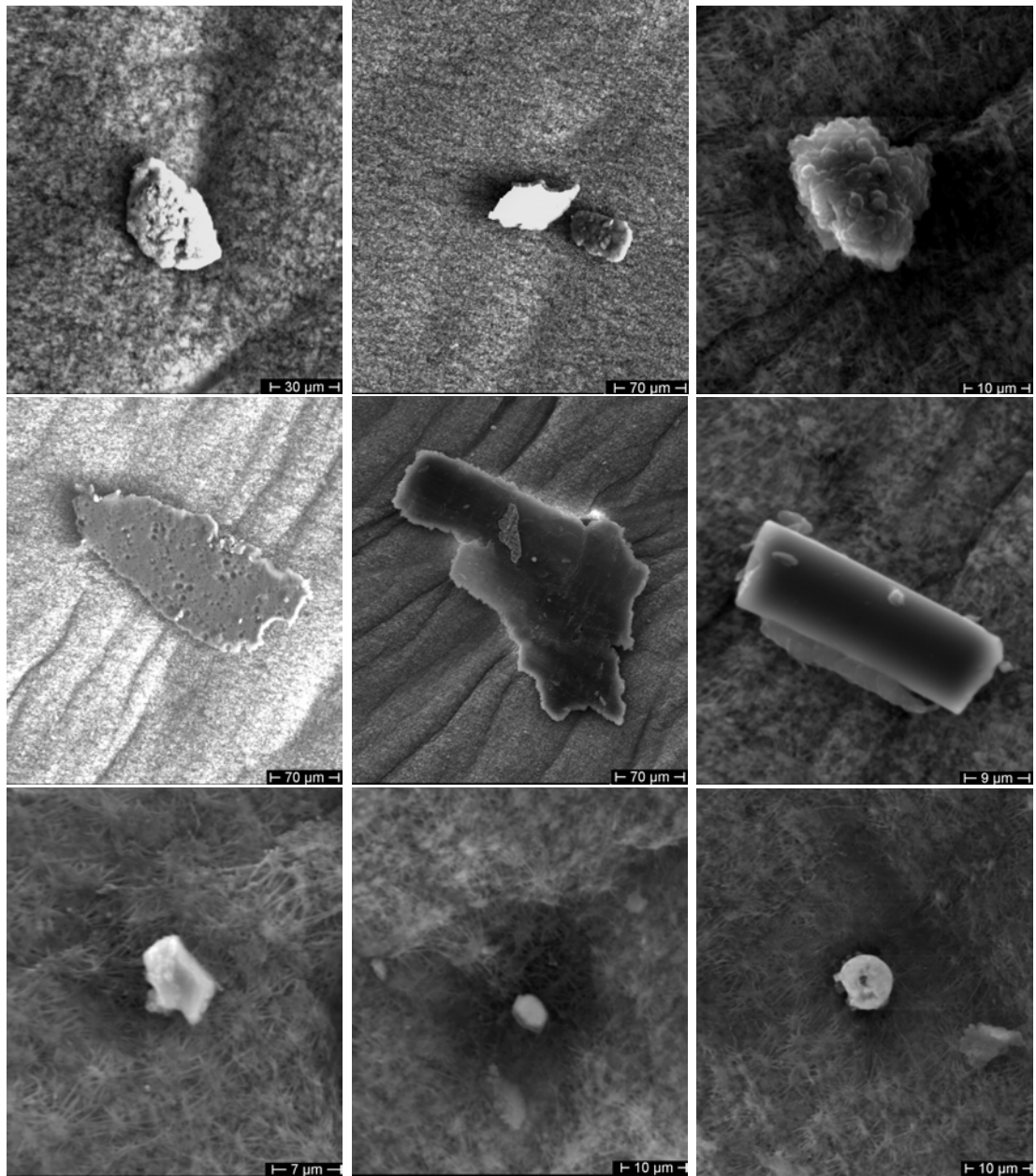


Figure 3.26: Teflon filters contaminants: Ca (first row left), Cu (first row center), Al (first row right), C (second row left) Cu (second row middle) Si, Ca and Al (second row right), Si (Third row left), Ti (third row center), S (third row right).

3. MATERIALS AND THEIR INTERACTION WITH RPC GAS MIXTURE

repeated in the same manner, but the first and second channels were swapped, in fact it is possible to see that in the second run the first channel shows a stable behaviour while the second channel shows increased current. The channel 2, in fact, in the second run, became an up-stream gap. In both first and second run 3 chambers were kept always in open mode (channels: 9-10-19-21-22), as mentioned in the Tab. 3.3, These chambers were used as reference. The rest of gaps were flown with recirculated gas with 10% of fresh gas injected in the closed loop. The gas flow was set at 1vol/h for all the channels. The system, since composed of several sub-systems, was several time very fragile, a very careful and daily monitoring allowed an overall smooth data-taking for more 3 years without any major problems.

A detailed chamber performance analysis has been carried out separating ohmic from the signal component using the developed tool described in Sect. 3.2.4.5. In Fig. D.4, D.5, D.6 and Fig. D.7, D.8, D.9 respectively ohmic and signal currents component are shown. The ohmic component represents the behaviour of the bakelite which is very sensible to gas mixture contaminants and environmental conditions. On the contrary the signal component describes the influence of contaminants and gas parameters on the detector's gain. This means that since the avalanche process is driven by gas properties, a different gain (and therefore signal current) is achieved for slightly different gas mixture. Even small compounds present in the mixture could shift the detector response as, in fact, it is clear in our data-taking. As described in Sect. 3.2.4.4, gascromatograph plots were daily produced but without finding any difference between the gas mixture sampled from the open and the gas recirculating in the closed loop; this is the reason why we performed detailed *ad hoc* chemical gas analyses online and offline. Both signal and ohmic current's component increase after several month of closed loop operation while for the open loop channels the behavior is quite stable even if there are fluctuations due to environmental variables and some spikes due to occurred problems to the gas system. The fact the ohmic and signal currents increased seems to indicate that both gas and bakelite properties are affected by the closed loop operation.

ISR Closed Loop test - Overall behavior

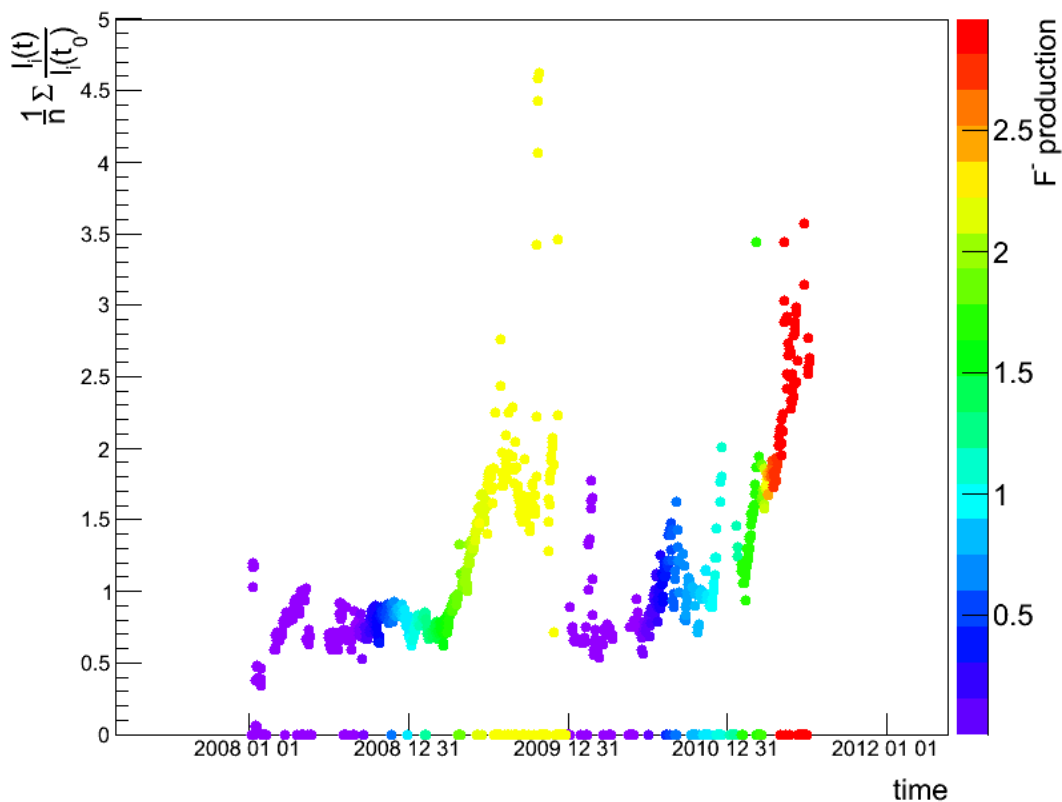


Figure 3.27: Total current during all runs with F^- production

Fig. 3.27 shows the integral of all currents averaged by their initial values; colors depict the F^- produced by the system. The first and second runs are clearly visible as well as the very high current and high F^- concentration reached during the second run. As shown, many contaminants have been found in the chemical setup; they could interact with the bakelite surface changing its properties, on the other hand these contaminants play also the role modifying the gas properties (and the electrical field inside the gap), the fluorine is suspected to play a big role since it is highly reactive. The Fig. 3.28 shows the comparison between F^- production sampled before and after the first (zeolite) filter which depress the F^- of a factor ≈ 50 in both case.

3. MATERIALS AND THEIR INTERACTION WITH RPC GAS MIXTURE

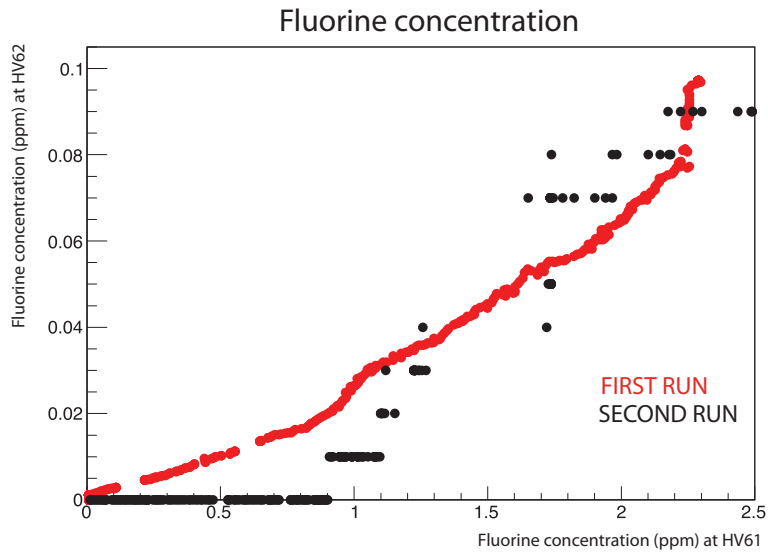


Figure 3.28: Filter performance in run1(red) and run2(black)

To better compare the filter behaviour, in the Fig. 3.29 the F^- productions, after the zeolite filter for both runs (1 and 2), along time are shown. In the second run (on the right) one can note that the slope is steeper and an higher value is reached also.

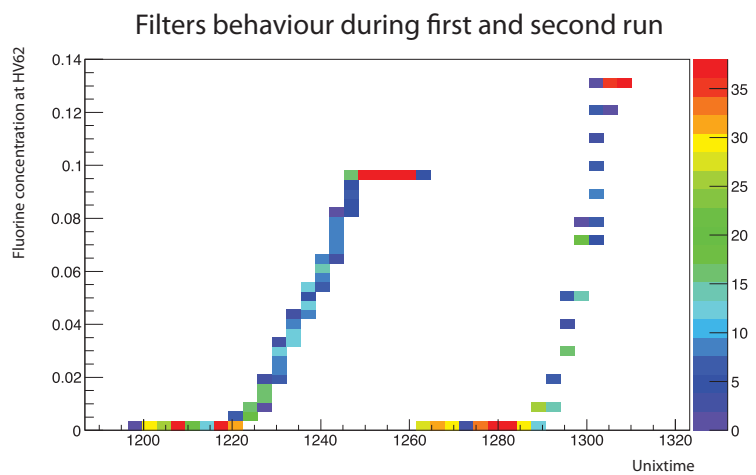


Figure 3.29: Filter behavior comparison

3.2.5.2 Surface defects

As discussed in Sect. 3.2.5, the detector behaviour is correlated with the status of the purifier materials installed in the closed loop gas system. On the other hand another important variable to keep in mind is the radiation level; at ISR we always operated with cosmic rays, in Appendix B radiation damage effects are discussed. By analysis of bakelites at LNF Frascati(24) it was shown that several surface defects play a very important rule in the interaction of inner bakelite surface with gas mixture.

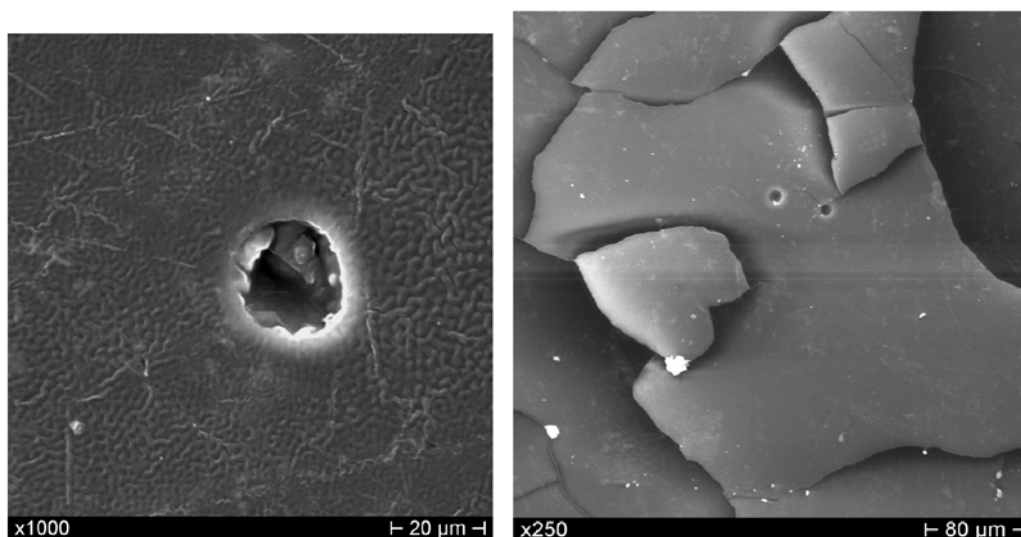


Figure 3.30: Depolymerized linseed oil, due to aging effects.

Fig. 3.30 shows occurred defects over the inner surface of the bakelite, coated with linseed oil (layer of $3-10\mu\text{m}$). The aging effect takes place by means of radicals, notably F^- , which interacts with the polymeric film (which covers the bakelite) breaking it, the effect of this process is a non-uniform surface and of course a non-uniform electrical field. Linseed oil is also very sensible to the respect of the temperature; high temperature could provoke shorts and then high currents, which could led the graphite layer to evaporate.

In the Fig. 3.31 is shown a defect due to NaF contamination, this compound is due to the presence of F^- radical, which is very reactive, and Na, which comes from bakelite (together with many other contaminants).

3. MATERIALS AND THEIR INTERACTION WITH RPC GAS MIXTURE

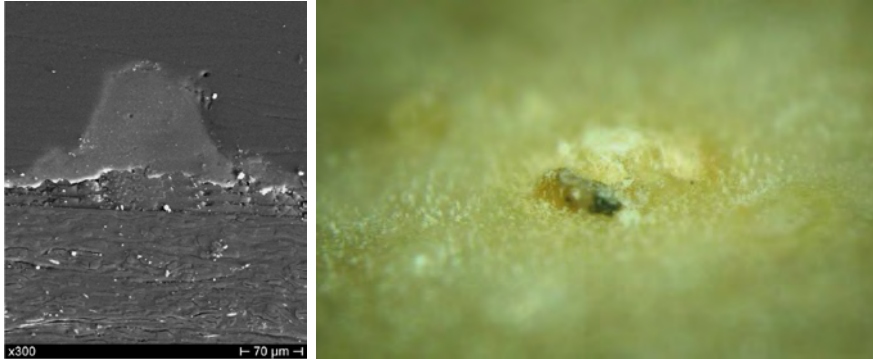


Figure 3.31: Section and prospective view of NaF defect

From the section view of this defect it is clear that the electrical field is much stronger near the collected NaF and this may cause high currents or even local sparks.

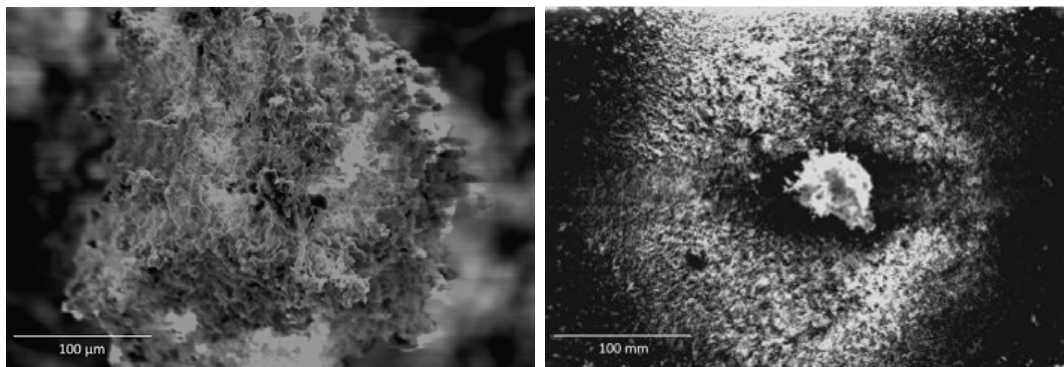


Figure 3.32: Dendrite defect 100 μ m and 1mm

Fig. 3.32 shows similar defects originated by contaminants created due to the presence of high reactive ions as F^- . In Fig. 3.33 the effect of an oil drop on the electric field is shown(25). Once this situation occurs, in some regions the electrical field can reach twice the nominal operating value leading to the transition from avalanche to streamer regime.

3.2 The scaled-down closed loop experimental setup

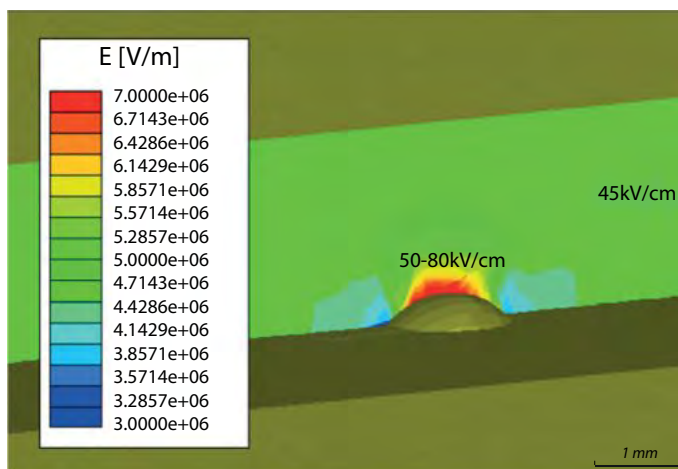


Figure 3.33: Simulation about the effect of a pollutant drop (1mm diameter 0.2mm height) respect to the electrical field inside the RPC 2mm gap.

In particle physics Zachary Malter(26) described this effect actually in detectors exposed to radiation such as electrons, ions, X-rays or extreme/vacuum ultraviolet. A secondary electron emission from the surface of a thin insulating layer results in the production of a positive charge on the surface. This positive charge produces a high electric field in the insulator, resulting in the emission of electrons through the surface. This tends to pull more electrons from further beneath the surface. Eventually the sample replenishes the lost electrons, by picking up the collected secondary electrons through the ground loop.

3.2.6 Conclusions

Resistive Plate Chambers (RPC) detectors are widely used in HEP experiments for muon detection and triggering at high-energy interactions at high-luminosity hadron colliders, in astroparticle physics experiments for the detection of extended air showers, as well as in medical and imaging applications.

In this chapter we have succeed to perform detailed studies and a full characterization of materials and gas contaminants present in the operational gas mixture of the RPC muon detector for the CMS Experiment at the CERN Large Hadron Collider. Alternative and innovative strategies were used to investigated the purification of gas

3. MATERIALS AND THEIR INTERACTION WITH RPC GAS MIXTURE

mixture mandatory to avoid any damage to the RPC chambers. Due to the interactions of the freon-based mixture with the materials adopted, in the RPC gap and in the gas system, several chemically aggressive ions may dramatically destroy the detector. In particular CMS (as also ATLAS experiment) uses a recirculation system (the Closed Loop) that purifies the gas after the RPC chambers employing a system of filter cartridges. The used filter system at this moment consists of metallic filters (Ni-Al, Cu-Zn based), zeolitic filter (Linde type A) and dust metallic filters (installed at the input and output of each cartridge). At the ISR experimental area we have run a scaled-down twin gas system in order to understand all the involved mechanism about the pollutants created during the RPC operation. Better procedures and materials are necessary to optimize the process of purification of the gas mixture as well as the process of filters regeneration since radiation level of LHC will increase and this will affect the production of contaminants which will increase as well.

Quantitative gas chemical analysis were performed online by a complete system which includes gas-chromatography, pH sensors and contaminants (notably HF) detectors. Lifetime of unused purifiers is more than 6 months after that the RPC current of up-stream gap start increasing, while the down-stream gaps show stable currents. This suggests that the first gap acts as a mechanical filter to the second gap which does not receive a polluted gas mixture. The chemical setup confirmed that F^- production is almost constant and the ion gets collected in the system since thanks to preliminary analysis we have found that the regeneration process is not helpful in removing fluorine from the zeolite filter as well as from the metallic filters. During the second run, adopting used purifier material the F^- production was slightly smaller and up-stream currents start increasing after 7 month of operation. The current rising up was in the end bigger as well as the production rate of F^- .

3.3 A device for monitoring gas-material interactions

3.3.1 Introduction

The Gas Gain Monitoring (GGM) system(27) is composed by the same type of RPC used in the CMS detector but of smaller size (2mm thick bakelite, $50 \times 50 \text{cm}^2$). Twelve gaps are arranged in a stack located in the CMS gas area (SGX5 building) in the surface, close to CMS assembly hall (LHC-P5). The Fig. 3.34 shows a layout of the GGM system.

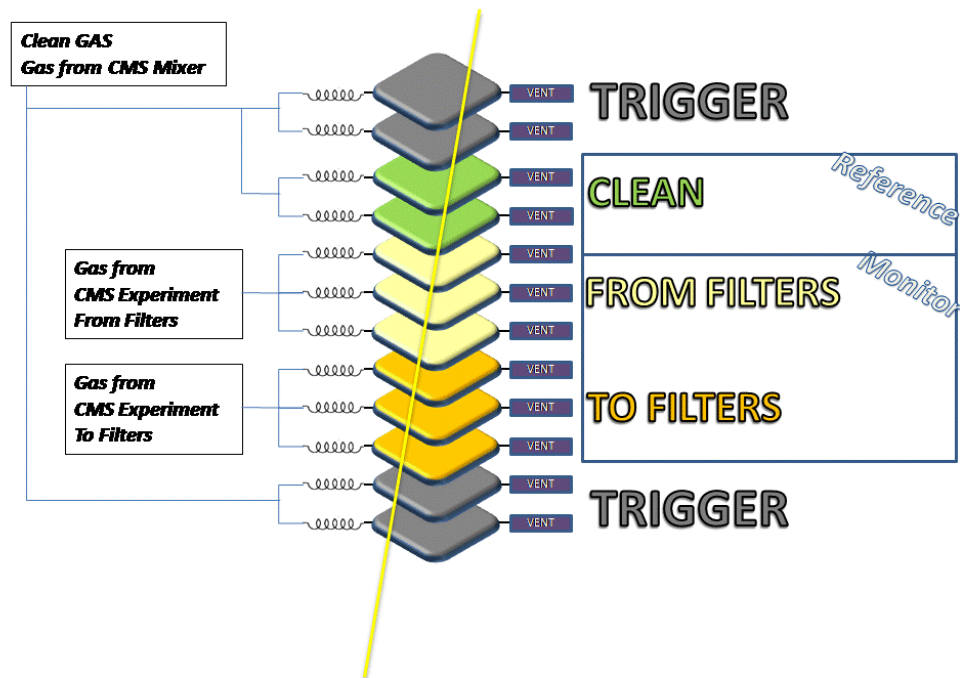


Figure 3.34: Layout of GGM experimental setup

The choice to install the system in the surface instead of underground allows to profit from maximum cosmic muon rates. In order to ensure a fast response to working point shifts with a precision of $\approx 1\%$, 10^4 events are required, corresponding to about 30 minutes exposure time on surface, to be compared with a 100-fold lesser rate underground. The trigger is provided by four out of twelve gaps of the stack, while the remaining eight gaps are used to monitor the working point stability. The eight

3. MATERIALS AND THEIR INTERACTION WITH RPC GAS MIXTURE

gaps are arranged in three sub-system: one sub-system (two gaps) is fluxed with the fresh CMS mixture and its output sent to vent. The second sub-system (three gaps) is fluxed with CMS gas coming from the closed-loop gas system and extracted before the gas purifiers, while the third sub-system (three gaps) are operated with CMS gas extracted from the closed-loop extracted after the gas filters. The basic idea is to compare the operation of the three sub-system and, if some changes are observed, to send a warning to the experiment. In this way, the gas going to and coming from the CMS RPC detector is monitored by using the two gaps fluxed with the fresh mixture as reference gaps. This setup will ensure that pressure, temperature and humidity changes affecting the gaps behavior do cancel out by comparing the response of the three sub-system operating in the same ambient condition. The monitoring is performed by measuring the charge distributions of each chamber. The eight gaps in the first phase were operated at different voltages in order to characterize the RPC chamber response at different regimes but later on it was decided to run all of them at fixed efficiency, $\approx 50\%$ since in this condition the charge sensitivity against a voltage shift is maximized it will be shown later. Comparison of signal charge distributions and the ratio of the avalanche to streamer components of the ADC provides a monitoring of the stability of working point for changes due to gas mixture variations.

3.3.2 Construction and commissioning

Each chamber of the GGM system consists of a single gap with double sided pad read-out: two copper pads are glued on the two opposite external side of the gap. Fig. 3.35 shows a sketch of a chamber whose photos are shown in Fig. 3.36; the two foam planes are used to reduce the capacity coupling between the pad and the copper shields.

3.3 A device for monitoring gas-material interactions

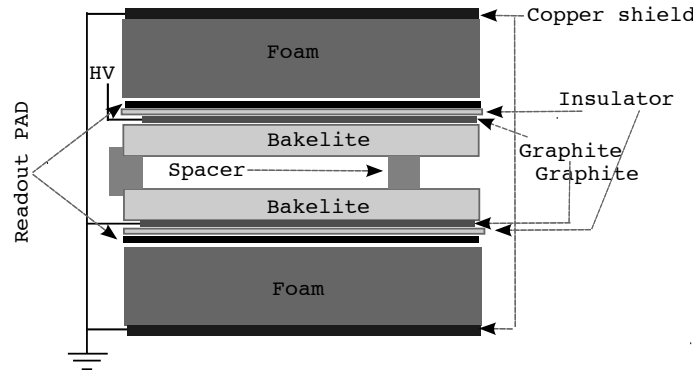


Figure 3.35: A schematic layout of a GGM chamber

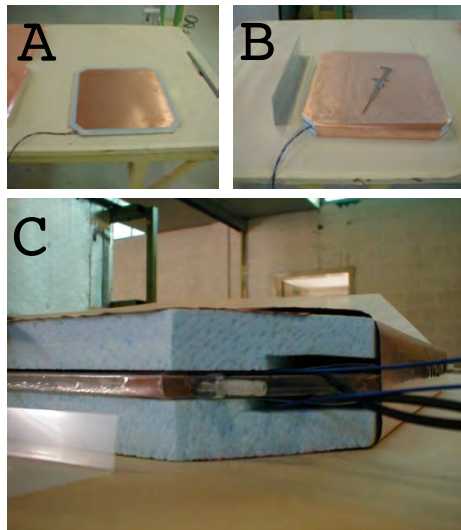


Figure 3.36: Pictures of a GGM gap and chamber. A) A bare gap with the HV and signal cables. B) A completed chamber. The gap is sandwiched between two foam panels and fully covered with a copper shield. C) A section of a chamber with the two foam panels visible.

The signal is read-out by a transformer based circuit A3 (Fig. 3.37). The circuit permits to algebraically subtract the two signal, which have opposite polarities, and to obtain an output signal with subtraction of the coherent noise, with an improvement by about a factor 4 of the signal to noise ratio. Fig. 3.38 shows the typical operation

3. MATERIALS AND THEIR INTERACTION WITH RPC GAS MIXTURE

mode of the GGM double-pad readout with positive and negative pads pulses, and the output pulse from circuit A3. For the charge analysis the output signals from circuit A3 are sent to a CAEN ADC V965A¹.

The GGM has been tested with cosmic rays at LNF and then shipped to CERN for the final commissioning (Fig. 3.39 show the final stack assembly).

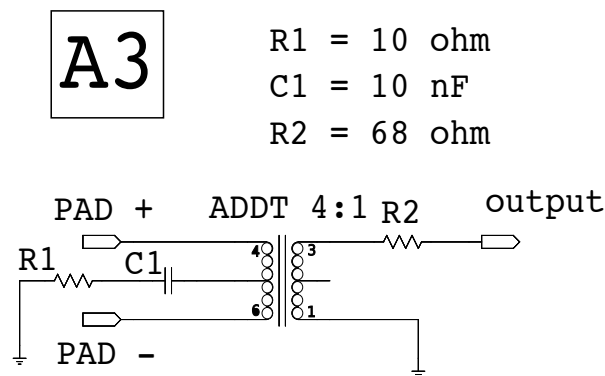


Figure 3.37: The electric scheme of the read-out circuit providing the algebraic sum of the two pad signal (PAD + and PAD -).

¹16 Charge-to-Digital Conversion channels with current integrating negative inputs (50Ω impedance). For each channel, the input charge is converted to a voltage level by a QAC (Charge to Amplitude Conversion) section. Each QAC output is then converted by two ADCs in parallel; one ADC is preceded by a x1 gain stage, the other by a x8 gain stage: a dual input range is then featured: 0 - 900 pC (200 fC LSB) and 0 - 100 pC (25 fC LSB); this allows to avoid saturation with big charge pulses while increasing resolution with small ones. The outputs of the QAC sections are multiplexed and subsequently converted by two fast 12-bit ADCs. The ADCs use a sliding scale technique to improve the differential non-linearity. Programmable zero suppression, multi-event buffer memory, trigger counter and test features complete the flexibility of the unit. The module works in A24/A32 addressing mode; the data transfer occurs in D16/D32/BLT32/MBLT64. The module also supports the chained block transfer (CBLT32/CBLT64) and the multicast commands. The board supports the live insertion that allows inserting or removing it into the crate without switching it OFF. (www.caen.it)

3.3 A device for monitoring gas-material interactions

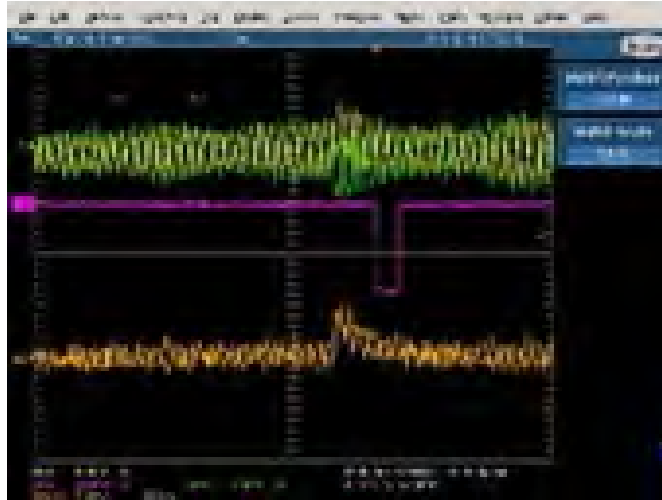


Figure 3.38: An oscilloscope screen-shot of the two pad signals (upper traces) which are effected by a coherent noise and are barely visible on the screen. In the lower trace the coherent noise is highly reduced by A3 circuit. The vertical scale is the same for both cases 5 mV/div.



Figure 3.39: A picture of the GGM system ready to be shipped to CERN. The stack is enclosed into an aluminum box for further shielding.

3. MATERIALS AND THEIR INTERACTION WITH RPC GAS MIXTURE

A typical ADC distribution of a GGM gap is shown in Fig. 3.40 for two different effective operating voltage (HV_{eff}^1), defined as the high voltage set on the HV power supply corrected for the local atmospheric pressure and temperature.

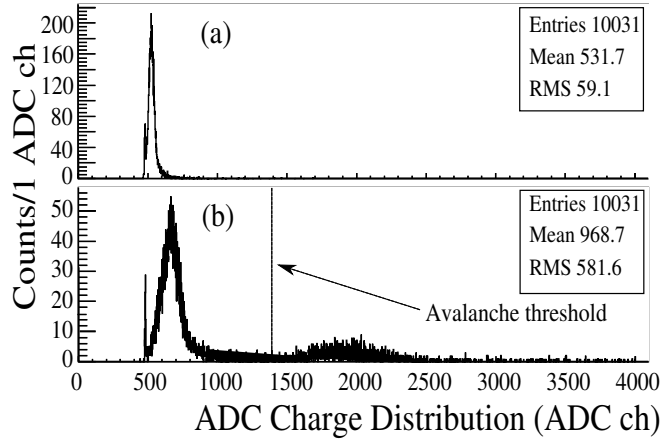


Figure 3.40: Typical ADC charge distributions of one GGM chamber at two operating voltages. Distribution (a) correspond to $HV_{eff} = 9.9\text{kV}$ while distribution (b) to $HV_{eff}=10.7\text{kV}$. In (b) is clearly visible the streamer peak around 1900 ADC channels. The events on the left of the vertical line (1450 ADC channels in this case) are assumed to be pure avalanche events.

Fig. 3.40 (a), corresponding to $HV_{eff}=9.9\text{kV}$, shows a clean avalanche peak well separated from the pedestal. Fig. 3.40 (b) shows the charge distribution at $HV_{eff}=10.7\text{kV}$ with two signal regions corresponding to the avalanche and to avalanche+streamer mode.

¹The effective HV is defined hereby:

$$HV_{eff} = HV \frac{P_0}{P} \frac{T}{T_0} \quad (3.7)$$

where $P_0 = 1010\text{mbar}$ and $T_0=293\text{K}$.

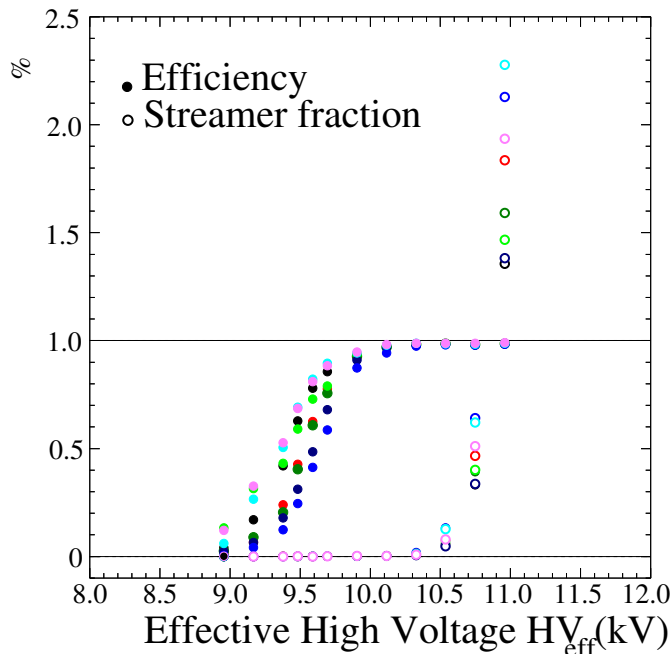


Figure 3.41: Efficiency plot (full dots) of GGM chambers as a function of HV_{eff} . The efficiency is defined as the ratio between the number of ADC entries above $3\sigma_{ped}$ and the number of acquired triggers. Open dot plots correspond to the streamer fraction of the chamber signal as a function of HV_{eff} .

Fig. 3.41 shows the GGM single gap efficiency (full dots), and the ratio between the avalanche and the streamer component (open circles), as a function of the effective high voltage. Each point corresponds to a total of 10000 entries in the full ADC spectrum. The efficiency is defined as the ratio between the number of triggers divided by the number of events above $3\sigma_{ped}$ over ADC pedestal, where σ_{ped} is the pedestal width. The avalanche to streamer ratio is defined by counting the number of entries in the avalanche (below the ADC threshold (Fig. 3.40 b) and above the pedestal region) and dividing it by the number of streamer events above the avalanche threshold. Both efficiency and avalanche plateau are in good agreement with previous results (28). In order to determine the sensitivity of GGM gaps to working point shifts, the avalanche to streamer transition was studied by two methods, the charge method and the efficiency method. In the charge method, the mean value of the ADC charge distribution in the

3. MATERIALS AND THEIR INTERACTION WITH RPC GAS MIXTURE

whole ADC range is studied as a function of HV_{eff} (Fig. 3.42). Each point corresponds to 10000 events in the whole ADC spectrum. In the plot three working point regions are identified

1. INEFFICIENCY ($HV_{eff} < 9.7$ kV);
2. AVALANCHE (9.7 kV $< HV_{eff} < 10.6$ kV);
3. AVALANCHE+STREAMER MODE ($HV_{eff} > 10.6$ kV).

The best sensitivity to working point shifts is achieved in the avalanche+streamer region, estimated to be about 25 ADC ch/10 V or 1.2pC/10V.

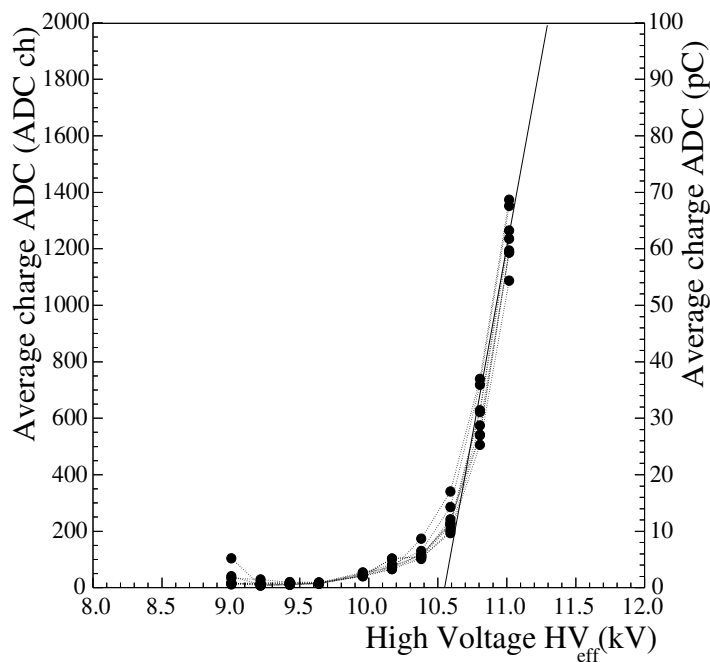


Figure 3.42: Average avalanche charge of the eight monitor chamber signal as a function of HV_{eff} . The slope is about 25 ADC ch/10 or 1.2pC/10V. Each point corresponds to 10000 triggers.

In the efficiency method, the ADC avalanche event yield is studied as a function of HV_{eff} (Fig. 3.43). The avalanche signal increases by increasing the HV applied

3.3 A device for monitoring gas-material interactions

to the gap, until it reaches a maximum value after which the streamer component starts to increase. The 9.0kV-10.0kV shows a sensitivity(29) to work point changes of approximately 1.3%/10V.

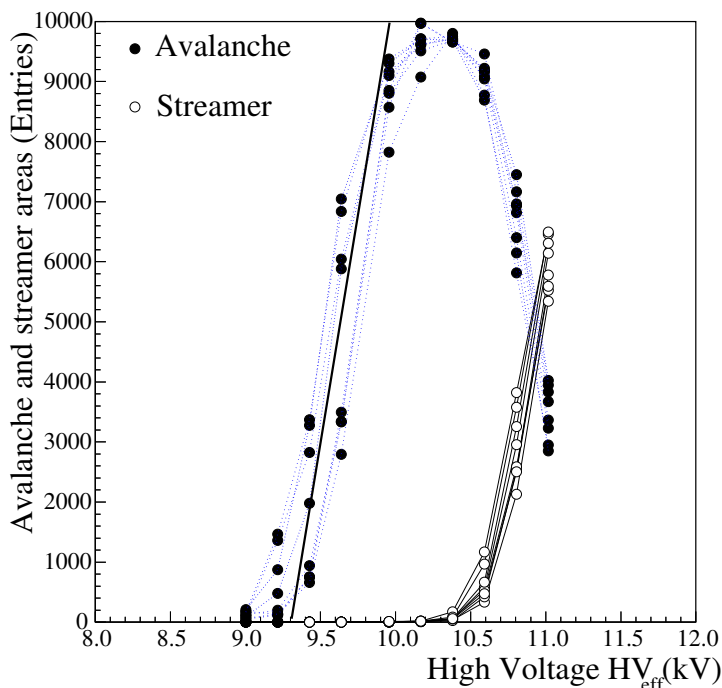


Figure 3.43: Streamer and avalanche yields as a function of HV_{eff} . Each point corresponds to 10000 collected triggers. The solid line has a slope of approximately 130 events/10 V corresponding to a sensitivity of 1.3%/10V.

3.3.3 Software development, Data-Taking and Analysis

The GGM software has been deployed as a RPM package¹ which contains several scripts, analysis tools and the main DAQ software. The main core was written in C(30) using standard UNIX² and CAEN libraries provided with the V965A ADC module.

¹RPM is a package management system. The name RPM refers to two things: software packaged in the .rpm file format, and the package manager itself. RPM was intended primarily for GNU/Linux distributions; the file format is the baseline package format of the Linux Standard Base.

²Multitasking, multi-user computer operating system developed in 1969 by a group of AT&T employees at Bell Labs

3. MATERIALS AND THEIR INTERACTION WITH RPC GAS MIXTURE

The DAQ consists in three packages:

- **gasgainmonitoring**: This is the main core of the system; it reads the CAEN V2718¹ controller of the VME crate where the QDC is installed. After reading correct registers the package takes care of storing raw data into files.
- **trgrate**: This is the trigger rate counter, it performs the calculation of the actual rate of data taking.
- **psxpico**: This package takes care of the environmental monitoring control.

All the above packages start automatically when the computer boots-up and they are always running thanks to background daemons “startup script” and the installed cronjobs² as in Fig. 3.44.

The DAQ has been developed using the XDAQ(31) framework, which is the standard way to integrate data acquisition systems at CMS. The main package “gasgainmonitoring” automatically invokes a fast post-processor written in PAW³ which performs a quick analysis on the raw files. Once the analysis has place, a light DST file is produced and stored; this DST file contains run summary details with the monitored value of each RPC chamber such as: anodic charge, avalanche area, streamer area, streamer/avalanche ratio and efficiency. The raw files are stored on a shared NFS⁴ disk on the CMS online cluster. By using a tool written with ROOT⁵ is possible to retrieve histograms (as example in Fig. 3.40) of the GGM variables. In the Fig. 3.44 a summary of the GGM architecture is shown.

¹This is a VME controller connected by fiber optic to a PCI controller card A2818.

²The name Cron comes from the greek word *chronos*, the ancient god of the time; In UNIX operating system Cron is a time-based job scheduler.

³PAW was developed at CERN in 1986 as an interactive, scriptable computer software tool for data analysis and graphical presentation in HEP.

⁴NFS is a network file system protocol developed by Sun Microsystems in 1984.

⁵R. Brun et al. developed this analysis tool in C++ for HEP Experiment at LHC.

3.3 A device for monitoring gas-material interactions

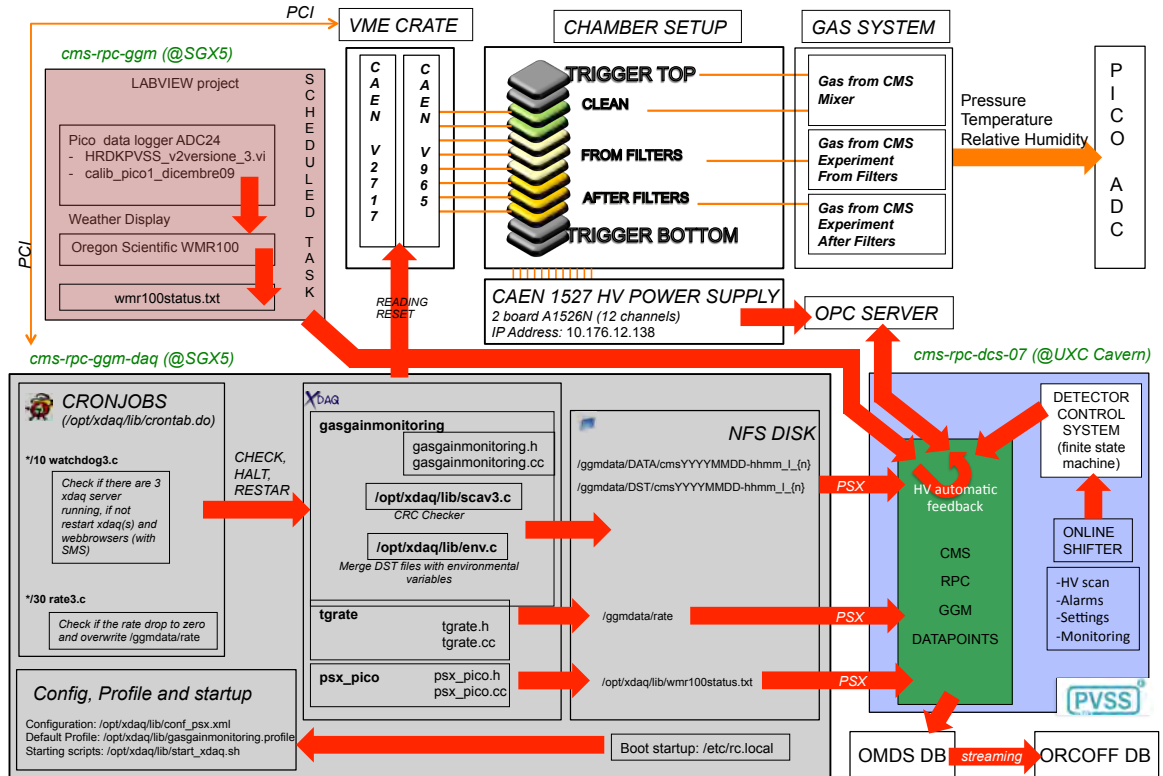


Figure 3.44: GGM data flow software and online tools

The environmental control is performed via *ad-hoc* sensors read with a 12bit PICO(32) ADC connected via USB to a computer. The accuracy of the temperature sensor is $\pm 1^\circ\text{C}$ in the range $0 - 40^\circ\text{C}$ and the resolution is 0.1°C . The relative humidity sensor has an operating range from 2% to 98% with a 0.1% resolution, $\pm 1\%$ absolute accuracy. The barometer operational range is between 700mbar and 1050mbar with a 0.1mbar resolution and a $\pm 1\text{mbar}$ accuracy. The online monitoring system records the ambient temperature, pressure and humidity of the GGM box, as well as the gas mixture temperature before and after each RPC gap, also the pressure and the relative humidity are monitored and recorded both inside the box that contains the RPC stack

3. MATERIALS AND THEIR INTERACTION WITH RPC GAS MIXTURE

and in the gas mixture before and after each gap. A LabVIEW¹ project has been designed in order to read these values, the data are sent through the network to the DAQ computer where the XDAQ jobs run. Environmental conditions and values from DAQ are sent then via PSX server to the main DCS panel and to the CMS official OMDS database. PSX is a system which allows relatively small amounts of data to be exchanged between XDAQ client applications and DCS systems by means of the SOAP² XML protocol. At CMS the online monitoring is performed via PVSS³ which is a commercial cross-platform software adopted by all LHC experiments as Detector Control System (DCS). A small project was developed and integrated into the complex CMS RPC DCS in order to give to the CMS shifter access to full information about the GGM and the gas status itself. The GGM package is available online(33) along with all the source codes.

3.3.4 Results and conclusions

The Gas Gain Monitoring System for the CMS RPC Detector has been described. The commissioning and the software development has been followed since the beginning during the construction phase. The main focus was the software development that ended up with a stand-alone easy installable packages. The GGM is actually taking data with the mission of monitoring any shift of the working point of the CMS RPC detector; analysis results show good sensitivity to working point changes. Results show sensitivity to working point changes in charge distribution:

$$(2.24 \pm 0.05)\text{ADC ch/V}$$

$$(112 \pm 2)\text{fC/V}$$

¹It is a platform and development environment for a visual programming language from National Instruments.

²SOAP is a protocol specification for exchanging structured information in the implementation of Web Services in computer networks. It relies on Extensible Markup Language for its message format, and usually relies on other Application Layer protocols, most notably Remote Procedure Call and Hypertext Transfer Protocol for message negotiation and transmission. SOAP can form the foundation layer of a web services protocol stack, providing a basic messaging framework upon which web services can be built. This XML based protocol consists of three parts: an envelope, which defines what is in the message and how to process it, a set of encoding rules for expressing instances of application-defined datatypes, and a convention for representing procedure calls and responses.

³ Software for Distributed Control System and Process Control System developed by ETM professional control

3.3 A device for monitoring gas-material interactions

and in efficiency:

$$(13.4 \pm 0.7)\text{events/V}$$

$$(1.3 \pm 0.1)\%/(10\text{V})$$

The purpose of GGM is to monitor any shift of the working point of the CMS RPC detector. The system redundancy allows for effectively cancelling out the environmental effects at the 2% level as in Fig. 3.45; this is obtained by means of two-gap ratio of the charge distribution.

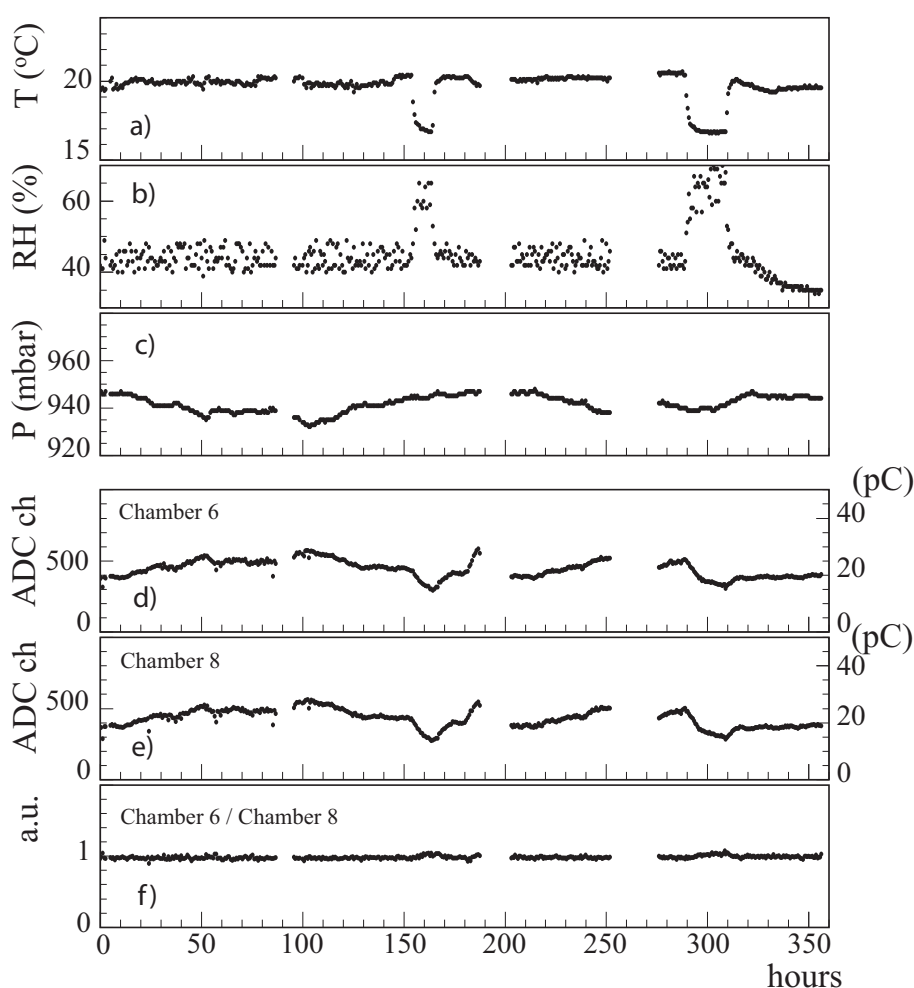


Figure 3.45: Stability of GGM against environment variation common to all gaps, such as atmospheric pressure (a), temperature (b), umidity (c). The charge of two gaps is heavily influenced by environment (d, e), while their ratio shows a 2% stability over several weeks (f).

3. MATERIALS AND THEIR INTERACTION WITH RPC GAS MIXTURE

In April 2011 some concern was raised about the possibility that the CMS gas mixture was slightly changing due to different efficiency plateau obtained from RPC chambers installed in both endcap and barrel. Due to technical problem the GC at CMS was not in operation at that moment but the CMS muon chamber were indicating that there was a shift of working point due to something related to the gas because this effect was globally seen by the totality of the chambers. The GGM was designed to spot a shift of the working point having as reference the clean chambers so in case of a mixer problem which affects also the clean gas mixture the GGM is unable to spot any warning. Anyway looking into the data, (Fig. 3.46) the GGM saw a transition due to the faulty gas mixer.

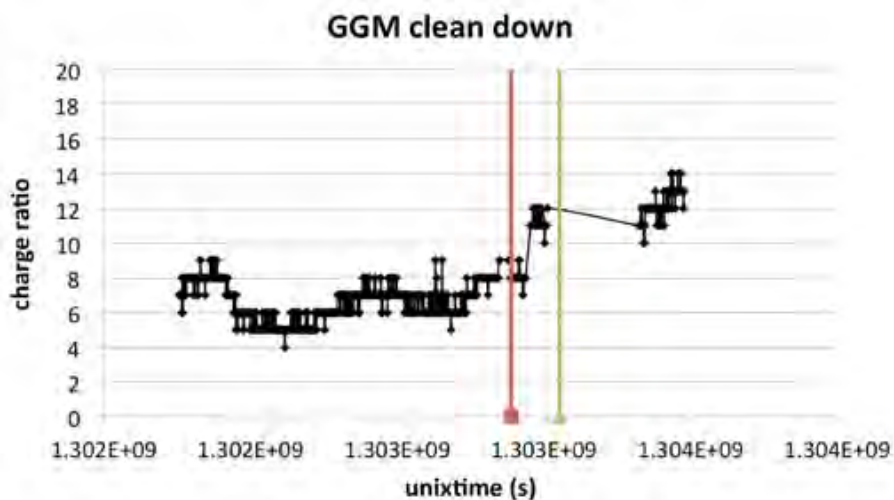


Figure 3.46: Shift of the working point spotted by the GGM due to a faulty SF_6 mass flow meter in the main CMS gas mixer.

The gas group promptly controlled the mixer and realized that the mass flow meter of the SF_6 was not working properly, then it was replaced and calibrated with a new one. With the new mass flow meter the working point shift disappeared.

Finally at the Laboratori Nazionali Frascati (L.N.F.) a twin GGM system is actually installed and operated in the same way as at CMS. This allows to test new software packages and new functions as the HV feedback. As discussed previously RPC are sensitive to environmental variables, then in the GGM variables ratio are used in order

3.3 A device for monitoring gas-material interactions

to remove the environmental dependence. This may not work perfectly in case the RPC gaps behave with very different gain because the HV curve slope could be different. In order to remove environmental dependence what could be done is to adjust the HV according to the environmental variables, notably pressure and temperature. The algorithm can keep stable the effective HV changing the applied HV according to environmental conditions. Moreover, as illustrated in the Sect. 3.4, more complicated relationship between chamber performance and environmental conditions could be found by means of new modeling technique so that the HV feedback correction may increase the precision. In Fig. 3.47 the charge histograms of a gap with stable HV and a gap with stable effective HV are shown. The black histogram shows that when the applied HV is stable the detector is affected by the environmental condition and the anodic total charge collected for each event (muon) is fluctuating. This fluctuation is reduced, red histogram, is the channel works with a constant effective HV.

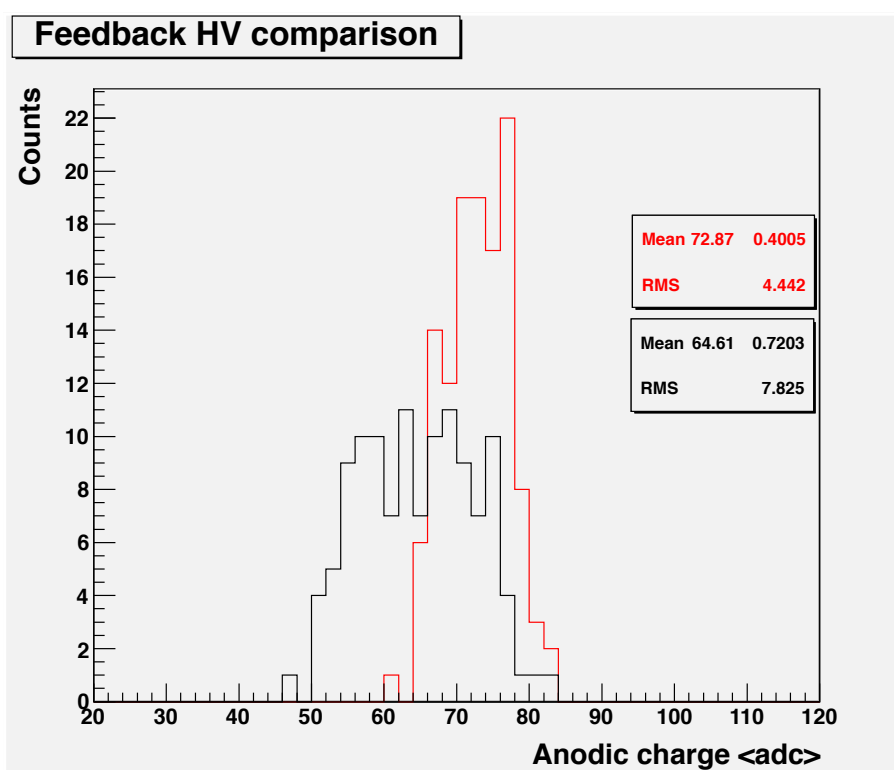


Figure 3.47: GGM with HV feedback for stable operation. In black a channel working at HV=10kV, in red a channel working at $HV_{\text{eff}} = 10\text{kV}$.

3. MATERIALS AND THEIR INTERACTION WITH RPC GAS MIXTURE

Given this promising result we decided to implement this automatic HV feedback even at the GGM installed at CMS. After an initial debugging period the system just worked perfectly as illustrated in Fig. 3.48.

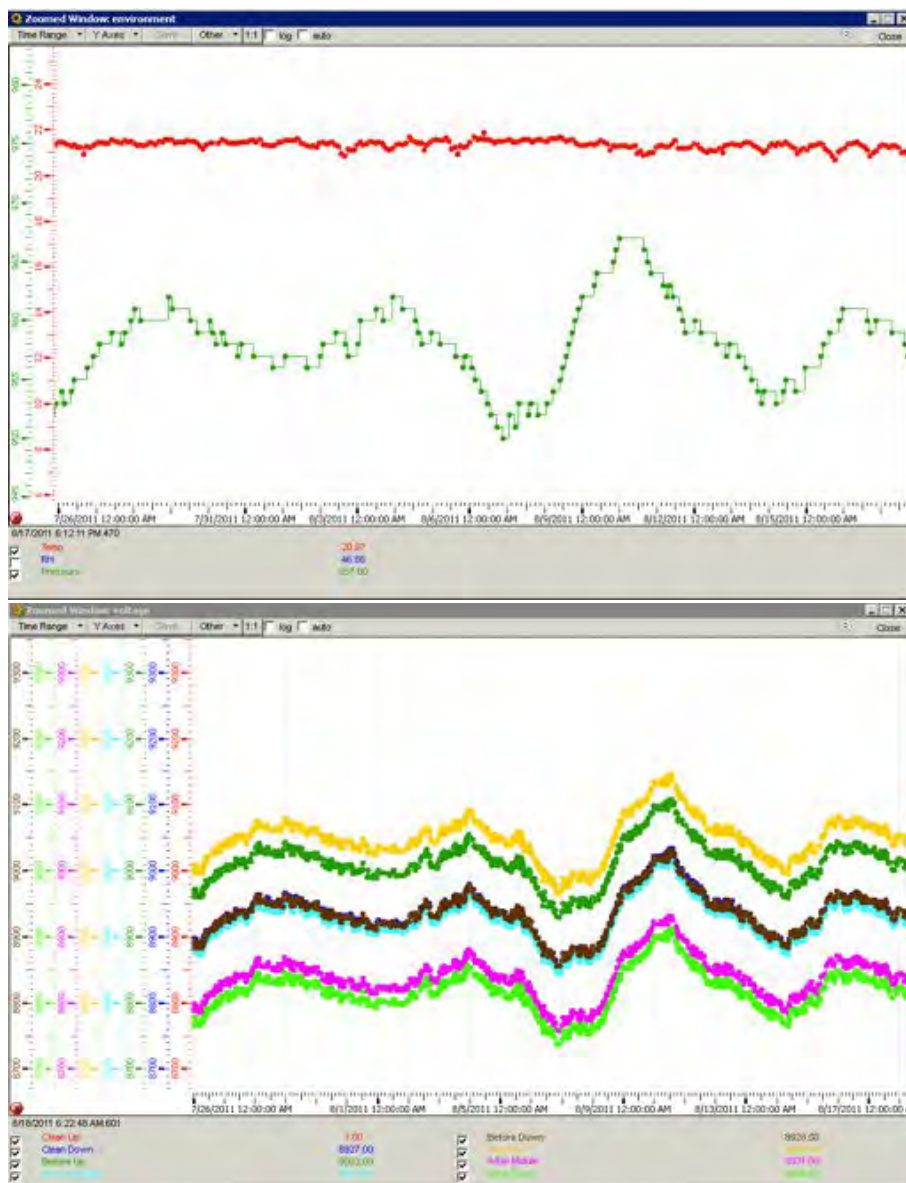


Figure 3.48: CMS GGM HV feedback as monitored by the PVSS central application. The upper plot shows the atmospheric pressure and temperature while the bottom plot shows the applied HV (on each RPC) which follows the atmospheric variables.

3.3 A device for monitoring gas-material interactions

Fig. 3.49 shows a very stable operating system which can spot then eventual pollutant in the gas system promptly and efficiently.

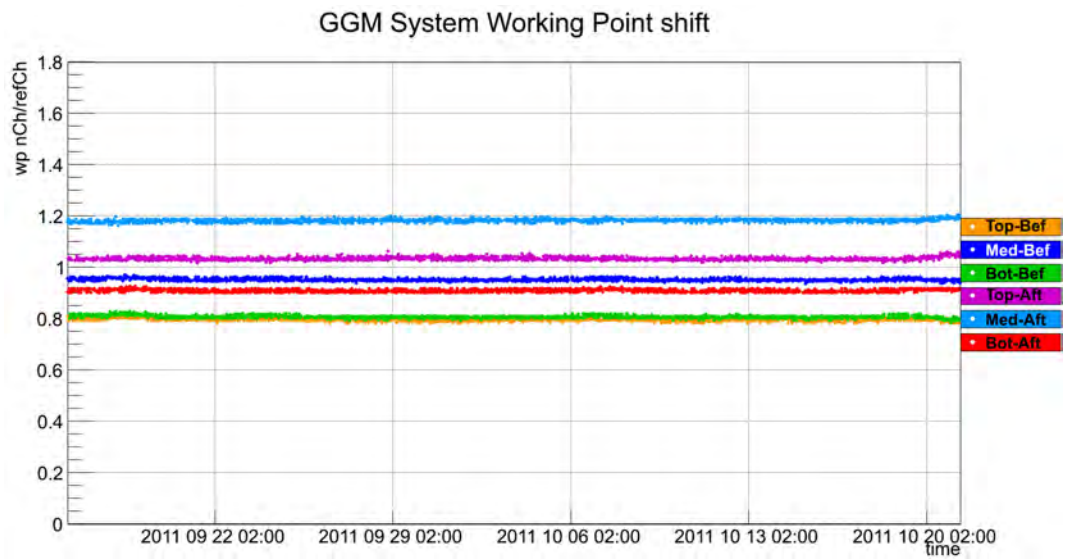


Figure 3.49: CMS GGM working point.

3. MATERIALS AND THEIR INTERACTION WITH RPC GAS MIXTURE

3.4 Towards a theoretical model of gas-material interactions

3.4.1 Introduction

The RPC working principle has been already described in the Sect. 2.2, while pollutant effects are introduced in the Sect. 2.3. The response of RPCs is, however as already mentioned, strongly dependent on environmental parameters such temperature, pressure and relative humidity, as well as on other operational parameters typical of the chosen application, like the radiation dose. The dependence of RPC response from environmental parameters has been studied in the past (34),(35),(36) and several parameterizations have been proposed.

In this thesis a new approach(37) is proposed to model the response of the RPC detector via a multivariate strategy. The algorithm, based on Artificial Neural Networks (ANN), allows to predict the response of RPC's as a function of a set of parameters, once enough data is available to provide a training to the ANN. As initial stage, environmental parameters (temperature T , atmospheric pressure p and relative humidity H) have been considered in this preliminary model. In an initial phase we trained a neural network with just one parameter and we found out, as expected, than the predictions constantly improve after adding parameters into the network. The agreement found between data and prediction has to be considered a pessimistic evaluation of the validity of the algorithm, since it also depends on the presence of unknown parameters not considered in training.

The data for this study have been collected utilizing the gas gain monitoring (GGM) system (Sect. 3.3) of the CMS RPC muon detector, during commissioning with cosmic rays. Results obtained from this study may be applied to the GGM itself to improve the HV feedback correction with more variables and coefficient factors. Parameters such as gas mixture components or contaminants are difficult or impossible to parametrize. Once the response of the RPC detectors will be adequately described by the ANN model described, any discrepancy between prediction and data will provide information on parameters not used in the training, such as material changes, gas contaminants, gas mixture changes, etc.

3.4.2 The Artificial Neural Network simulation code

An Artificial Neural Network (ANN) is an information processing paradigm that is inspired by the way biological nervous systems, such as the brain, process information (38). An ANN is configured for a specific application, such as pattern recognition or data classification, through a learning process. The commonest type of artificial neural network consists of three groups, or layers, of units: a layer of input units is connected to a layer of hidden units, which is connected to a layer of output unit as shown in Fig. 3.50.

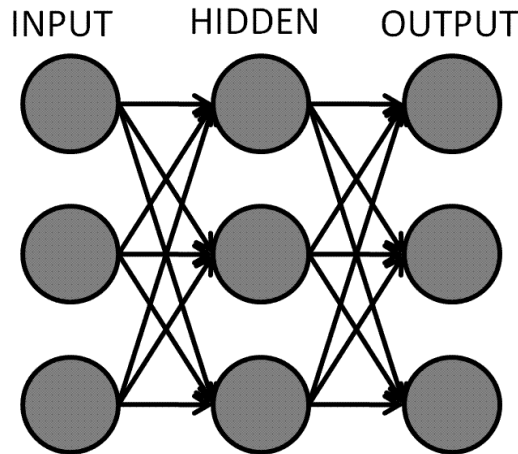


Figure 3.50: Example of a simple Neural Network configuration.

The activity of the input units represents the raw information that is fed into the network. The activity of each hidden unit is determined by the activities of the input units and the weights on the connections between the inputs and the hidden units. The behavior of the output units depends on the activity of the hidden units and the weights between the hidden and output units. For this study temperature, humidity and pressure have been selected as inputs and anodic charge as output. For the ANN an error back-propagation pattern with 3 hidden layers. It was demonstrated (39) that the number of layers is not critical for the network performance, so we decided to go with 3 layers and give to the neural network a sufficient number of hidden units automatically optimized by a genetic algorithm that can take into account several configuration. For each configuration, in each layer there are a number of neurons between 2 and 12,

3. MATERIALS AND THEIR INTERACTION WITH RPC GAS MIXTURE

the genetic algorithm performs the training process with an estimation of the global error; then the configuration is stored and the genetic algorithm continues to evaluate a slightly different configuration. Once the algorithm has taken into account all the possible configurations the best one in terms of global error is chosen. The error is calculated point by point just with the comparison between the neural network forecast and the experimental data. During the training phase the network is taught with environmental data as input, the output depends on the neuronal weights, that at the very beginning are initialized with random numbers. The network output is compared with the experimental data we want to model, and in this phase the network has an estimation of the error, the error itself is back-propagated into the network in order to modify the weights to minimize the error. Once the training is complete the network's weights are optimized to have the minimum error for the chosen network pattern, the genetic algorithm goes on considering several configuration in an automatic way and the really optimal network along with its structure is returned. Such a network is ready to be executed in a none taught period, with different input data. Thanks to this approach it is possible to have a prediction, in terms of charge measurement with a good accuracy, in the future also the dark current will be added as a target parameter in the neural network simulation, and both the charge measurement and the dark current will be used to spot a pathological behavior. In this study the GGM is the system used to train the neural network with charges measurement but this approach will be used more in general with RPC CMS detectors, using the dark current as output variable in the neural network.

3.4.3 Environmental variables and datasets

The GGM experimental setup has been already deeply described in Sect. 3.3. The dataset used is composed of four periods, each period composed of runs. Each run contains 10^4 cosmic ray events where environmental parameters and GGM anodic output charges are collected. The acquisition rate is typically 9.5Hz. Tab.3.5 shows features of the three periods.

3.4.4 Results

Typical simulation outputs show generally good agreement between data and prediction Fig. 3.51. In periods where prediction is not accurate, the discrepancy is typically

3.4 Towards a theoretical model of gas-material interactions

Table 3.5: NN analysis: periods summary table

Periods	Number of runs	Timeline		Environmental range		
		Start	Finish	T (°C)	RH (%)	P (mbar)
1	396	01/09/08	26/09/08	16.5-20.5	35-70	953-970
2	86	27/09/08	01/10/08	16.5-20.5	35-55	962-973
3	460	01/10/08	17/10/08	16.5-22.0	32-60	958-980
4	92	27/10/08	1/11/08	18.5-20.0	35-45	944-960

concentrated in narrow regions ("spikes").

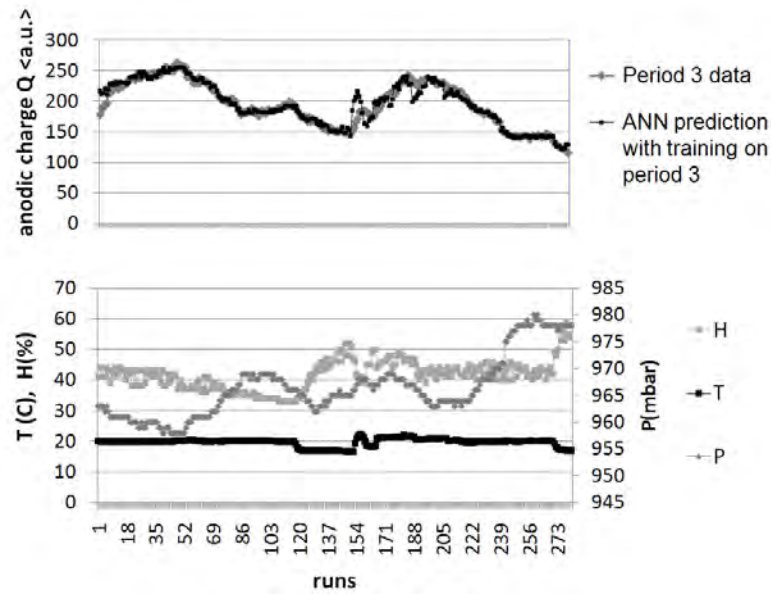


Figure 3.51: Gap 7 trained on 3 - prevision on period 3

The overall agreement between data and prediction is shown in Figs. 3.52,3.53 where the quantity

$$\frac{\Delta Q}{Q} \equiv \frac{Q_{EXP} - Q_{PRED}}{Q_{EXP}} \quad (3.8)$$

is plotted as a function of the experimental points for all four periods, divided for training and prediction respectively. The error distribution for the predictions is much

3. MATERIALS AND THEIR INTERACTION WITH RPC GAS MIXTURE

wider than for the training as expected (Fig. 3.54).

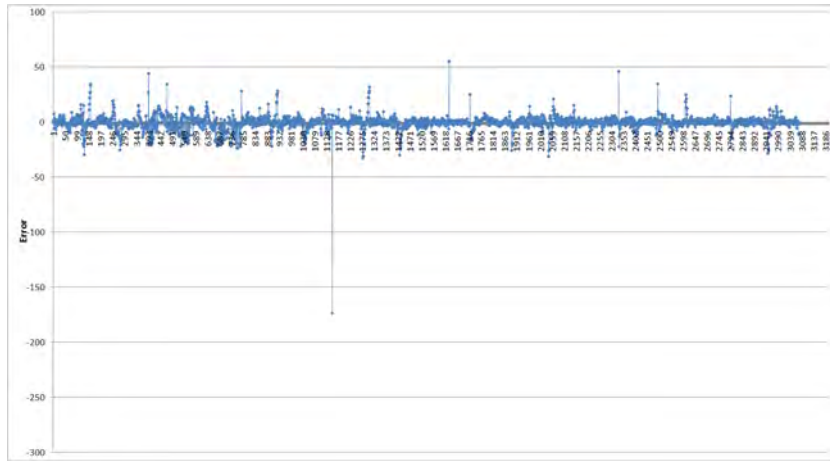


Figure 3.52: Distribution of error for training for all runs.

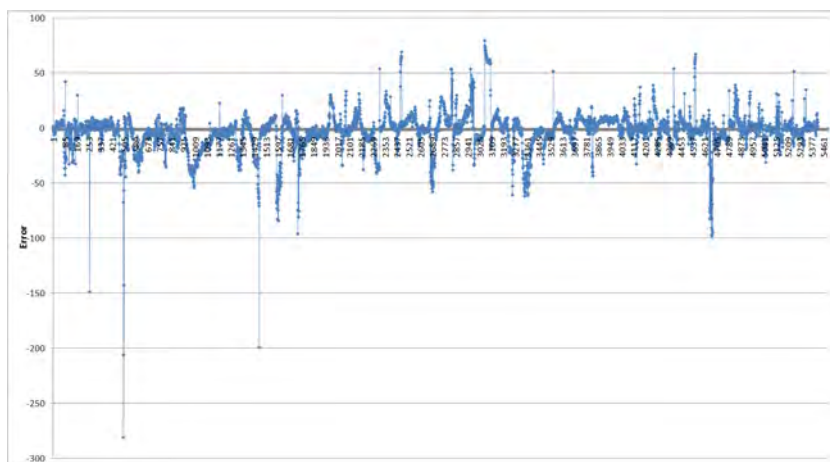


Figure 3.53: Distribution of error for predictions for all runs.

3.4 Towards a theoretical model of gas-material interactions

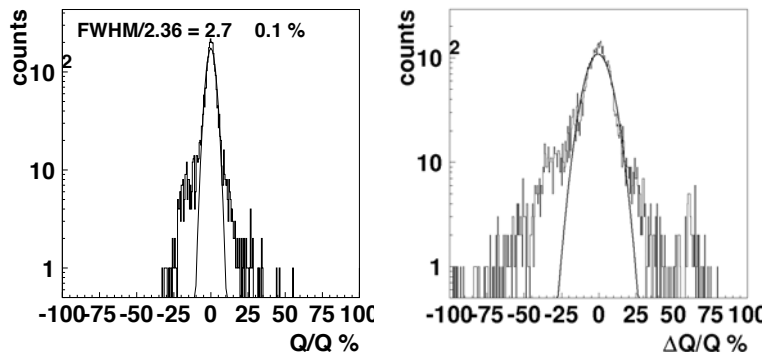


Figure 3.54: Error for training (left) and prediction (right) for all runs. Gaussian fit superimposed.

The distribution of the error for the predictions shows a $\sigma_{fwhm} \sim 7\%$ where $\sigma_{fwhm} \equiv \Gamma_{fwhm}/2.36$ width with very long tails, due to points with very large discrepancy between data and prediction. The cases with very large discrepancy were studied in detail, and found to be characterized by a (p, T, H) value at the edges of the parameter space. Fig. 3.55 shows the correlation between (p, T, H) and error. To quantify the position of each point in the (p, T, H) parameter space, the centroid of the distribution of runs in the (p, T, H) parameter space

$$C_i \equiv \frac{\sum_{i=1, N} x_i}{N} \quad ; \quad \mathbf{x} \equiv (p, T, H) \quad (3.9)$$

and the norm $\|\mathbf{x}\|$ the distance of each run to the centroid

$$\|\mathbf{x}\| \equiv \sqrt{\sum_{j=1,3} (x_j - C_j)^2} \quad (3.10)$$

were computed.

3. MATERIALS AND THEIR INTERACTION WITH RPC GAS MIXTURE

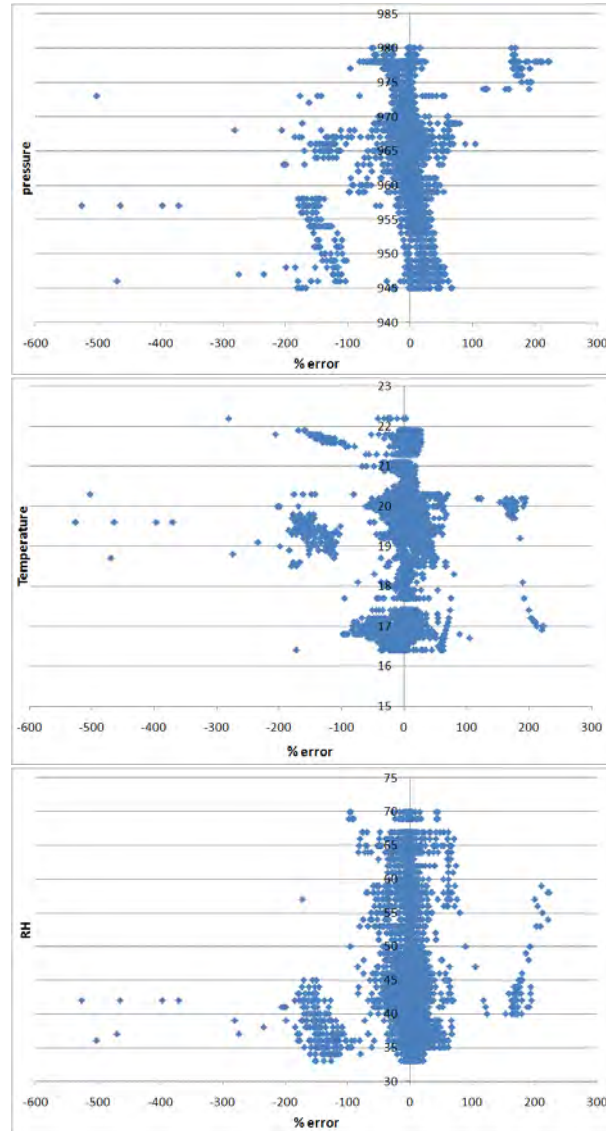


Figure 3.55: (Top) pressure (center) temperature (bottom) humidity versus error $\frac{\Delta Q}{Q}$.

The distribution of the $\frac{\Delta Q}{Q}$ error as a function of the norm $\|\mathbf{x}\|$ (Fig. 3.56) shows three distinct structures. The satellite bands with very large error were studied in detail. All data point in such bands belong to period four and channel six for which problems were detected. Period four and channel six therefore were excluded in the analysis. The distribution of the error as a function of r_b after this selection is shown in Fig. 3.57, with a $\sigma fwhm \sim 4\%$ width and nongaussian tails extending up to $\frac{\Delta Q}{Q} = 200\%$.

3.4 Towards a theoretical model of gas-material interactions

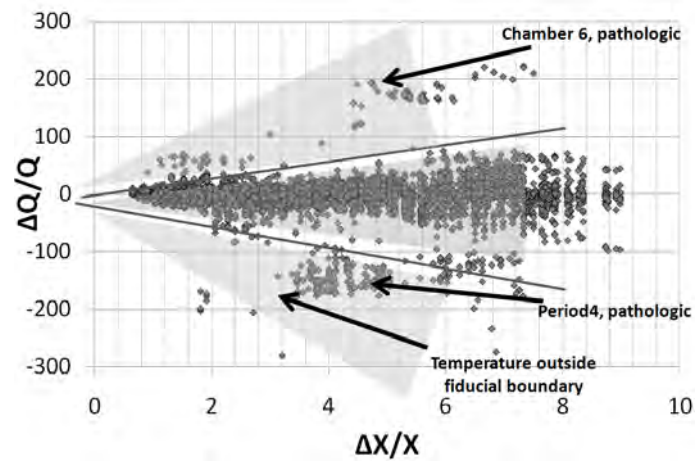


Figure 3.56: Distribution of error as a function of the $\|x\|$ norm for all runs, six chambers and both training and prediction.

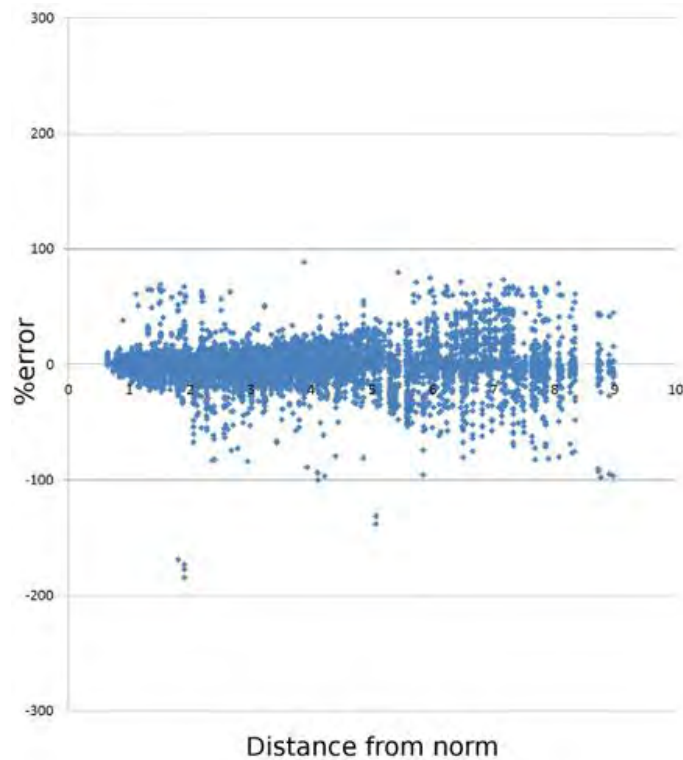


Figure 3.57: Error $\frac{\Delta Q}{Q}$ vs norm $\|x\|$ after selection cuts.

3. MATERIALS AND THEIR INTERACTION WITH RPC GAS MIXTURE

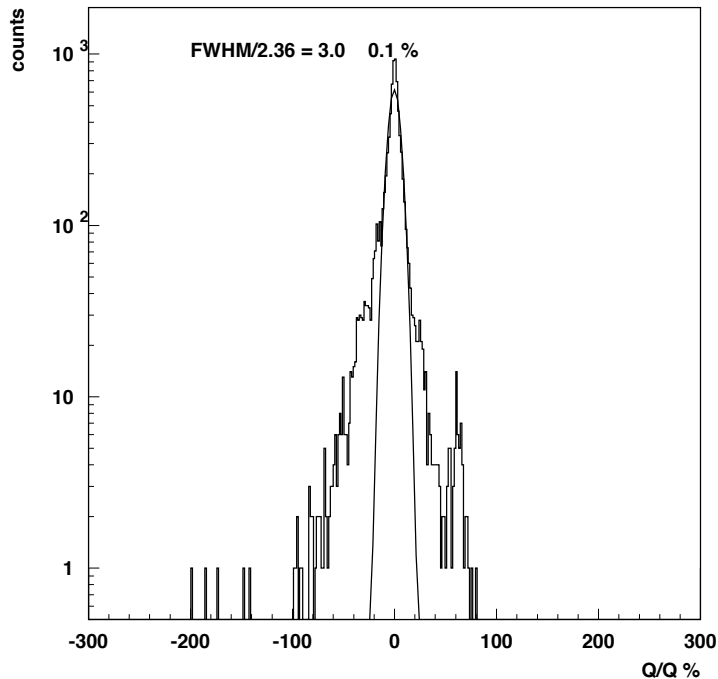


Figure 3.58: Distribution of errors for all norms $\|\mathbf{x}\|$. Gaussian fit superimposed, showing large nongaussian tails.

A selection on the fiducial volume (f.c.) in the \mathbf{x} parameter space (Tab. 3.6) was applied in order to avoid runs on the boundaries of the (p, T, H) space. After the selection cuts, predictions on two periods based on training on the third period were performed. Results are shown in Fig. 3.59 to Fig. 3.67. The selection cuts provide $\sigma_{fwhm} \sim 5\%$ error, as summarized in Tab.3.7.

Table 3.6: Synopsis of selection cuts for fiducial volume.

$(958 < p < 968)\text{mbar}$	$(19.4 < T < 20.4)^\circ\text{C}$	$(34 < H < 44)\%$
------------------------------	-----------------------------------	-------------------

3.4 Towards a theoretical model of gas-material interactions

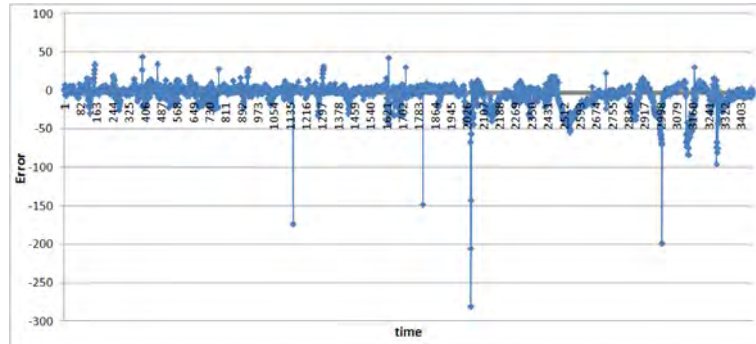


Figure 3.59: Period 1 training, prediction on periods 2 and 3.

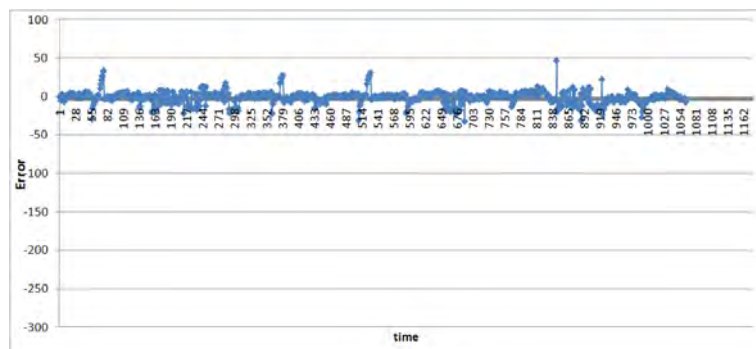


Figure 3.60: Period 1 training, prediction on periods 2 and 3, fiducial selection.

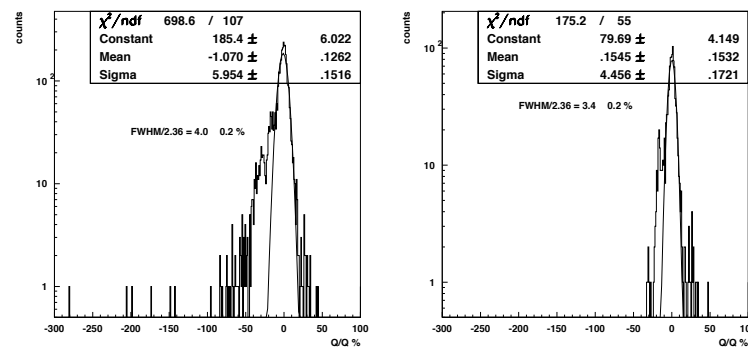


Figure 3.61: Period 1 training, prediction on periods 2 and 3, (left) no cuts, (right) fiducial cut, gaussian fit superimposed.

3. MATERIALS AND THEIR INTERACTION WITH RPC GAS MIXTURE

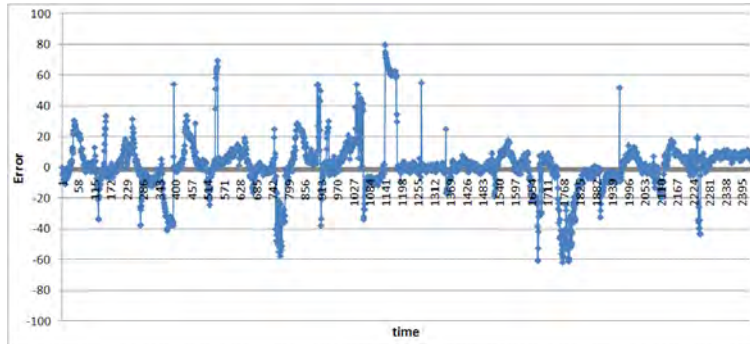


Figure 3.62: Period 2 training, prediction on periods 3 and 1.

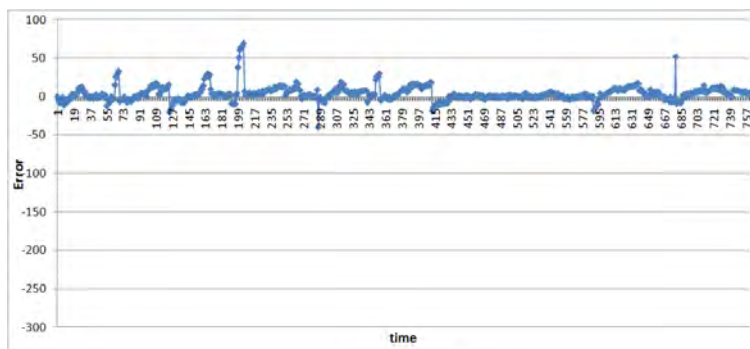


Figure 3.63: Period 2 training, prediction on periods 3 and 1, fiducial selection.

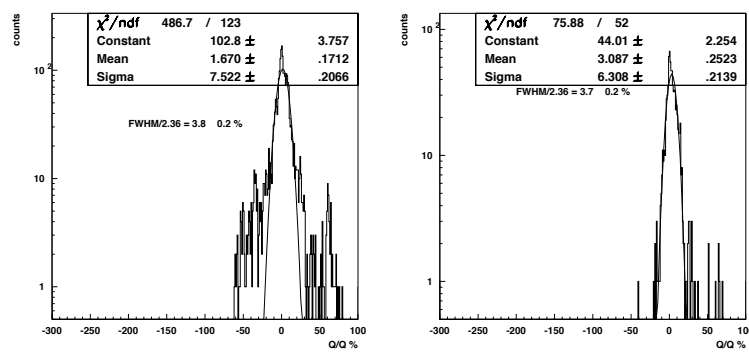


Figure 3.64: Period 2 training, prediction on periods 3 and 1, (left) no cuts, (right) fiducial cut, gaussian fit superimposed.

3.4 Towards a theoretical model of gas-material interactions

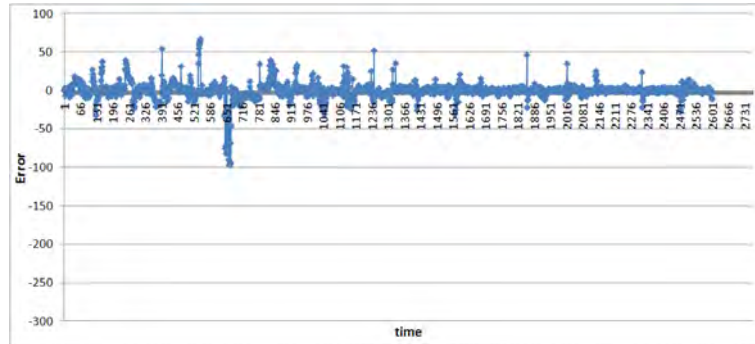


Figure 3.65: Period 3 training, prediction on periods 1 and 2.

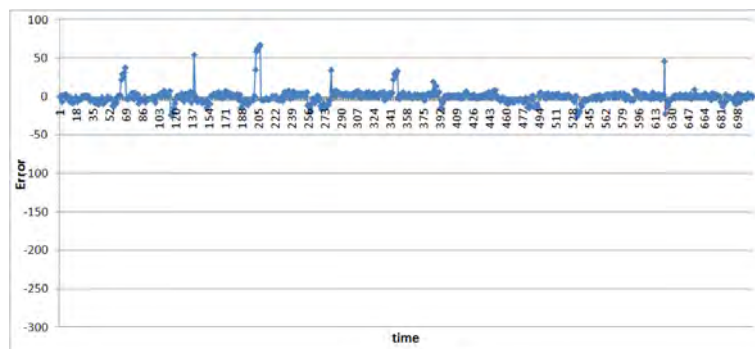


Figure 3.66: Period 3 training, prediction on periods 1 and 2, fiducial selection.

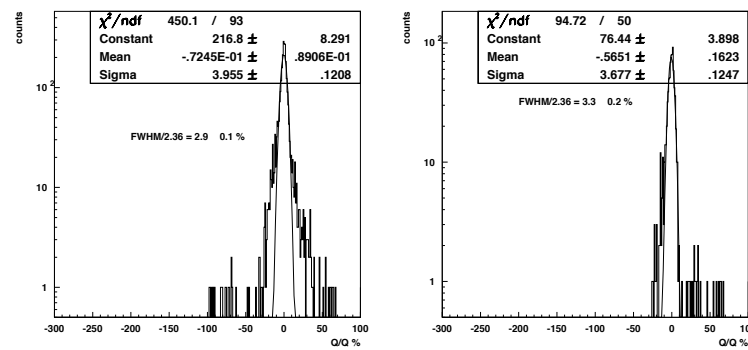


Figure 3.67: Period 3, prediction on periods 1 and 2, (left) no cuts, (right) fiducial cut, gaussian fit superimposed.

3. MATERIALS AND THEIR INTERACTION WITH RPC GAS MIXTURE

Table 3.7: Summary of errors σ_{fwhm} and nongaussian tails (ngt) for various selection cuts and samples.

Data sets	$\frac{\Delta Q}{Q}$	ngt counts	%ngt
All six chambers, all four periods training (train.)	2.7 ± 0.1	123	2.26%
All six chambers, all four periods prediction (pred.)	6.7 ± 0.1	358	6.60%
Chamber six and period four excluded pred.	3.0 ± 0.1	251	4.63%
Pred. on periods 2 and 3, train. on period 1	4.0 ± 0.2	273	3.52%
Prediction on periods 3 and 1, train. on period 2	3.4 ± 0.2	229	2.95%
Pred. on periods 1 and 2, train. on period 3	3.8 ± 0.2	127	1.63%
Pred. on periods 2 and 3, training on period 1, f.c.	3.7 ± 0.3	38	0.49%
Pred. on periods 3 and 1, training on period 2, f.c.	2.9 ± 0.1	77	0.98%
Pred. on periods 1 and 2, training on period 3, f.c.	3.3 ± 0.2	23	0.29%

3.4.5 Conclusions

A new approach based on ANN in modeling the response of RPC detectors was presented, and preliminary results obtained with data from the CMS RPC GGM system were described. The model, once trained on the response of a detector well within the parameter space (p, T, H) , is able to predict the response in other periods with a better than $\sigma_{fwhm} \sim 10\%$ accuracy. With this approach it is possible to model the RPC response in terms of anode charge; this prediction once demonstrated in good agreement with experimental data, can be a very useful tool to spot pathological behavior for example due to pollutants in the gas mixture. Besides the anode charge, also the dark current is an important indicator of the chamber performance and studies are in progress to use the dark current in the training phase. The use of the dark current will be very important in operating and maintaining the CMS RPC detector, where the current of hundred of chambers is monitored and recorded online without any environmental correction. This approach, once properly trained, could spot immediately and online pathological chambers whose behavior is shifting from the normal one. Further studies are in progress to determine and cure the residual nongaussian tails of the $\frac{\Delta Q}{Q}$ errors distributions, to deal with training and prediction on detectors with different high voltage supply, to widen the sample of environmental conditions, and in adding new dimensions to the parameter space such as radiation levels.

3.5 A proposal for new materials

3.5.1 Introduction

Although bakelite is the most common material used in the RPC chambers, thanks to its properties and low price, new materials and coatings have been investigated for the construction of medium-sized RPCs. The bakelites with good electrical properties and coated with silicone have been used to build RPCs of various sizes ($30 \times 30\text{cm}^2$ and $1 \times 1\text{m}^2$ operated in streamer mode and $10 \times 10\text{m}^2$ operated in avalanche mode) showing more than 92% efficiency and about 2 ns time resolution for long-term operations. In order to study the suitability of this material for operation in high dose environment, these chambers are exposed to a high flux of photons at the Gamma Irradiation Facility at CERN. The goal is to monitor the performance during and after the irradiation dose to validate long term operation in avalanche and streamer modes. Preliminary results on validation of the new materials and subsequent chamber operation are presented. The prototype RPC chamber was assembled with a single-gap (2mm) made of high resistive ($\rho \sim 10^{10} - 10^{12}\Omega\text{cm}$) bakelite paper laminates produced and commercially available in India. The bakelite used for the small prototype is of P-120 grade (P-120, NEMA LI1989 Grade XXX), which is used for high voltage insulation under humid conditions. A thin coating of silicone is applied to the inner surfaces of the bakelite sheets used for making the gas gap. In India, silicone coated chambers, operated in the streamer mode using argon, tetrafluoroethane (R-134a) and isobutane in 34:59:7 mixing ratio, prepared by a gas mixing and flow control unit(40) have been tested with cosmic rays(41).

3.5.2 Preliminary tests

This small prototype has been assembled and preliminarily tested in India, for efficiency, noise rate, dark current, time resolution and long term stability in streamer mode in a cosmic stand(42). The chamber was then shipped to CERN where new tests have been carried out.

3. MATERIALS AND THEIR INTERACTION WITH RPC GAS MIXTURE



Figure 3.68: Experimental setup for the small high-resistivity bakelite RPC.

A separate cosmic stand has been built (Fig 3.68), using two little scintillators in coincidence. We have used the CMS standard gas mixture (95.7% $C_2H_2F_4$ - 4.0% Iso- C_4H_{10} - 0.3% SF_6 humidified at about 40%) and a high voltage of 10kV has been applied. We set up an online current monitoring and recording system in order to test the long term stability. After these preliminary tests at the ISR cosmic stand, we moved the small prototype to the Gamma Irradiation Facility (GIF), (at meyring CERN site) where a $^{137}Cesium$ source is irradiating the environment. During this installation we developed the mechanical support for the chamber and online monitoring of radiation, current and environmental parameters such as temperature, pressure, humidity etc. in order to keep track of the chamber performance and environmental changes.

3.5.3 Results

This prototype has readout strips in x-y axis, this means that we are able to locate in the two dimensional space where the chamber was fired by the muons. We developed a software that is able to reproduce a coincidence between two readout strips, in order to obtain the 3D-plot as shown in Fig. 3.69. Although the event distribution is not constant, there are no dead zone, so the efficiency is homogeneous all over the chamber.

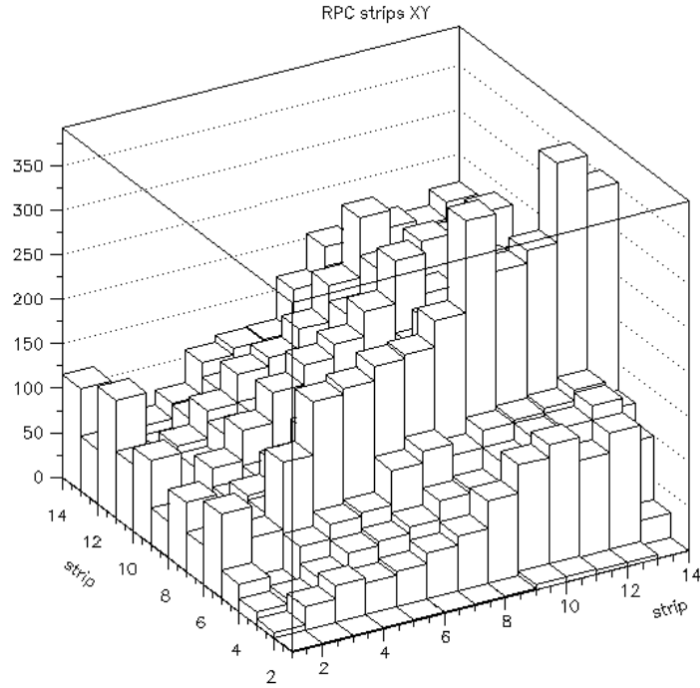


Figure 3.69: Surface plot of the small RPC high-resistivity prototype

An efficiency scan performed earlier in India, reached full efficiency at around 10kV (Fig. 3.70). The same test has been reproduced once the chamber arrived at CERN.

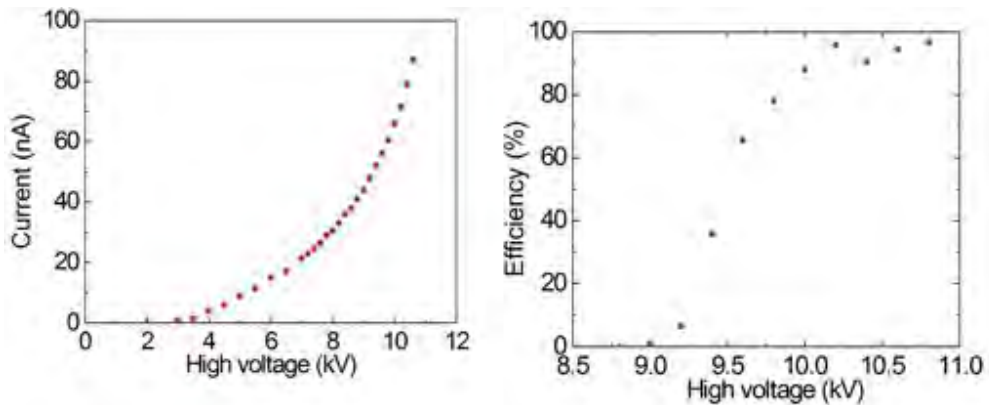


Figure 3.70: RPC prototype with high-resistivity bakelite: I-V plot and the efficiency scan with CMS standard gas mixture.

At the ISR Forward RPC Laboratory, the chamber, in the *ad – hoc* cosmic stand

3. MATERIALS AND THEIR INTERACTION WITH RPC GAS MIXTURE

reached full efficiency as we can see in Fig. 3.71. The prototype chamber was then installed in the CERN GIF experimental area, in order to be irradiated with a gamma source and the chamber performances are monitored. During two months the chamber was irradiated with a nominal photon flux of $5.109\text{m}^{-2}\text{s}^{-1}$. The current and high voltage as well as environmental parameters and gas parameters were recorded. After the irradiation, the chamber was reinstalled in the CERN ISR cosmic stand in order to compare the performances before and after the irradiation. Preliminary results show that chamber behavior did not change substantially with radiation exposure.

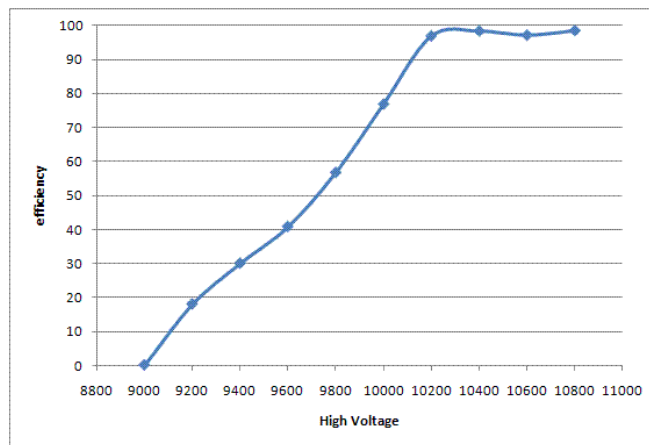


Figure 3.71: RPC prototype with high-resistivity bakelite: Efficiency scan with CMS standard gas mixture.

3.5.4 Conclusions

In conclusion, a small ($10 \times 10\text{cm}^2$) RPC prototype with a new kind of bakelite has been tested and preliminary results are promising in terms of time resolution (42), long term stability and efficiency. The prototype described here is found to work well in both avalanche and streamer modes. It also sustained its performance when operated for more than four months with and without high flux of radiation. A systematic long term study with temperature effects has to be done in order to fully characterize this promising new kind of bakelite.

4

Beyond RPC, Gas Electron Multipliers detector

4.1 An overview

In this chapter a completely new work on a new detector has been carried out. After a long characterization on small size detectors (Sect. 4.5) a new full-size detector (described in Sect. 4.6) has been designed and built; it represents an upgraded version of the already described RPC technology. The industrial technological progress makes available year after year new and new technologies which can be adopted to develop detectors with enhanced performance. MPGD technology, shown in Sect. 4.2.1, represents a very interesting case-study where the adoption of advanced processes used in micro-electronics had an impact on the design of detectors for High Energy Physics. This full-size developed detector, object of this work, relies on a MPGD technology and it depicts the state-of-the-art breaking the word's record in size between analog detectors. This detector has been fully tested in several beam tests as detailed in the Sect. 4.7. All tests ended up successfully with very positive and original published results shown in the Sect. 4.9. All the hardware solutions and developed software (Sect. 4.8), which allowed the construction and characterization of this prototype, constitute also a very original work. This work is going to be proposed officially to the CMS collaboration as an upgrade project, then a Technical Design Report (TDR) will be submitted by march 2012.

4.2 Introduction

The CMS muon system, relies as on three detector technologies: DT, CSC and RPC as shown in the Sect. 2.1. The DT and CSC provide precision tracking functions, while RPCs provide fast trigger thanks to their excellent time resolutions (Sect. 2.2). As in Fig. 4.1, up to $\eta^1 = 1.6$ the forward muon region is instrumented with RPCs. For region with high $|\eta| > 1.6$, during the CMS commissioning and construction, several concerns were raised on whether RPCs would be able to sustain the very hostile environment of the high- η region; it was decided not to instrument this area at all.

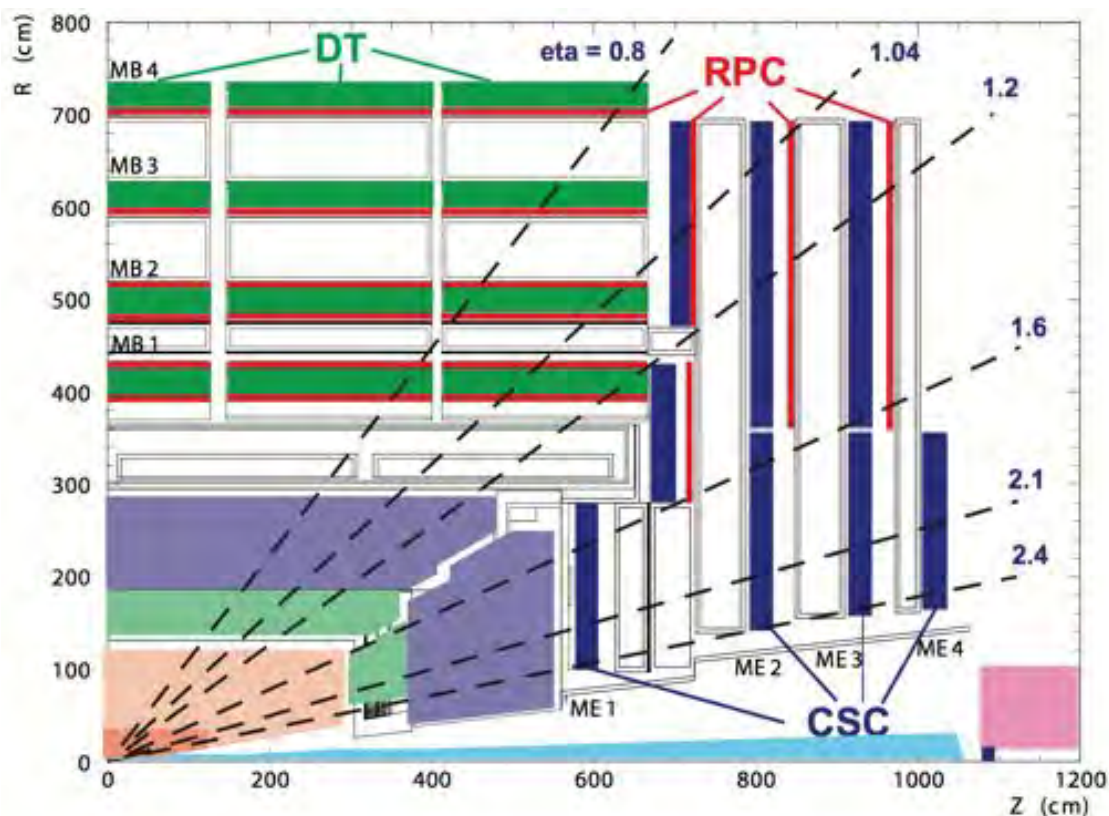


Figure 4.1: CMS section with designed RPC layers.

¹ η is the pseudorapidity defined by:

$$\eta = \frac{1}{2} \ln \left(\frac{|\vec{p}| + p_L}{|\vec{p}| - p_L} \right) \quad (4.1)$$

where p_L is the component of the momentum p along the beam axis.

4. BEYOND RPC, GAS ELECTRON MULTIPLIERS DETECTOR

Gas Electron Multipliers (GEMs)(43) are an interesting technology for the future upgrade of the forward region of the muon system since they can provide precision tracking and fast trigger information simultaneously: moreover they can be designed with sufficiently fine segmentation to cope with high particle rates at LHC and its upgrades in the η region to be covered; Fig. 4.2 shows the charged particle flux at the CMS detector, the region at high- η reaches a particle flux of few kHz/cm². Anyway the construction of GEM detectors is complicated and requires several expertise; large GEM detectors are even more complicated and object of this thesis is the design and construction of the largest GEM detector ever built.

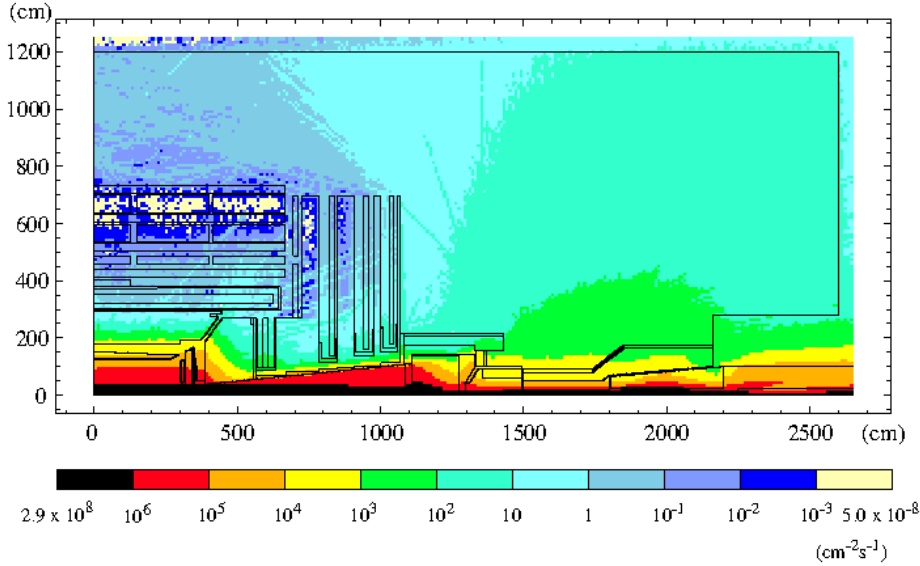


Figure 4.2: Charged particles (hadrons and muons) fluxes in the CMS detector and experimental area. The data are from latest Fluka simulation and correspond to LHC peak luminosity ($10^{34}\text{cm}^{-2}\text{s}^{-1}$).

4.2.1 MPGD and GEM detector

Micro Pattern Gas Detectors (MPGD¹) are relative new gaseous detectors characterized high performance if compared for example to wire chamber where slow drifting ions cause space charge effects, which limits the rate capability to 10–100kHz/cm². On

¹The invention of Micro-Pattern Gas Detectors offered the a big potential for developing new gaseous detectors with unprecedented spatial resolution, high rate capability, large sensitive area, operational stability and radiation hardness.

the contrary in MPGD the rate capability is typically limited by discharge probability rather than space charge effects bringing up the sustainable rate about two orders of magnitude with respect to wire-chambers; GEMs reach the highest rate capabilities among gas detectors.

GEM is a MPGD whose development has seen a lot of interest thanks to special industrial processes more and more available which allow the construction of relatively large size GEMs(44). They were invented in 1998(43), initially for high-energy physics, and were produced by means of photolithographic process. This process has been widely used in the printed circuit industry, nowadays thanks to big companies industrial techniques (more and more advanced, new processes) are available cheaper machine: this is the key which helped GEM in their development.

The basic element of a GEM detector is a thin composite insulator sheet of Kapton¹ with two metal copper layers (electrodes) on the top and the bottom of the insulator sheet. The foil is patterned with microscopic holes, realized by the conventional photolithographic methods, where a strong electric field is created by applying voltages on the GEM copper electrodes. Fig. 4.3 depicts the foil pattern and the electrical field generated by an applied potential difference (typically 420V) between the top and the bottom of the foil.

¹Kapton is a polyimide film developed by DuPont. Kapton remains stable in a very wide range of temperature (1-673K). Kapton is used in, among other things, flexible printed circuits and flexible electronics. Kapton-insulated wiring has been widely used in electrical wiring of civil and military aircraft because it is lighter than other insulators and has good insulating and temperature characteristics. For these reasons Kapton was used extensively in the Apollo program (NASA); space agencies still are adopting Kapton in several application such as the Space Shuttle and the new sunshield of the James Webb Space Telescope. The chemical name for Kapton K and HN is poly(4,4'-oxydiphenylene-pyromellitimide). It is produced from the condensation of pyromellitic dianhydride and 4,4'-oxydiphenylamine. Kapton synthesis is an example of the use of a dianhydride in step polymerization. The intermediate polymer, known as a "poly(amic acid)," is soluble because of strong hydrogen bonds to the polar solvents usually employed in the reaction. The ring closure is carried out at high temperatures (473-573K).

4. BEYOND RPC, GAS ELECTRON MULTIPLIERS DETECTOR

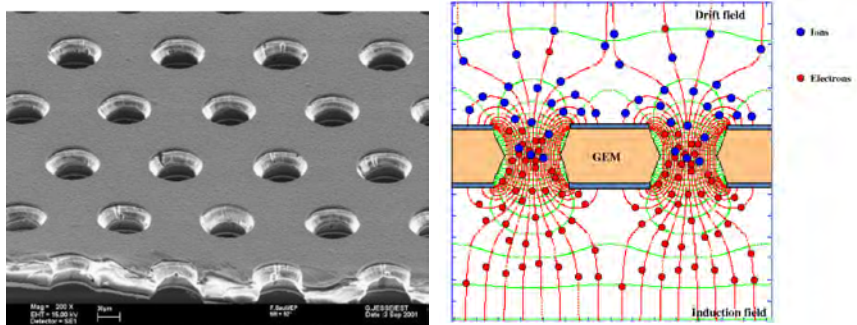


Figure 4.3: GEM foil pattern (left), electrical field inside the GEM gap (right).

The strong electric field allows to transfer charge with an amplification factor which may vary between 10 and 20. This is the reason why, normally, GEMs are used in stacks in order to achieve higher gain, each GEM foil contributes to the gain limiting the voltage applied to the foils and therefore minimizing spark probability.

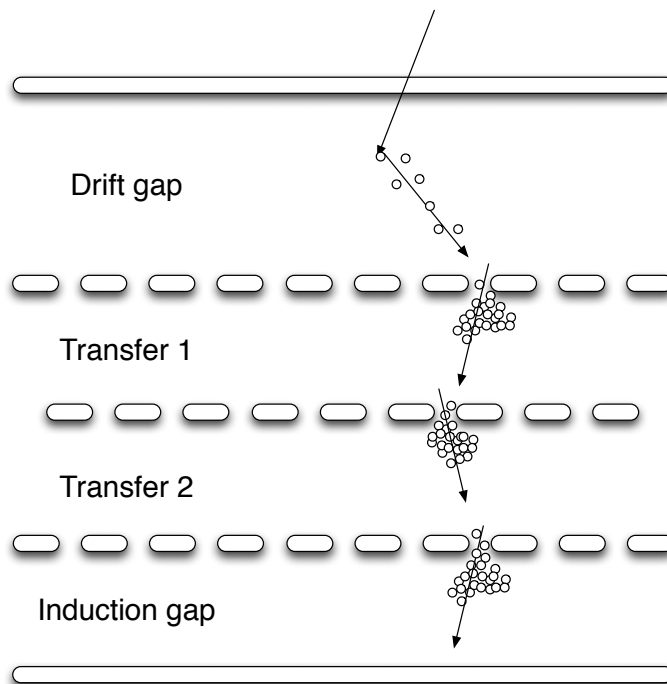


Figure 4.4: GEM schema of the working principle.

Another very interesting feature of GEMs, that makes this detector radically different from RPCs, regards the fact that in GEMs the conversion occurs in the drift area,

the multiplication around the holes of each foil and the detection at the very end in the induction area as in Fig. 4.4 while for the RPC there is only one volume of gas where the multiplication and detection take place

All the GEM foils were and are developed/produced at the CERN Surface Treatment Service. Two of the current LHC experiments, TOTEM(45) and LHCb(46), use triple-GEM detectors both in the forward regions where high rate capability is imperative. The spatial resolution was, since the beginning, one of the most interesting GEM performance; depending on the adopted electronics a space resolution of $\approx 50\mu\text{m}$ is easily achievable while a time resolution of few ns makes GEM slower than RPCs but still acceptable. In this thesis several timing studies were carried out to understand margin of developments to challenge the faster RPCs.

4.2.2 Double and single-mask technology

Up to few years ago the GEM foils were produced with a technology called “double-mask” while recently a process called “Single Mask” has been introduced, in this thesis we have demonstrated that this new process behaves excellently even for large size, which cannot be achieved with the old process. The full-size(47) prototypes GE11.I and GE11.II (as described in 4.6.1 and 4.6.2) that we have build represent the state-of-the-art of this technology with the world’s record in size. In the standard process the photolithography is used to pattern the foil; this is performed transferring by UV-light a mask to the foils, laminated with a photoresistive material. After UV-exposure the foil is chemically etched to remove the copper only in the holes because the photoresist still is protecting the surface. The last step is the etching of the inner insulate layer, again this is performed chemically only for the holes, being the copper already removed. This process is then repeated to both sides of the foil, and it works well for dimensions that do not exceed 0.5m. Anyway a very good alignment is therefore mandatory since the hole size is $\approx 50\mu\text{m}$. To overcome this issue it has been introduced the “Single Mask” technique which makes use of only one film on one side to pattern the foil. In this way the alignment problem between masks disappears and also bigger size foils can be produced. The new “single-mask” process is very similar to the old one, just the bottom copper side is etched after the inner polyimide layer. The polyimide etching then became responsible of a good pattern. In this job utmost important is the shape of the holes which should not be cylindric but as a double cone. This is obtained using

4. BEYOND RPC, GAS ELECTRON MULTIPLIERS DETECTOR

a basic aqueous solution containing ethylene diamine and potassium hydroxide (KOH): the first etches strongly anisotropically while the second isotropically. The process has to be carefully under control, in order to find optimal parameter to achieve the best result and to make it reproducible.

4.3 Candidate Technology

We have proposed GEM technology as a candidate for the upgrade of the muon system. Since 2009 together with the CERN group and the RD51¹ collaboration we have been working on a feasibility study on the use of micro-pattern gas detectors (MPGD). A full-size working chamber with dimensions 990mm \times (220 – 455)mm, has been successfully built and tested as explained in detail in 4.6.1 while a second detector with enhanced performance has been designed and tested as well as detailed in 4.6.2. Fig. 4.5 shows the first version of the candidate prototype, the so-called GE11.I.

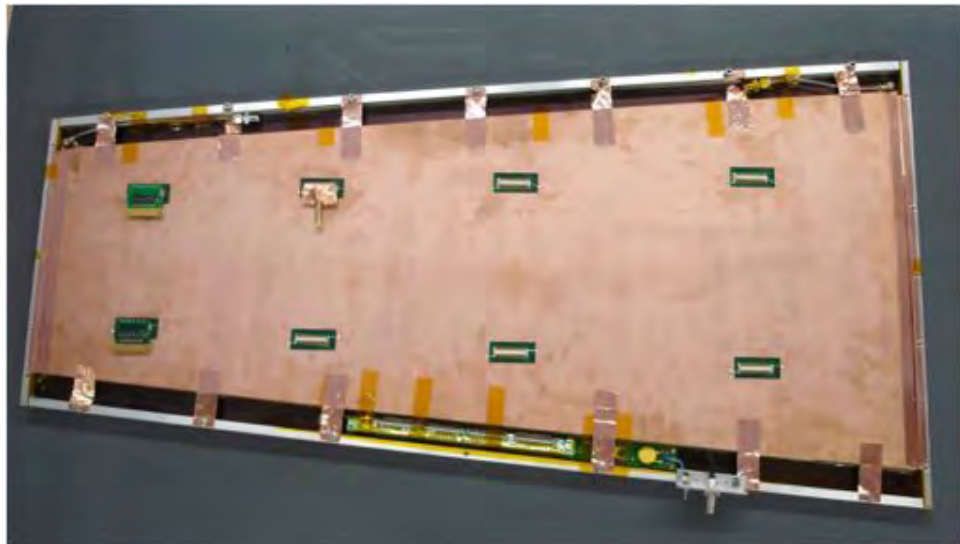


Figure 4.5: GE11 prototype chamber, dimensions: 990mm \times (220 – 455)mm.

We started designing the first chamber prototype at the end of 2009 following a very tight schedule that allowed to complete the construction of the first detector in October 2010. As a starting point we developed a 3D detailed CATIA(48) model of a full-scale detector, to support the construction of a mock-up and functional prototype. This design was optimized with several studies focused on the mechanical integration (routing of cables, gas system) and detector performance such as gas flow simulations, readout and electronics.

¹The R&D collaboration aims the development of advanced gas-avalanche detector technologies and associated electronic-readout systems, for applications in basic and applied research. The main objective of the R&D programme is to advance technological development and application of Micro-pattern gas detectors.

4.4 CMS high- η environment

The high- η region ($|\eta| > 1.6$) presents hostile conditions, with a particle fluence of several hundreds Hz/cm² for an LHC luminosity¹ of 10^{34} cm⁻²s⁻¹. In Fig. 4.6 is shown the forward region of CMS Experiment which is commonly called Endcap. In the Sect. 2.1 more details are given about both CMS Endcaps and the Barrel.



Figure 4.6: Forward region of the CMS Experiment.

The particle rate might increase up to several kHz/cm² depending on the LHC upgrade scenarios. In addition to this we must also consider the rates of thermal neutrons, low energy photons, and γ 's produced in a hadron collider such as the LHC. Hence there are several stringent requirements for a detector to be installed eventually in the high- η region. This is the reason why the forward muon trigger system is equipped with RPC detectors only at $|\eta| < 1.6$. Moreover a very strong magnetic field of 3T is present in the high- η region, the magnetic field orientation is almost perpendicular to the chamber surface. In the end at the moment CMS is actually lacking robustness at high- η because of missing redundancy, GEMs could meet this weakness and improve the

¹In intersecting storage ring collider luminosity is defined as:

$$L = f n \frac{N_1 N_2}{A} \quad (4.2)$$

where f is the frequency of the machine, n is the number of bunches in one beam in the storage ring, N_i is the number of particles in each bunch and A is the cross section of the beam.

overall muon system. The high- η region is presently vacant and presents an opportunity to be instrumented with a detector technology that could sustain the hard environment and be suitable for operations at the LHC and its future upgrades.

4.5 Small size prototypes

Initially we focused on the production and characterization of small size prototype(49) in order to ensure the feasibility of this study. Several prototypes with an active area of $10 \times 10\text{cm}^2$ were produced in the CERN EN-ICE surface treatment workshop and subsequently tested in the RD51 laboratory of the CERN Detector Technology Group (DT). We performed many tests also using several gas mixture to perform timing and efficiency studies and characterize in a detailed way the detector performance, in particular we have heavily used X-rays and ^{56}Fe / ^{90}Sr sources¹ for gain measurement. The gain is calculated monitoring the current from the readout (I_{output}) according to this formula:

$$I_{output} = \frac{\#_{\gamma} \cdot \#_p \cdot G \cdot e}{\Delta t} \quad (4.3)$$

where G is the gain, e the elementary charge and $\#_{\gamma}$ the numbers of counts due to X-rays tube while $\#_p$ is the number of pairs created by each photon, $\#_p$ is defined by:

$$\#_p = E_{\gamma} \cdot \sum_{i=1}^N \frac{\%_{i_{\text{gas}}}}{w_{i_{\text{gas}}}} \quad (4.4)$$

where $w_{i_{\text{gas}}}$ represents the number of pairs created by the chosen gas and $\%_{i_{\text{gas}}}$ the gas percentage in the mixture. Since the I_{output} is difficult to measure when the rate is low and the counts are difficult to measure with high rate, we could evaluate both and finally the gain G using this equivalence:

$$\frac{\#_{\text{gamma}}^{\text{low,without}}}{\#_{\text{gamma}}^{\text{low,without}}} = \frac{\#_{\text{gamma}}^{\text{high,without}}}{\#_{\text{gamma}}^{\text{high,without}}} \quad (4.5)$$

Timing-GEM prototype The first $10 \times 10\text{cm}^2$ detector we have built was a triple-GEM obtained using the standard double-mask technique for the etching of the GEM foils, as explained in the Sect. 4.2.2. The foils, as usual, were made of $50\mu\text{m}$ thick kapton sheets with $5\mu\text{m}$ copper clads on both sides. The GEMs and cathode drift foils were glued on fiberglass frames and mounted inside a gas-tight box as shown in Fig. 4.7.

¹ ^{90}Sr is a radioactive isotope of strontium, with a half-life of 28.8 years, it undergoes β^- decay with decay energy of 0.546MeV distributed to an electron, an anti-neutrino, and the yttrium isotope ^{90}Y . ^{90}Sr is almost a perfectly pure beta source since the γ s emission from the decay is so weak that it can normally be ignored. ^{56}Fe is the most common isotope of iron; about 91.754% of all iron is under this form.

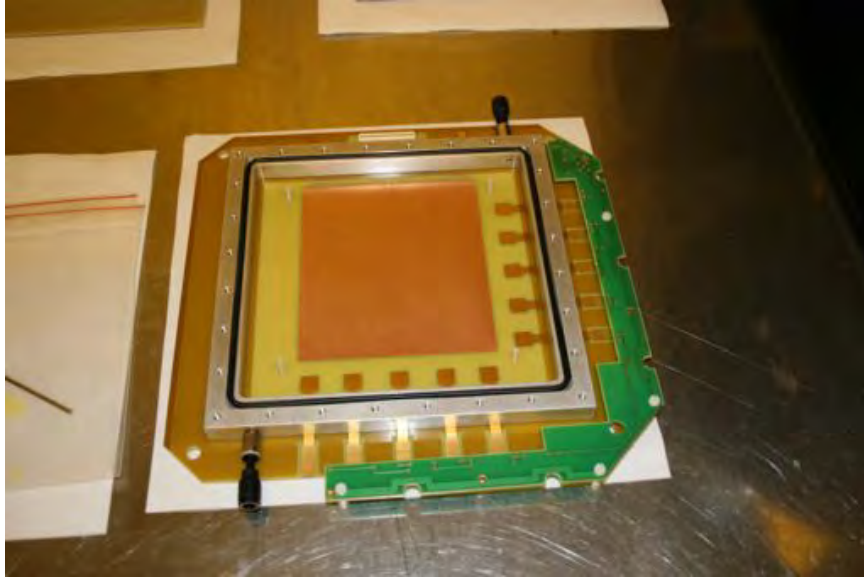


Figure 4.7: Timing-GEM prototype.

The detector has 128 strips with a pitch of 0.8mm and it was called Timing-GEM since we used this detector for several initial timing measurement playing with electrical fields across the gaps and foil voltages as described in Sect. 4.9. Two main different configurations were tried to study the detector performance, each configuration was characterized in terms of different gaps size: drift, transfer 1, transfer 2, induction: respectively 3/2/2/2 mm and 3/1/2/1 mm. The measured gains for this detector is shown in Fig. 4.8 and 4.9 for two different gas mixtures.

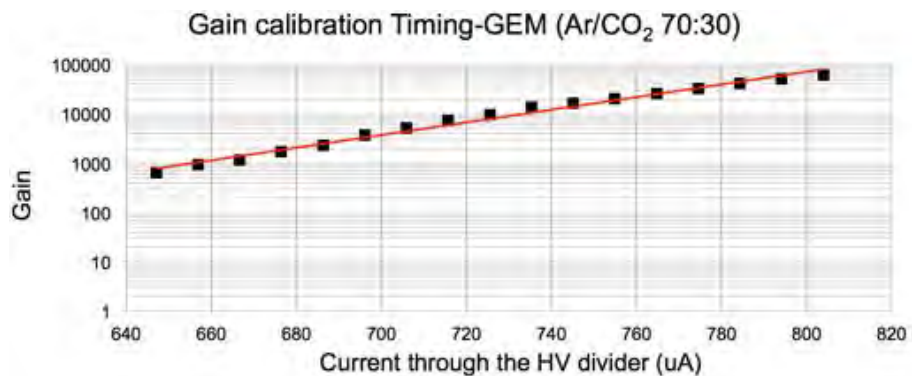


Figure 4.8: Timing-GEM measured gain with gap configuration 3/1/2/1mm and gas mixture Ar/CO₂ 70:30.

4. BEYOND RPC, GAS ELECTRON MULTIPLIERS DETECTOR

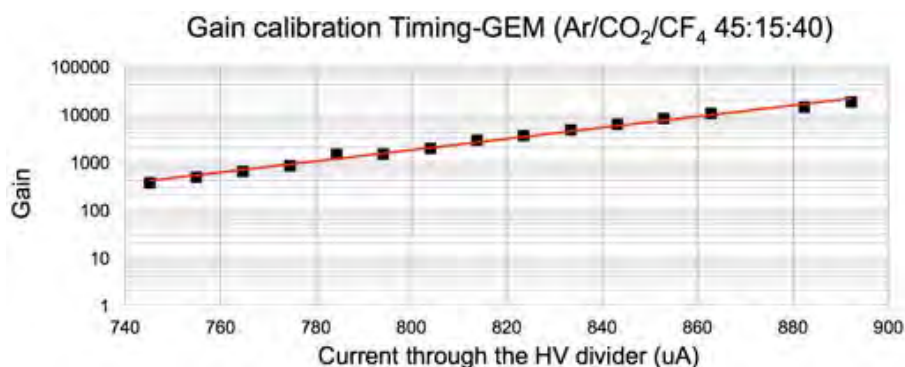


Figure 4.9: Timing-GEM measured gain with gap configuration 3/1/2/1mm and gas mixture Ar/CO₂/CF₄ 45:15:40.

SingleMask-GEM prototype As second detector, we decided to build a geometrically identical chamber using the single-mask technology (introduced in 4.2.2) in order to compare performances between single and double mask technologies. For this second detector we have chosen a 2D readout with 256 channels on X and Y; strips pitch of 0.4mm. The measured gain for this detector is shown in Fig. 4.10 while in Fig. 4.11 a GEM foil cross section is presented to show how the single-mask technique is mature and can achieve a very good bi-conical shape of the holes.

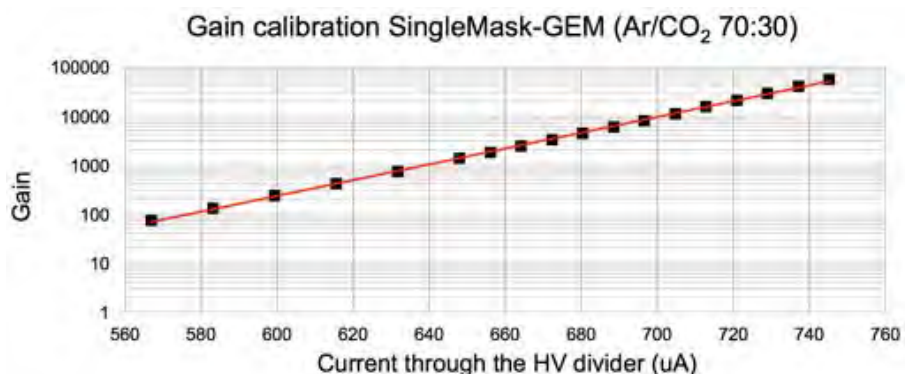


Figure 4.10: SingleMask-GEM measured gain with gap configuration 3/1/2/1mm and gas mixture Ar/CO₂ 70:30.

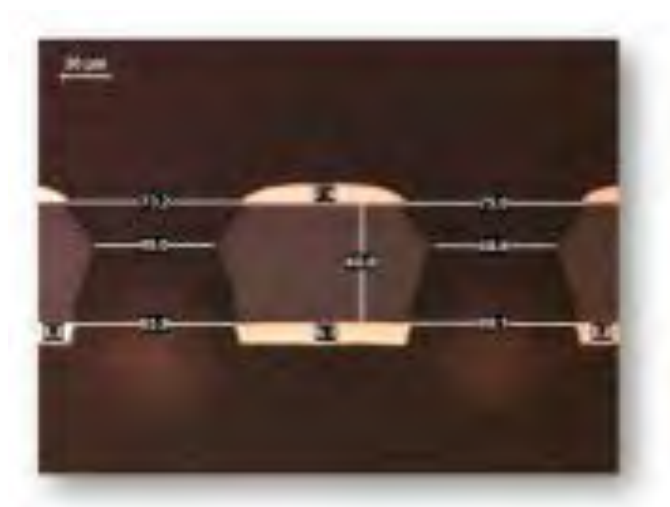


Figure 4.11: single-mask cross section.

Honeycomb GEM prototype Furthermore, another small-size (again $10 \times 10\text{cm}^2$) detector was prepared using existing single-mask foils of the single-mask prototype to prove a candidate solution to avoid the GEM foil stretching, which can be a critical process at certain stages(50). So, to avoid the need for foil stretching during detector assembly, a technique based on inserting honeycomb spacers into the detector gaps was tested as in Fig. 4.12.

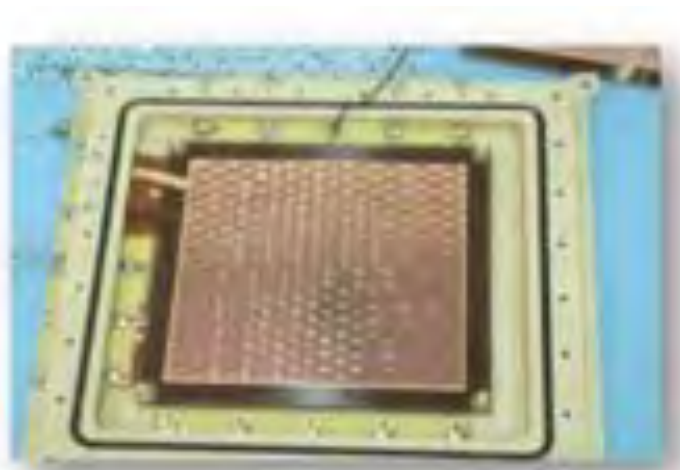


Figure 4.12: GEM with honeycomb structure inserted.

4. BEYOND RPC, GAS ELECTRON MULTIPLIERS DETECTOR

Three different configurations were tried with varying honeycomb cell sizes (in drift, transfer 1, transfer 2, induction gap): 12/12/12/12 mm (config 1), 6/12/12/12 mm (config 2), 6/0/0/0 mm (config 3). Promising results will be shown in the Sect. 4.9 even if a new solution called NS2 will probably take over the honeycomb idea.

NS2 prototype This prototype was the first being produced using a mechanical stretching process instead of the traditional thermal one. The thermal stretching process could be critical at certain stage, even if the principle is simple is difficult to standardize and serialize this process for a mass production; also the cost is an issue since this process keeps busy at least two technician for few days (even a week). The Fig. 4.13 shows the new detector built piling up the foils stretched by means of screws fixed on the external frame.

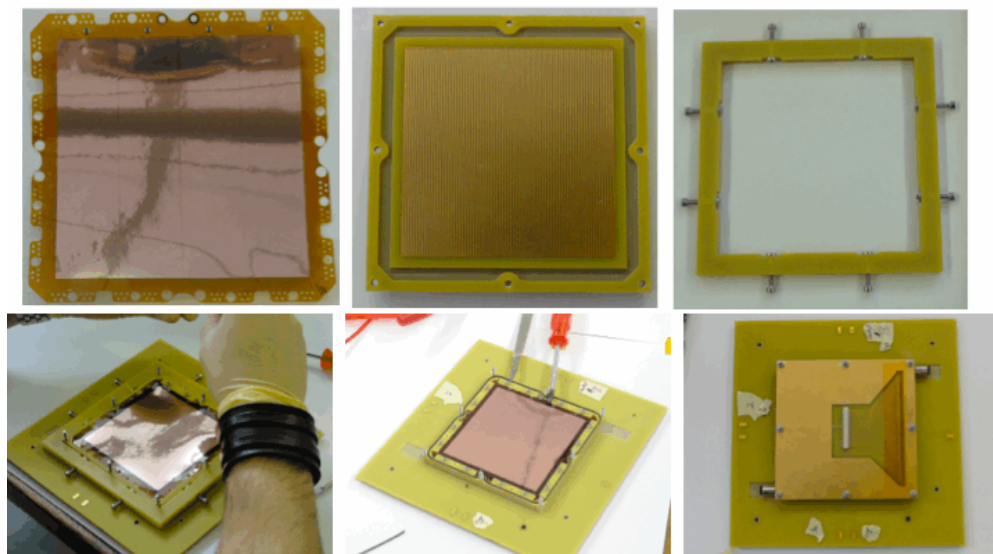


Figure 4.13: Construction phases of the self-stretched chamber.

There are really many advantages such as the fact that no glue is used and the detector could be dismantled anytime (for example to replace a foil) within one hour, the same time you need to mount it, incredibly faster than the usual way to mount

(and stretch) the detectors so far. Another big advantage consists in the fact that the readout also could be changed anytime depending from different usage and applications, moreover in the future electronics upgrade where more and more integration is foreseen the readout will host power regulation and distribution for the front-end chips and the the chips itself in such a way to reduce possibilities of bad contacts, reduce noise, and make faster the detector production and testing. A $10 \times 10\text{cm}^2$ detector has been produced and tests were performed at the RD51 laboratory, the gain curve calibration is shown in Fig. 4.14.

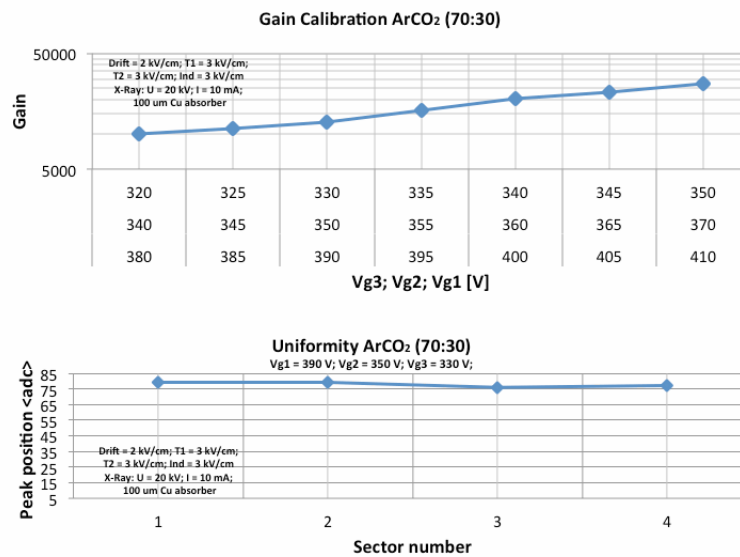


Figure 4.14: Gain curve of self-stretched GEM.

So encouraging results indicated that this idea worked and then we proceed to the next step that was to increase the dimensions. As intermediate detector between the small $10 \times 10\text{cm}^2$ and the full-size we have decided to go for a $30 \times 30\text{cm}^2$ detector to check at least feasibility of this dimension before to go for the full-size chamber. Finally this new idea could make the life easier and reduce (around factor 10) the cost of each detector.

Korean-GEM prototype In the end the Fig. 4.15 shows the latest small size ($7 \times 7\text{cm}^2$) detector which was build in Korea(51) in May 2011.

4. BEYOND RPC, GAS ELECTRON MULTIPLIERS DETECTOR

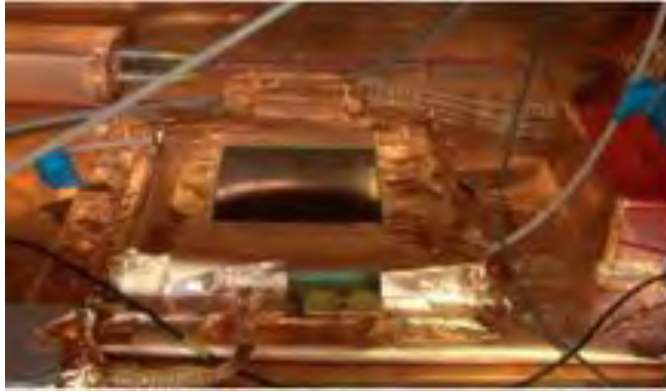


Figure 4.15: Korean GEM inside the X-rays copper box.

This detector represents one of the first attempt outside CERN to build GEMs; the result is excellent as shown in the Fig. 4.16. In the view of the mass production for the GE1/1 project this detector is demonstrating that external companies could afford the GEM foils production, even if for the moment only for a small size detector. The external production is a key point for the costs to be decreased.

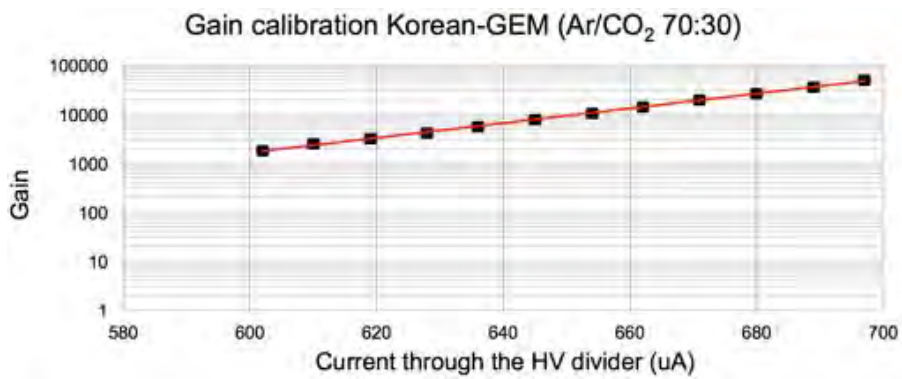


Figure 4.16: Korean-GEM measured gain Ar/CO₂ 70:30.

4.6 Large detector construction

4.6.1 Full-size detector construction - GE11_I (2010)

The exploded CAD view, in Fig. 4.17, shows the mechanics, derived from the originally planned RPC detector RE1/1 and adopted for the GE1/1 project. The proposed "GEM Endcap Station 1 Ring 1" or "GE1/1" detector is designed to fit exactly into the envelope of the older RPC detector.

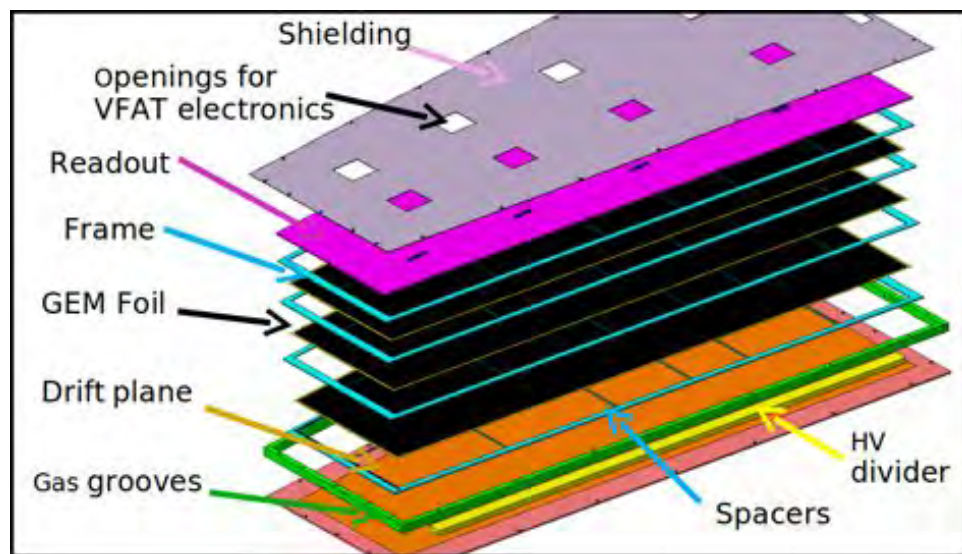


Figure 4.17: GE1/1 exploded CAD view.

With respect to the old detector layout, few modifications were done to accommodate the new electronics and the new gas system. Several gas flow simulations(52) have been performed focusing on geometrical optimization of the velocity field inside the chamber volume. Different configurations were tested in terms of number of inlets and outlets and spacers geometry. For each data-set we estimated the percentage of the chamber where the flow was below a threshold. The final design was chosen using the feedback from the simulations.

The triple-GEM detector (in Fig. 4.17 black) is fully contained inside an aluminum box and uses large-area single-mask GEMs(44). As discussed in 4.2.2 the production of GEM foils relies on the photolithographic processes; after one can choose between single and double-mask technology. Anyway once the foil dimension exceeds 40cm the double-mask process becomes critical, so we have chosen the single-mask technology

4. BEYOND RPC, GAS ELECTRON MULTIPLIERS DETECTOR

still not widely used for really large size detector. The single-mask foils produced are made of $50\mu\text{m}$ thick kapton sheet with $5\mu\text{m}$ copper clad on both sides.

Between each GEM foil there is a 2mm glued spacer (in Fig. 4.17 blue); on the right the HV divider is placed (in Fig. 4.17 yellow) which provides voltage to different sectors of each foil. The gas mixture enters from the short side via grooves cut (in Fig. 4.17 green) in the aluminum frame. The adopted electronics, the TOTEM VFAT(53), is installed in the openings (in Fig. 4.17 violet) that allow connections between the VFAT chips and the readout plane (in Fig. 4.17 pink).

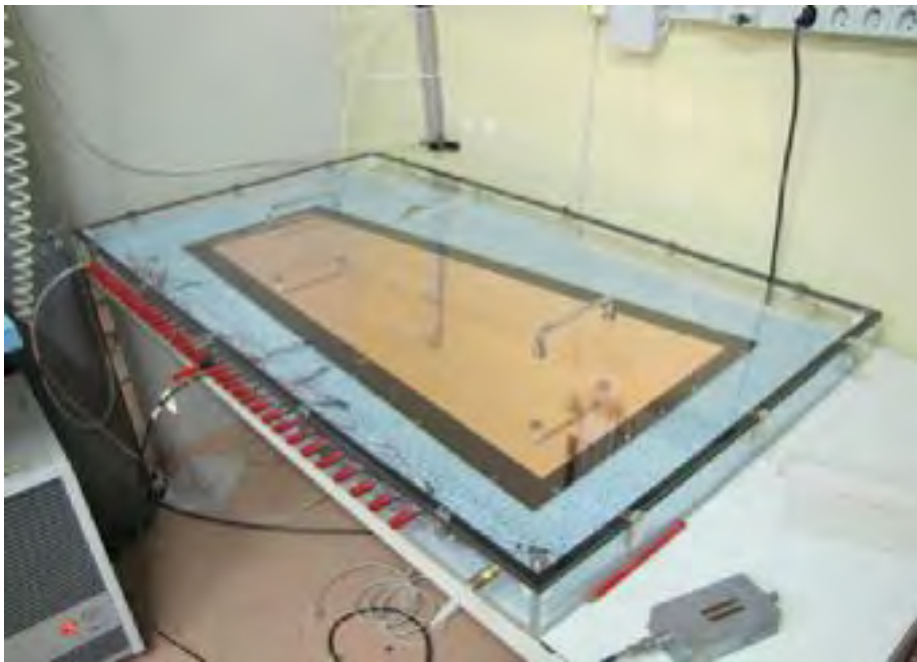


Figure 4.18: GE1/1 Drift plane under HV test in gas box.

The drift electrode (Fig. 4.18), which is part of the chamber envelope itself, is produced by gluing a $300\mu\text{m}$ kapton layer with $5\mu\text{m}$ copper cladding to a 3mm aluminum plate. The drift electrode was tested in open air and nitrogen and showed a leakage current less than 20nA.



Figure 4.19: GE1/1 First full-size foil produced.

Fig. 4.19 shows our first full-size trapezoidal GEM foil with these dimensions: $990\text{mm} \times (220 - 455)\text{mm}$. In Fig. 4.20 the sketch of the chosen sectorization of the foil is presented. Each sector, out of the 35, covers 100cm^2 so that the discharge probability (measured at the RD51 laboratory) is about 10^{-6} for a gain of $2 \cdot 10^4$.

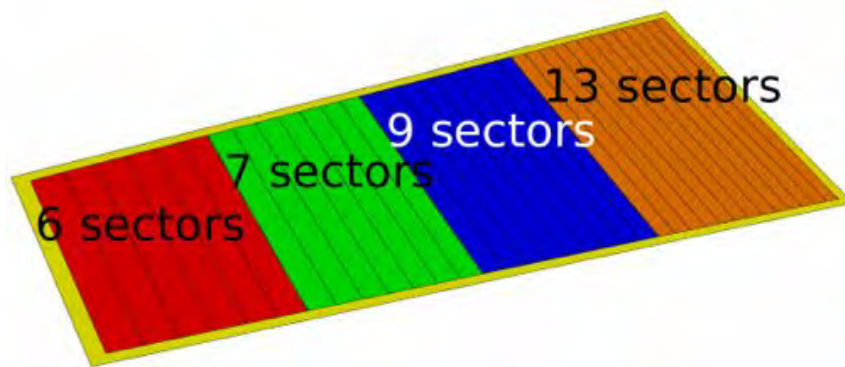


Figure 4.20: GE1/1 High Voltage sectors.

Before installing the foils inside the detector, they were subjected to thermal stretching using a special oven. The temperature was maintained at 37°C for 24 hours. After the stretching process is completed, the foil is ready to be glued together with the frame

4. BEYOND RPC, GAS ELECTRON MULTIPLIERS DETECTOR

(Fig. 4.21). Finally, the foil plus the frame are again placed inside the oven to cure the glue.



Figure 4.21: GE1/1 Gluing spacers on the foil with the glue gun.

While the frame is necessary to keep the foils in place, we performed studies with the purpose of avoiding the stretching process and using any frame at all to have a bigger active area. During a test beam campaigns in 2010 we have tried using a honeycomb structure in between the foils which is supposed to behave as a frame to maintain the proper distance between foils; it was proved that this small-size prototype (described in Sect.4.5) containing this honeycomb worked without problems albeit with a reduced efficiency due to the geometrical influence of the honeycomb walls. Further studies are going on to increase the honeycomb cell size to reduce the efficiency loss to a low reasonable value. Another strategy to avoid the GEM spacer frames could be to tension the GEM foil sufficiently by adopting the well tested stretching technique used at Frascati; there the stretching process is performed mechanically with accurate control of the applied force(54). For the GE1/1 prototype, every foil is tested before and after the stretching process; we perform a careful optical inspection and a sector-by-sector HV test increasing the voltage up to 500V measuring the current, which we expect to be of the order of few nA. This optical inspection is extremely important because simple dust could dramatically affect chamber operations. Because of this, we always operate in a clean room.

The readout PCB (Fig. 4.22) is divided into four η partitions and each partition has two VFAT chips. Each VFAT chip is able to read 128 channels, so for every sector

we have 256 channels. The strip pitch is varying along the longest chamber dimension from 0.8 mm to 1.6mm. Several noise studies have been done with the same electronics used at the test beam with small size detectors for understanding and debugging the detector. The low noise level we achieved made it possible to operate the full-size prototype with approximately the same threshold, and therefore operating conditions, used for the small prototype.



Figure 4.22: GE1/1 PCB readout plane.

Fig. 4.23 shows the layout of the HV divider board which provides different voltages to the GEM foils. It is made using HV SMD resistors and has a built-in RC Filter which cuts the intermediate frequency from the CAEN 1527 power supply, as GEM detectors are sensitive to HV power supply fluctuations.

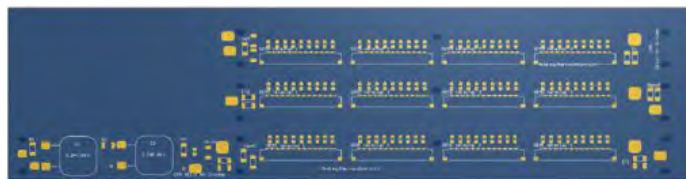


Figure 4.23: GE1/1 HV divider.

For the readout electronics we adopted the VFAT(TOTEM) chip because of its capabilities of tracking and fast triggering(55), which make it very suitable for our application. The VFAT is a digital on/off chip for tracking and triggering with an adjustable threshold for each of the 128 channels; it uses $0.25\mu\text{m}$ CMOS technology

4. BEYOND RPC, GAS ELECTRON MULTIPLIERS DETECTOR

and its trigger function provides programmable fastOR information based on the region of the sensor hit. For prototype testing we used the front-end electronics developed by INFN (Siena and Pisa), based on the TOTEM VFAT chip.

4.6.2 Full-size detector Construction - GE11_II (2011)

The construction of the second prototype started mid-April 2011. The goal of this detector was to address the inputs coming from the physics community about the detector granularity and timing performance. About this last point the strict CMS requirement pushed us to choose a fast gas mixture containing CF_4 and a reduced gas gap configuration. Timing properties of gas containing CF_4 are illustrated in Sect.4.9 which shows excellent results with small prototypes during the 2010 test beam campaigns. This new prototype, called GE11_II, shared the same mechanics and electronics of the old GE11_I since the new detector represented an upgrade in terms of timing performance and readout electronics.

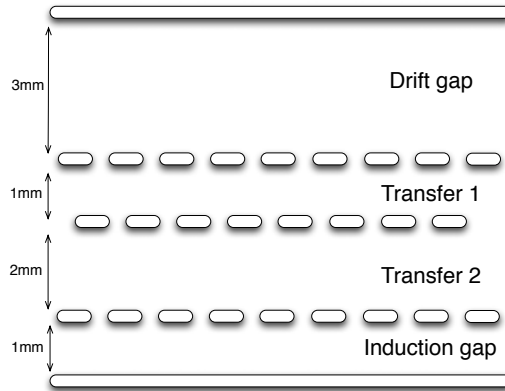


Figure 4.24: Gap configuration for the full size prototype GE11_II.

The chosen gap configuration, for this second prototype, was 3/1/2/1 (Fig. 4.24), in particular this new layout was challenging from the mechanical point of view since the stretching process should be really excellently performed being the gaps so subtle. For small detectors this configuration was already used but for large size foils we had to tune the thermal stretching and think about a new stretching stage performed via mechanical forces which is discussed in 4.5. Modifying the oven temperature from 37°C to 30°C and monitoring carefully all the operations we manage to stretch properly all the foils and

build the detector. For what regards the readout as we wanted to address comments from the physics community we decided to improve a lot the granularity equipping the readout with 3184 channels (previously the first detector had 1024 channels). Now in the readout plane we designed 8 η -partitions and 3 sectors for partition in order to have 24 slots for the electronics. The designed strip pitch was smaller compared to the first prototype (from 0.8mm to 1.6mm) namely from 0.6mm to 1.2mm following the same usual trapezoidal shape. The Fig. 4.25 shows the gain calibration curve of the GE11_II performed just before the data-taking at the beam experimental area.

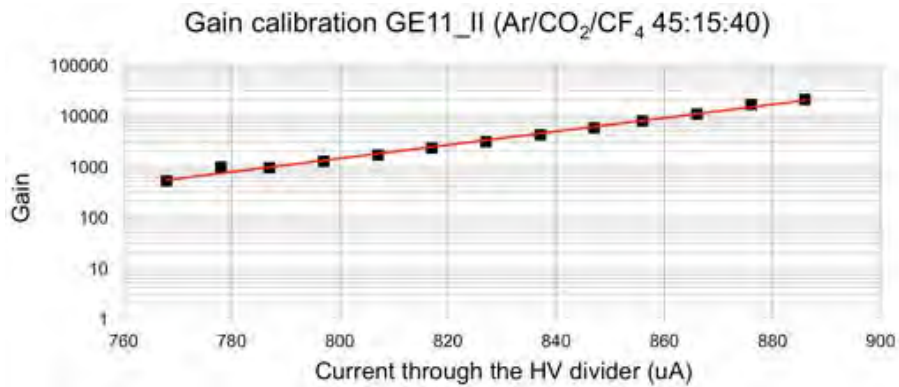


Figure 4.25: GE11_II measured gain Ar/CO₂/CF₄ 45:15:40.

4.7 The beam test experimental setup

A test beam is a precious period where an equipment, mainly a detector for HEP, can be tested in a similar environment with respect to the one present in big experiment such as CMS. At CERN there are several beam lines with different features and performances, in fact there are several campaigns performed by a large world wide community which every year exploits the high potential of all kind of beams provided by the accelerator complex (briefly described in Sect.1.2). In 2010 we run 3 beam tests (June, August and October) at the SPS-H4 experimental area, in the first and second we worked with small size prototype, while in the last test-beam period the prototype CMS GE11_I chamber was tested. In 2011 we had 4 test beams (June, August, September and October) at SPS-H2, SPS-H4 and SPS-H8. In general we used a 150GeV muon and pion beam with a rate of few kHz.

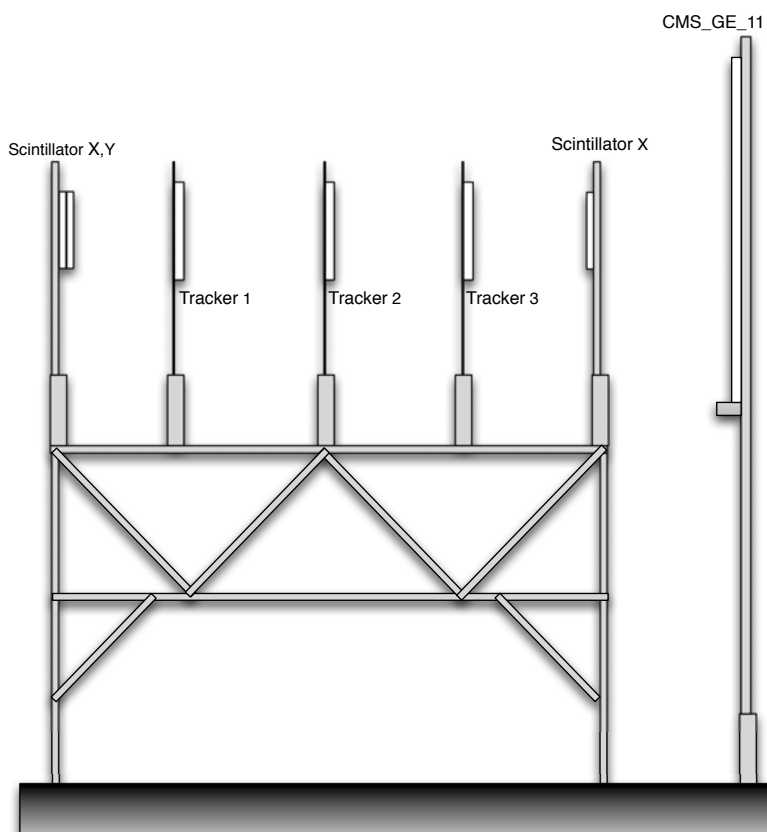


Figure 4.26: RD51 triple-GEM based Tracking telescope.

4.7 The beam test experimental setup

The small prototype were usually installed into a GEM telescope (Fig. 4.26) which consists of three standard $10 \times 10\text{cm}^2$ triple-GEM detectors (GEM-Tracker). In the telescope all triple-GEM detectors ($10 \times 10\text{cm}^2$ active area) run with a gas mixture Ar/CO₂ (70:30) and at a gain $\approx 10^4$. Each GEM-Tracker detector has 256 strips (0.4mm pitch) in both horizontal and vertical coordinate, perpendicular to the beam. For the GEM-Tracker in total 12 VFAT chips were used, four for each chamber, two out of four were used for the vertical readout, while the remaining two for the horizontal one. The VFAT(53) ASIC was designed at CERN using radiation tolerant technology. It has a 128 channel analog front-end and produces binary output for each of the channels for tracking. In addition, it can provide a programmable, fast OR function on the input channels depending on the region of the sensor for triggering. The chip offers adjustable thresholds, gain and signal polarity, plus a programmable integration time of the analog input signals. The signal sampling of the VFAT chip is driven by a 40MHz internal clock. The readout of all detectors was done with the TURBO boards developed for TOTEM(45) by INFN Siena-Pisa. Concerning the software development a lot of work has been done about the reconstruction algorithm to calculate event by event precisely ($100\mu\text{m}$) the tracks in order to evaluate efficiency, cluster size and space resolution of the chamber under test (small or/and full-size prototype) as detailed in the Sect. 4.8.

The final environment at CMS will be dominated by a 3T^1 almost parallel² magnetic field. In Fig. 4.27 and Fig. 4.28 magnetic field calculations are shown according to simulations.

¹This field is around 200.000 times stronger than natural Earth field!

²Detector and Magnetic field form an angle of 8°C .

4. BEYOND RPC, GAS ELECTRON MULTIPLIERS DETECTOR

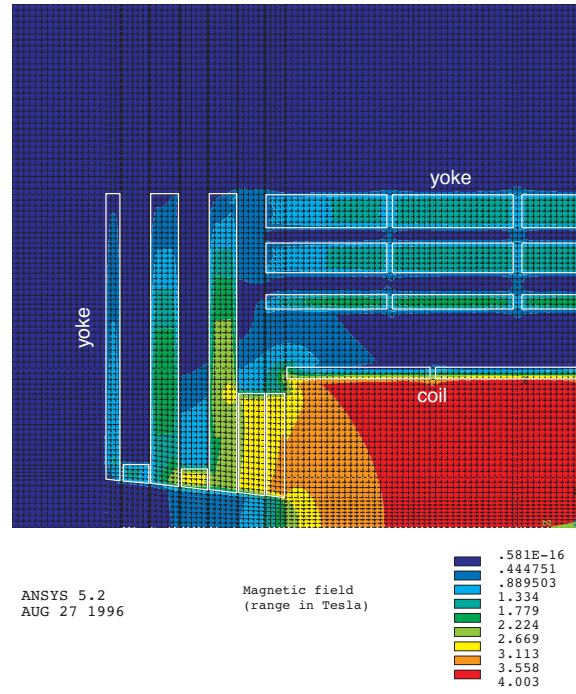


Figure 4.27: Total Magnetic field of CMS Endcap.

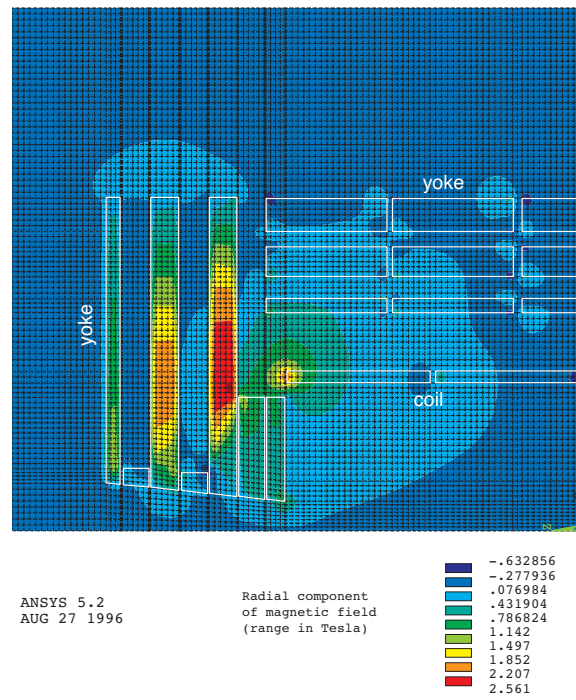


Figure 4.28: Radial component of the CMS Endcap Magnetic field.

4.7 The beam test experimental setup

Then to reproduce this hard and delicate environment we have decided to test our full-size chamber in the same magnetic field using the CMS magnet M1 actually installed in Preveessin at the SPS-H2 beam line (Fig. 4.29) during June and July 2011. The RD51 collaboration was strongly supporting us also providing the GEM-Tracker which was mounted far away from the magnet to reconstruct tracks event by event. The data-taking was intense due to several hardware failures and magnet issue but in the end we manage to complete our tentative data-taking plan which was very ambitious.



Figure 4.29: CMS M1 magnet at the SPS-H2 beam line (Preveessin).

4.8 Software Development

The developed software is actually a complete framework which is able to read the raw data coming from the DAQ and produce plots and 3D view of events. The DAQ and part of the Event-builder and Reco routines have been previously developed¹ in 2009. The framework is shown in Fig. 4.30 and actually it is a suite of script and different software working together in a coherent way.

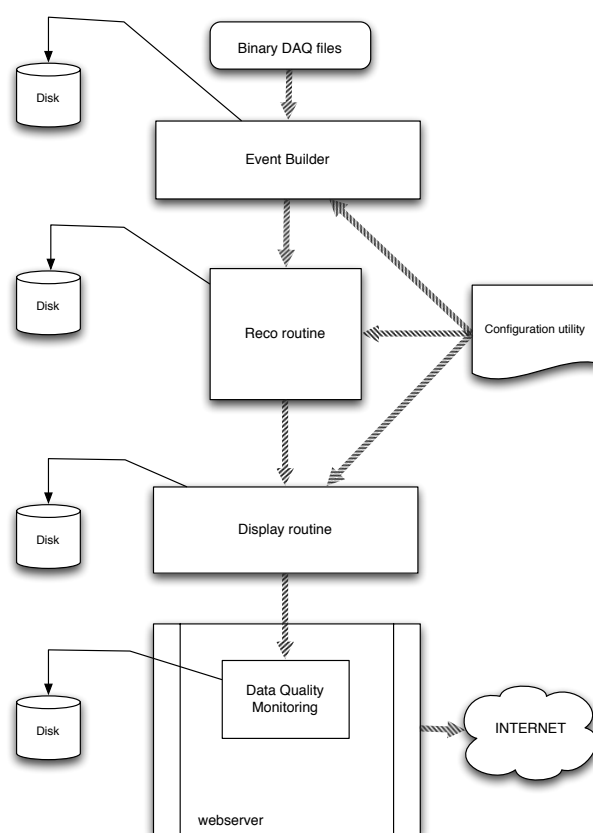


Figure 4.30: Software Development for Data analysis and quality monitoring.

On top of everything the DAQ written in Labview produces binary files with structured data, the Event-builder reads and transforms the binary information into a ROOT Tree². The Tree is then processed by the Reco routines where the main embodiment

¹Many thanks to Eraldo Olivieri, Matteo Alfonsi and Gabriele Croci for their help and time spent together!

²A Tree is a ROOT object and consists of a list of independent branches (ROOT TBranch object).

is the efficiency measurement performed by means of 2D fitting of tracker data. In the end the Display routine is able to read and interpret graphically the data coming from the Reco routines; the user can watch in a 3D environmental space the data-taking event by event as in Fig. 4.31.

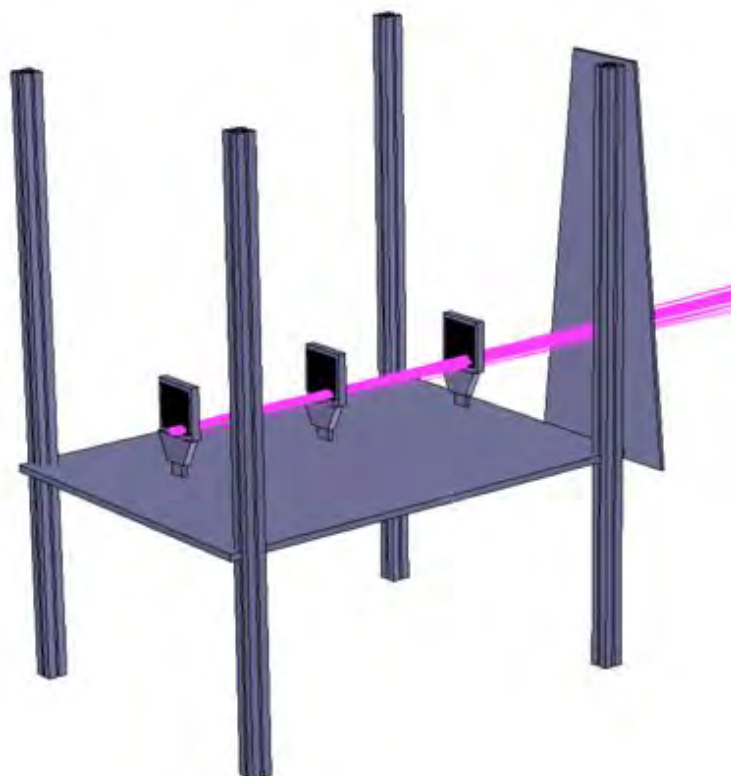


Figure 4.31: 3D Event Display, view of the tracking GEM table and GE1/1 prototype detector.

Moreover an other useful developed tool is the online Data Quality Monitoring (DQM) as shown in Fig. 4.32. The DQM consists in a webserver which shows online preliminary results from the data-taking. Each run, in fact, once is closed is soon processed and a script is invoked dynamically, updating the main webpage. The webserver shows a minimal menu with the run number list, updated dynamically, and with main plots such as occupancy, efficiency, strip profile and cluster size. This tool is very useful

Each branch has its own definition and list of buffers. Branch buffers are automatically compressed and they may be automatically written to disk or kept in memory. Variables of one branch are written to the same buffer.

4. BEYOND RPC, GAS ELECTRON MULTIPLIERS DETECTOR

during intense data-taking period because it allows operators to quickly check the data quality.

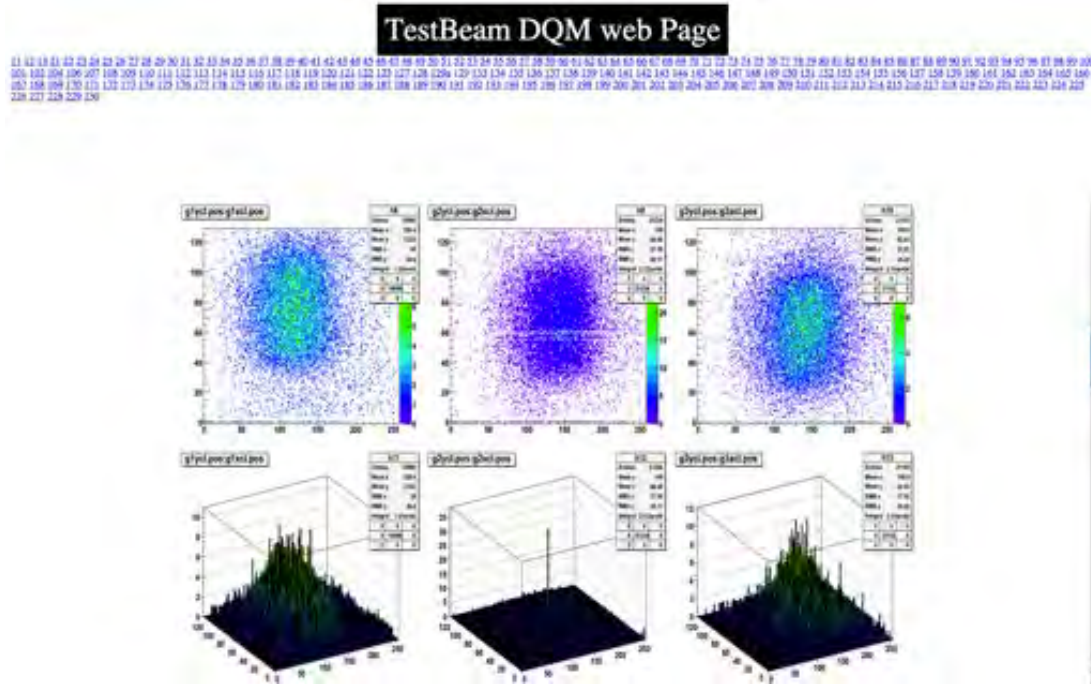


Figure 4.32: Data Quality Monitoring for the Test Beam.

4.9 Data analysis and performance

The performance of small prototypes(49) has been evaluated during the test-beams that took place mainly in the year 2010 even if further gas studies were performed also in 2011. The time resolution achieved is around 4.5ns as in Fig. 4.33, with gas mixture Ar/CO₂/CF₄ (45 : 15 : 40). The triple-GEM foils of the detector used in this test were powered individually without any HV divider, thanks to this technique we were able to set fields and voltages between the foils testing several configurations.

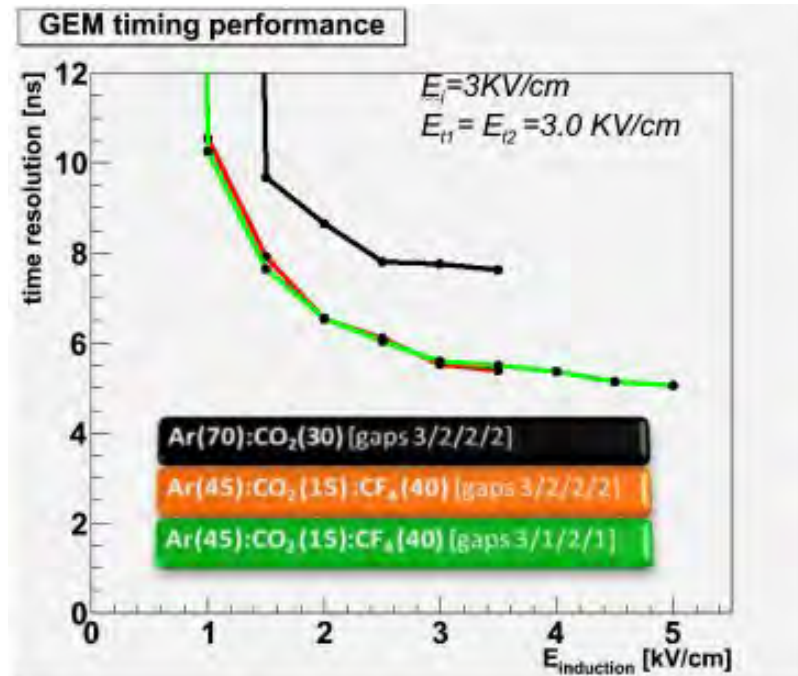


Figure 4.33: Time resolution of the double mask GEM small prototypes.

Time resolution values have been calculated performing some statistical data-analysis in order to remove other effects which in the beginning were masking the real physical value. In fact the time distribution measured with the TDC¹ is affected by a jitter in time due to the fact the the VFAT is a digital chip with internal clock (40MHz). Since the beam is not synchronous than the chip is introducing a dead time between the chip internal clock and the signal arrival. The result is that the TDC spectrum is

¹In the experimental beam area we have used a CAEN VME V1290A with 32 independent Multi Hit/Multi Event Time to Digital Conversion channels. The unit houses four High Performance TDC chips, developed by CERN, which provides 25ps resolution in time.

4. BEYOND RPC, GAS ELECTRON MULTIPLIERS DETECTOR

a convolution between the original gaussian time distribution and a jitter distribution introduced by the chip as in Fig. 4.34.

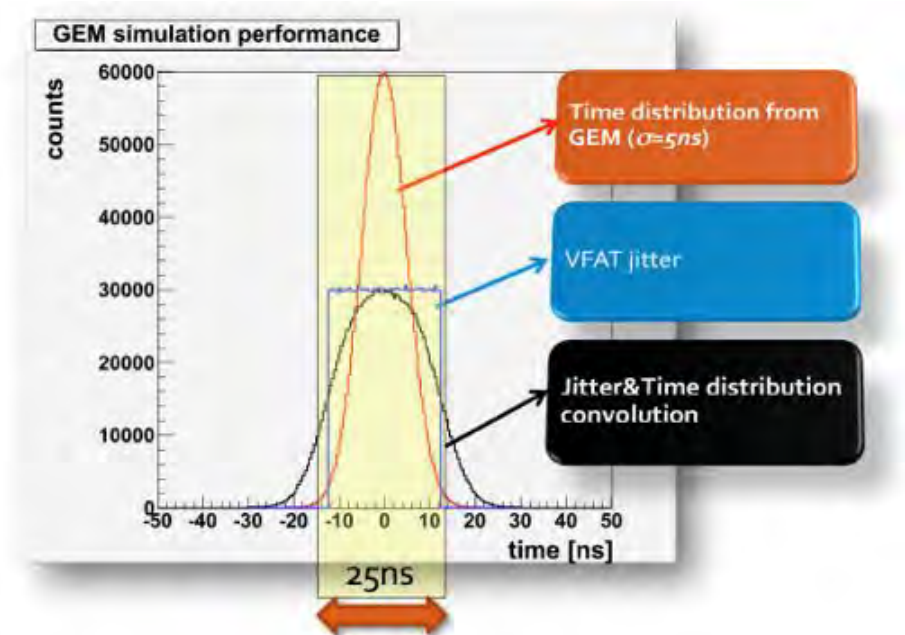


Figure 4.34: Convolution between gaussian time distribution coming from the detector and jitter due to asynchronous beam.

To retrieve the original gaussian shape we must retrieve the time distribution $f(x)$ from $h(x)$ where $g(x - \tau)$ represents the time jitter.

$$h(x) = \int_a^b f(x) * g(x - \tau) dx = \int_a^b \frac{1}{\sqrt{2\pi\sigma^2}} e^{-\frac{(\tau-\mu)^2}{2\sigma^2}} a \text{rect}(x/b) d\tau. \quad (4.6)$$

where:

$$f(x) = \frac{1}{\sqrt{2\pi\sigma^2}} e^{-\frac{(\tau-\mu)^2}{2\sigma^2}}, \quad g(x) = a \text{rect}(x/b) \quad (4.7)$$

Then to retrieve $f(x)$, numerically a small montecarlo algorithm has been designed to correlate the original gaussian shape with the convoluted experimental data.

In Fig. 4.35 we evaluated the efficiency of the prototype built with single-mask technology foil and the efficiency of the standard double-mask.

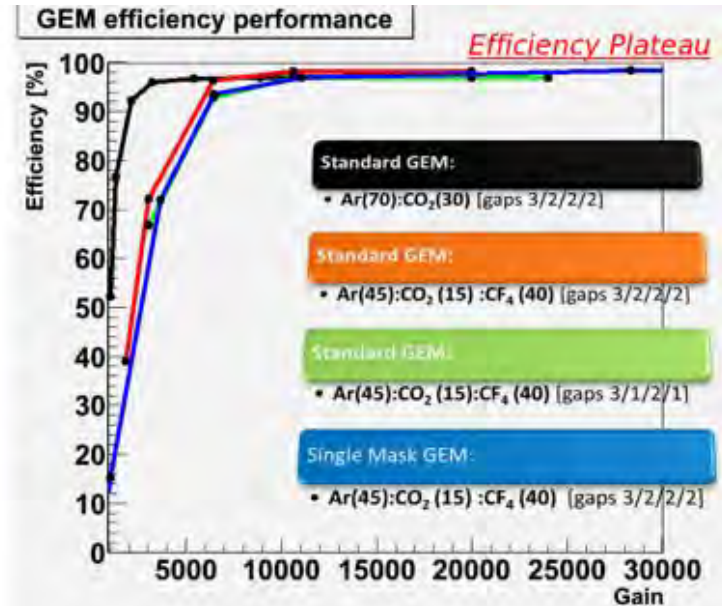


Figure 4.35: Efficiency comparison: single and double mask technology.

The single-mask prototype performs in the same manner as the double-mask prototype. This result allows us to replace the standard double-mask technology with the single-mask, which is the only technology that can be suitable for big size GEM foils.

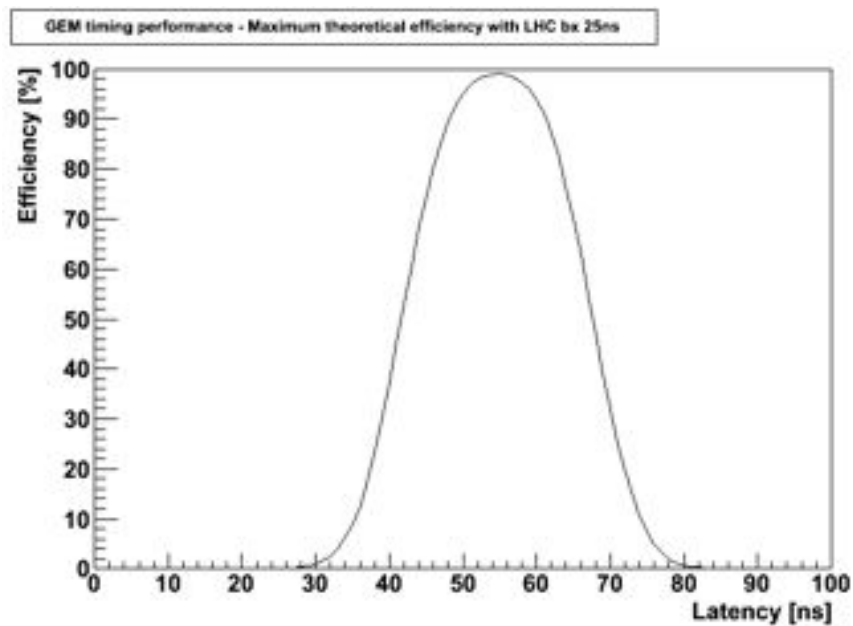


Figure 4.36: Simulated efficiency with LHC bunch crossing (bx) 25ns.

4. BEYOND RPC, GAS ELECTRON MULTIPLIERS DETECTOR

Using the best time resolution obtained experimentally (after the de-convolution), we have simulated the efficiency for the LHC bunch-crossing of 25ns. Fig. 4.36 shows the resulting efficiency vs. latency, which is an adjustable parameter of the VFAT chip. For what concerns the small prototype detector which contains the honeycomb structure inside GEM foil gaps; Fig. 4.37 shows a muon-graphy where it is clear the identification of various zones and sharp honeycomb walls. The honeycomb cells define the amount of inefficient areas since through the walls and nearby the amplification is disturbed and gain drops dramatically. Anyway the detector is able to work without additional problems like sparks; low efficiency ($\approx 70\%$) is fully justified by the geometrical factor of the honeycomb cell size.

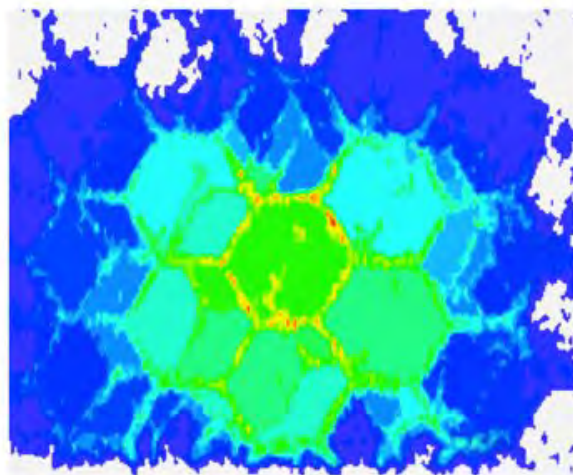


Figure 4.37: Honeycomb GEM - Muography at the beam test.

In October 2010 we completed the first test beam (pion and muon beam 150GeV) using the full-size prototype candidate chamber GE11_I described in the Sect. 4.6.1. From an operational point of view, the full-size prototype behaved excellently. Fig. 4.38 shows the prototype detector mounted on a movable table for a dedicated beam scan along the chamber.

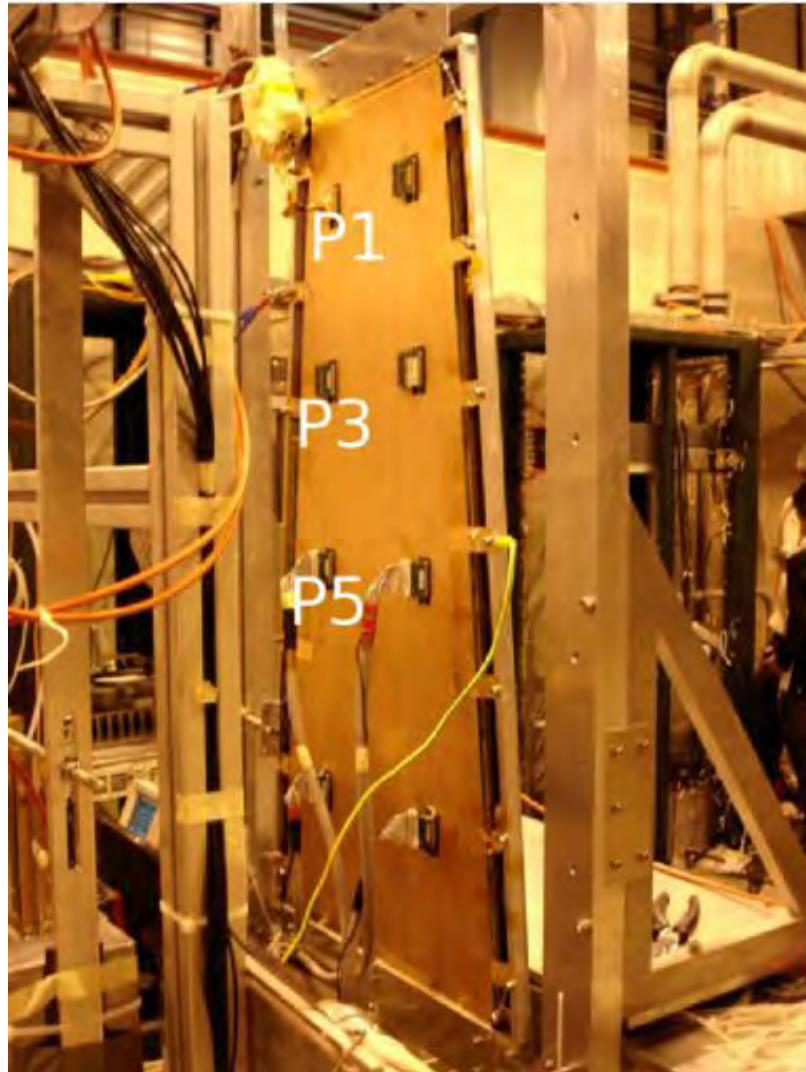


Figure 4.38: GE11.I Installed at the RD51 H4 experimental beam area showing P1-P3-P5 the sectors fired from the beam line.

During the beam period we were able to test the full-size detector along with the RD51 GEM-Tracker telescope to reconstruct tracks. In Fig. 4.39, 4.40 and 4.41 the efficiency measurement is shown indicating that the detectors behaves excellently in all the sectors.

4. BEYOND RPC, GAS ELECTRON MULTIPLIERS DETECTOR

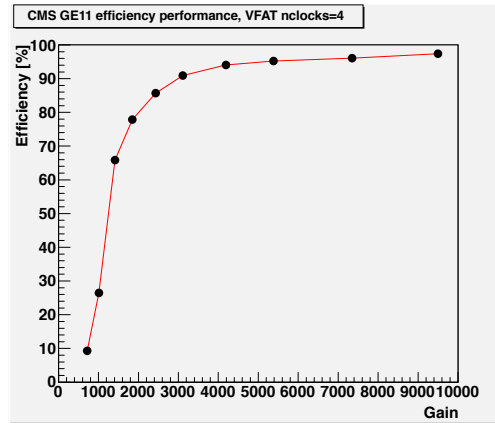


Figure 4.39: Efficiency scan of the GE11.I: P1.

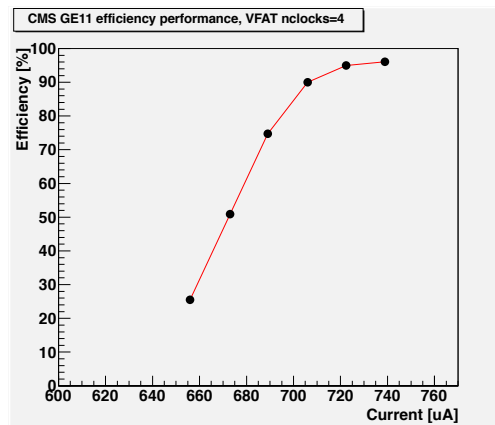


Figure 4.40: Efficiency scan of the GE11.I: P3.

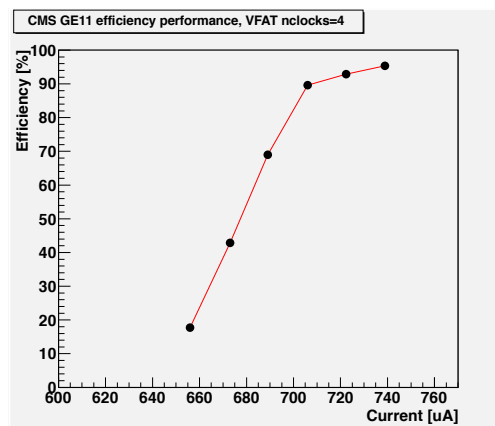


Figure 4.41: Efficiency scan of the GE11.I: P5.

Moreover the space resolution has been measured and shown in Fig. 4.42, 4.43, and 4.44.

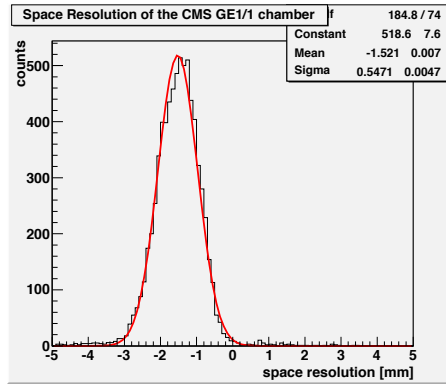


Figure 4.42: Space resolution of the GE11.I: P1.

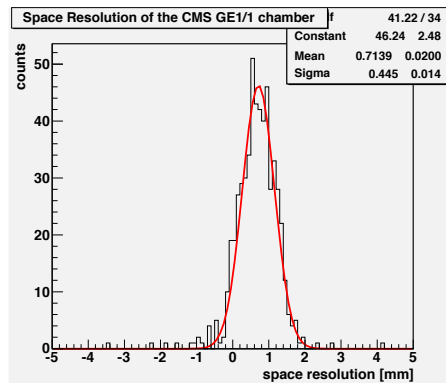


Figure 4.43: Space resolution of the GE11.I: P3.

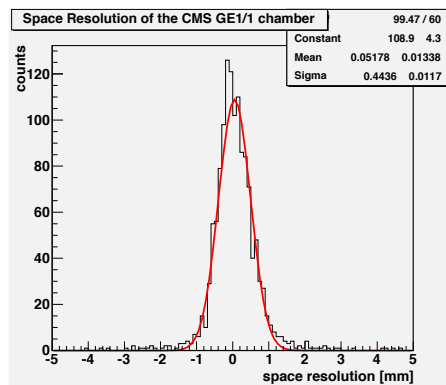


Figure 4.44: Space resolution of the GE11.I: P5.

4. BEYOND RPC, GAS ELECTRON MULTIPLIERS DETECTOR

During June and July 2011 we have deeply started studying the performance of the GE11_II described in the Sect. 4.6.2. This full-scale detector was tested with a 150 GeV muon/pion beam at the CERN SPS H4, H6 and H8 beam lines during several RD51 test beam campaigns. The RD51 standard double-mask triple-GEM beam telescope has been used as usual as tracking device. In the full-size detector, based on the observed very low noise without beam, a VFAT threshold of 12 units¹ was set along with a comparator current set to $40\mu\text{A}$. With these settings the noise was practically absent, operating the detector in a gain range of $0 - 10^4$. The Fig. 4.45 shows a preliminary HV and latency scan with Ar/CO₂/CF₄ (45:15:40).

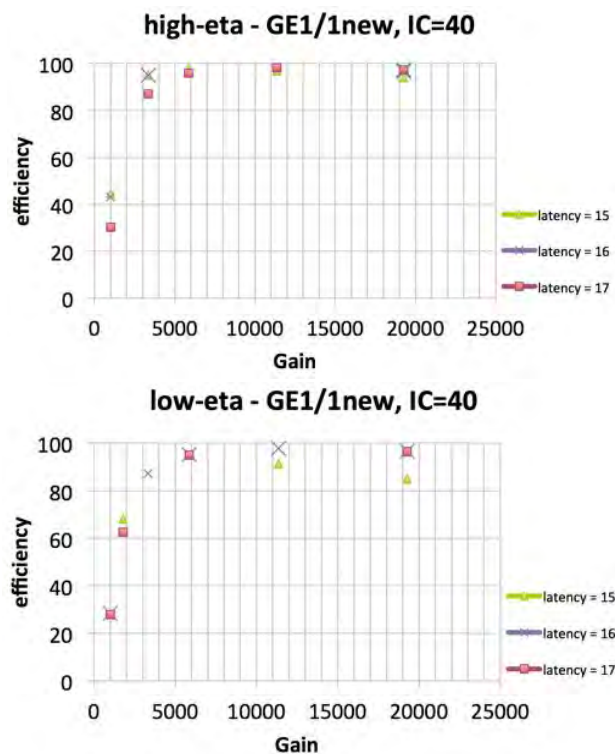


Figure 4.45: GE11_II efficiency performance in the high and low- η .

A remarkable result is the fact that GE11_II reaches full efficiency with a gain of ≈ 7000 : this is in agreement with previous results on small prototypes and indicates that the full-size detector is performing excellently; the operation at higher gain will

¹One VFAT threshold unit corresponds to a charge of $\approx 0.08\text{fC}$ at the input channel comparator stage.

ensure a very stable operation. Fig. 4.46 shows the cluster size and space resolution which actually confirm the very good efficiency curve.

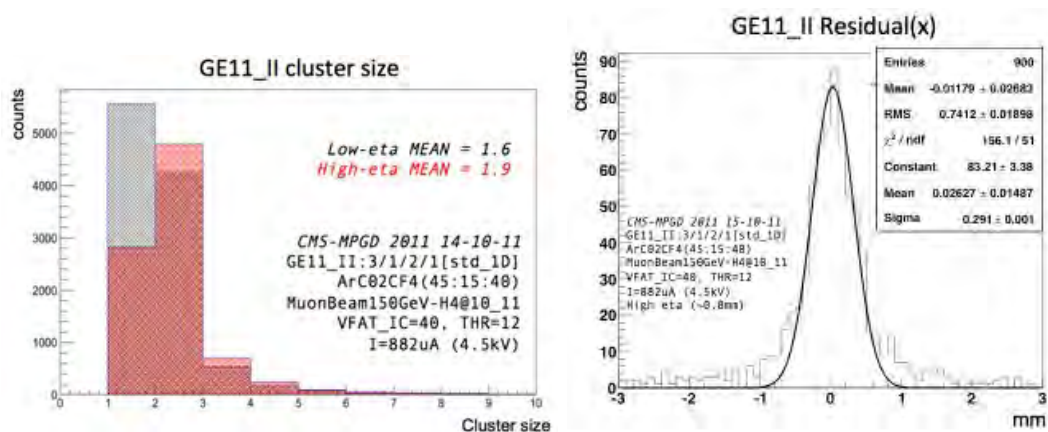


Figure 4.46: GE11.II performance: space resolution and cluster size in the high and low- η .

In one campaign also a strong magnetic field, was used in order to validate the detector in an environment similar to the CMS Endcap high- η . In the Fig. 4.47 and 4.48 measured clusters size and cluster displacement are shown. The cluster size doesn't seem to be affected by the magnetic field, while the signal induced on the strips is displaced due it. The measurement of this displacement is in good agreement with simulations performed with GARFIELD¹.

¹Garfield is a computer program, developed at CERN, originally for the detailed simulation of two and three dimensional with TPC, drift and (multi) wire counters. For many of 2D configurations, exact fields are known but this is not the case for three dimensional configurations, not even for seemingly simple arrangements like two crossing wires. Furthermore, dielectric media and complex electrode shapes are difficult to handle with analytic techniques. To handle such increasingly popular detectors, Garfield is interfaced with the *neBEM* program. Garfield also accepts two and three dimensional field maps computed by finite element programs such as *Ansys*, *Maxwell*, *Tosca*, *QuickField* and *FEMLAB* as basis for its calculations. The finite element technique can handle nearly arbitrary electrode shapes as well as dielectrics. [<http://garfield.web.cern.ch/garfield>]

4. BEYOND RPC, GAS ELECTRON MULTIPLIERS DETECTOR

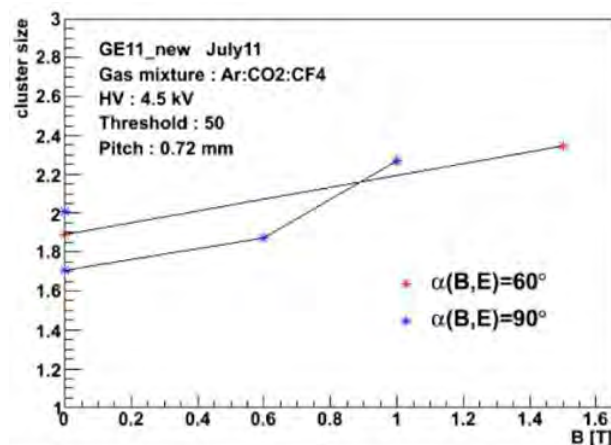


Figure 4.47: GE11_II performance inside a strong magnetic field: cluster size.

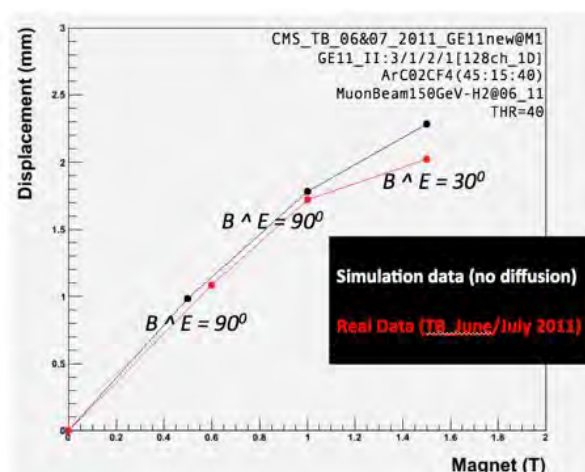


Figure 4.48: GE11_II performance inside a strong magnetic field: cluster's displacement due to the magnetic field.

In September 2011 the full-scale prototype GE11_II was tested again in H4 SPS beam line. This time the goal was to test the detector with the Scalable Readout System (SRS), provided by the RD51 Collaboration, and the APV¹ chips. During those tests the capability to measure spatial resolution, by pulse height information, was showed. Two small $10 \times 10\text{cm}^2$ GEM detectors (called TR_5 and TR_1) were used

¹The APV (Analog Pipeline Voltage Mode) is a $0.25\mu\text{m}$ CMOS analog asynchronous chip with 128 input channels. They feed signals into a low noise pre-amp followed by a CR-RC shaping amplifier. The signals are then converted to approximately 50ns wide voltage pulses with magnitudes of about 100mV per MIP.

to reconstruct the tracks in the same manner as it was previously done using the VFAT readout chip. Both these small detectors were running with Ar/CO₂ while the GE11_II was operated with Ar/CO₂/CF₄. To minimize the impact of beam divergences on the measurement the beam was set to be a $2 \times 2\text{mm}^2$ spot.

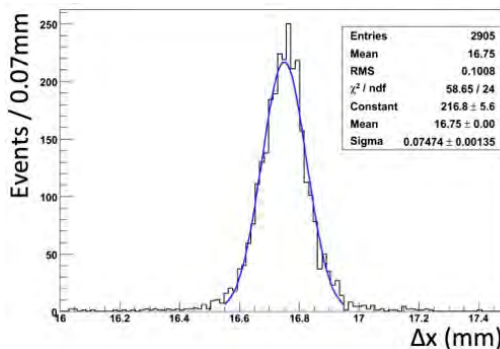


Figure 4.49: Δy distribution for TR_5 and TR_1 .

Assuming that both TR_5 and TR_1 , which share the same construction, have the same spatial resolutions ($\sigma_{y5} = \sigma_{y1}$) and that the beam divergence in y is negligible in the center, considering the Fig.4.49, we have for the width of the Δy distribution:

$$\sigma_{\Delta y}^2 = \sigma_{y5}^2 + \sigma_{y1}^2 = 2 \times \sigma_y^2 \quad (4.8)$$

$$\sigma_y = \frac{\sigma_{\Delta y}}{\sqrt{2}} = 53\mu\text{m} \quad (4.9)$$

Hit positions in x and y are computed from the mean (or center-of-gravity) of the corresponding strip cluster using analog pulse height information for each strip. It is a reasonable assumption that $\sigma_{x5} \approx 53\mu\text{m}$ if $\sigma_{y5} = 53\mu\text{m}$. Since in TR_5 strips in x and y have the same pitch, an upper bound on the spatial resolution of the GE11_II prototype can be established, in section with smallest strip pitch, achievable with analog pulse height information:

$$\sigma_{x_{GE11}} \leq \sqrt{\sigma_{\Delta x}^2 - \sigma_{x5}^2} \leq 103\mu\text{m} \quad (4.10)$$

The (4.10) gives an upper bound value, as any remaining beam divergences in x will still contribute to the width of the Δx distribution in Fig. 4.50.

4. BEYOND RPC, GAS ELECTRON MULTIPLIERS DETECTOR

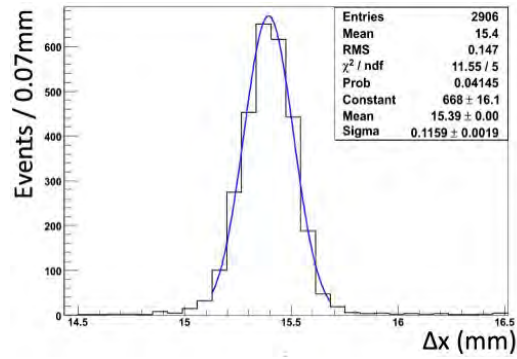


Figure 4.50: Δx distribution for TR_5 and GE11.II.

4.10 Summary and Conclusion

In summary, a full-size working detector with large dimensions $990\text{mm} \times (220 - 455)\text{mm}$ (active area) has been designed, built, and studied in several beam tests. This detector is actually the biggest ever build in the world and it has shown already excellent performance. Nowadays, the single-mask technique has matured as it profits from a very refined production process which permits careful control of the shapes and dimension of the holes. This technology is becoming very suitable even for industrial production, which would decrease cost.

In 2010 we have completed three beam tests at RD51 setup in the H4 beam line (SPS Preveessin), with small size prototypes; we demonstrated that the small prototypes are addressing the requested requirements in terms of high efficiency and gain, stable safe and reliable operation at LHC. From the electronic point of view, the detector plus the readout proved to work without any problem under simulated CMS LHC conditions. In 2011 we have run five beam periods; the goal was to test the detector performance inside a strong magnetic field (3T), the timing performance of the full-size prototype with optimized gas gap configuration and finally the testing of updated/new electronics compliant with the CMS system. The GE11.II detector was tested during several test beams showing very positive results. The GEMs for CMS collaboration made a significant improvement during the construction and the assembly of this second full-scale detector since it was challenging to build a large area GEM with transfer 1 and induction gap size of 1mm.

4. BEYOND RPC, GAS ELECTRON MULTIPLIERS DETECTOR

5

Conclusion

This thesis was focused in applied physics; this means to cope with many different engineering aspects with the goal of studying and improving devices, materials and in general equipments adopted in the high energy field. Thanks to a multidisciplinary approach we have found several original solutions to complete all measurement campaigns in different fields. In the beginning, concerning the RPC studies, we have established a long-term campaign with the target of a continue monitoring of gas and detector response variables; this activity involved hardware installation, software development and data-analysis, that is actually the full chain of a physics experiment, even if in a very reduced scale. On the other hand, concerning the material science, we have been working on a new detector, upgrading the RPC technology, using improved industrial processes which deliver more and more advanced materials. Exploiting advanced photolithographic processes we have used the state-of-art production, at CERN, to design, build and test a large-size GEM detector which represent the world's record for dimension and performances. We tested this chamber in several test beams, in several different conditions comparing real data with simulations and we have even upgraded the detector producing a second enhanced version with improved timing performance, a crucial factor for the CMS Experiment. This prototype detector, in fact, is taken under consideration for the upgrade of the CMS endcap high- η region; this is the perfect example as applied studies on technological aspects can have a huge impact on particle physics, since thanks to feasibility studies described in this thesis we have shown a possible instrumentation of the vacant area where, so far, no detector has been installed due to several concerns about the sustainability of a technology in that area.

5. CONCLUSION

Appendix A

RPC Appendix

A. RPC APPENDIX

The bakelite corporation was formed in 1922 from a merger of three companies: the General bakelite Company, which Baekeland had founded in 1910, the Condensite Company founded by J.W. Aylesworth, and the Redmanol Chemical Products Company founded by L.V. Redman(56). bakelite Limited was formed in 1926 from the amalgamation of three suppliers of phenol formaldehyde materials: the Damard Lacquer Company Limited of Birmingham; Mouldensite Limited of Darley Dale and Redmanol Chemical Products Company of London. In 1939 the company was acquired by the Union Carbide and Carbon Corporation. At the moment bakelite is not adopted anymore extensively, since new plastic materials have been developed, but in the recent past bakelite was widely used in several applications such as saxophone mouthpieces, whistles, cameras, solid-body electric guitars, rotary-dial telephones, machine guns, jewelry, desks, toys, thermal shield etc etc. Nowadays bakelite is manufactured and produced in sheet, rod and tube form for industrial applications, electronics, power generation and aerospace industries, and under a variety of commercial brand names. For what concerns the production and the composition of the bakelite the core is made by Phenolic sheet(57), a dense material which is built applying heat and pressure to layers of paper or glass cloth impregnated with synthetic resin. These layers are usually cellulose paper, cotton fabrics, synthetic yarn fabrics, glass fabrics or unwoven fabrics. When heat and pressure are applied to the layers, a chemical reaction (polymerization) transforms the layers into a high-pressure industrial laminated plastic. Phenol formaldehyde resins (PF), globally speaking are the result of the reaction between phenols and formaldehyde.

Formaldehyde(58), CH_2O , (IUPAC name Methanal) is the most common and simplest aldehyde precursor of several important polymers, in standard condition is a colorless gas.

In nature Formaldehyde (Fig. A.1) is mainly produced in the upper atmosphere¹ due to the action of the sunlight and oxygen on atmospheric methane and also from the combustion of carbon compounds. On the other hand Formaldehyde does not accumulate in the environment because it is broken by the sunlight. In industrial process Formaldehyde is produced by methanol oxidation instead of methane oxidation as in nature because this is much more difficult to happen. The methanol oxidation

¹Formaldehyde has been found even outside the Earth as the first organic compound detected outside our planet(59).

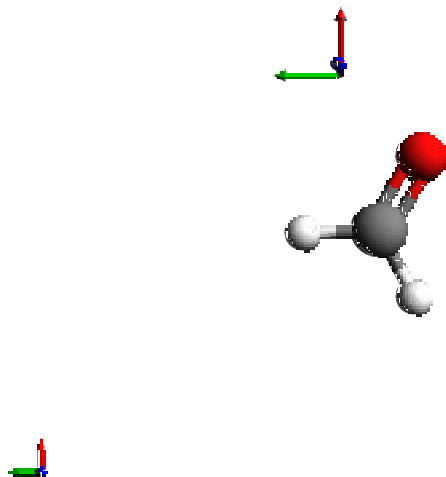


Figure A.1: Tridimensional structure of formaldehyde

is catalyzed by silver metal or a mixture of an iron and molybdenum or vanadium oxides. The process takes place between 250°C and 400°C, methanol and oxygen react in presence of iron oxide with molybdenum and/or vanadium (in case of silver-based catalyst the required temperature is 650°C:



Phenol (or carboic acid) is, in standard conditions, an organic solid and white crystalline organic mildly acidic compound with the chemical formula $\text{C}_6\text{H}_5\text{OH}$ and shown in Fig. A.2.

It was discovered in 1834, when it was extracted from coal tar, which remained the primary source until the development of the petrochemical industry. Phenol consists of a Phenyl (C_6H_5) group, bonded to a Hydroxyl (OH) group and it is produced industrially on a very large scale because it is fundamental for the production of other materials. Since Phenol is commercially very important industries have found several production processes. One of the main route involves the partial oxidation of Cumene (isopropylbenzene) via the Hock rearrangement(60):



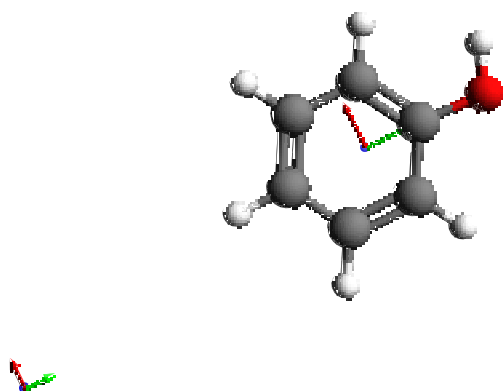


Figure A.2: Tridimensional structure of Phenol

Other methods use benzenesulfonate or chlorobenzene. The major uses of phenol involve its conversion to plastics or related materials by means of several condensation and hydrogenation process; few examples are condensation with acetone (bisphenol-A and polycarbonates), hydrogenation of phenol gives cyclohexanone (nylon), condensation with formaldehyde gives phenolic resins such as the bakelite which is detailed discussed here.

Phenol-formaldehyde resins are formed by a step-growth polymerization reaction that can be either acid- or base-catalysed. Since formaldehyde exists predominantly in solution as a dynamic equilibrium of methylene glycol oligomers, the concentration of the reactive form of formaldehyde depends on temperature and pH. Phenol is reactive towards formaldehyde at the ortho and para sites (sites 2, 4 and 6) allowing up to 3 units of formaldehyde to attach to the ring. The initial reaction in all cases involves the formation of a hydroxymethyl phenol:



The hydroxymethyl group is capable of reacting with either another free ortho or para site, or with another hydroxymethyl group. The first reaction gives a methylene bridge, and the second forms an ether bridge.

Phenolic bakelite is produced in dozens of commercial grades and with various additives to meet diverse mechanical, electrical and thermal requirements. When the molar ratio of formaldehyde to phenol is less than one the polymerization is performed by means of acid-catalysis. The produced resin is called Novolax. This is widely used in the photolithography process as photoresist. On the contrary when the molar mass of formaldehyde to phenol is greater the polymerization is performed by means of base-catalysis and the result is called Resol.

About the surfaces of the RPC bakelite, they are made of Melamine resin. Melamine is an organic thermosetting plastic material made from melamine and formaldehyde by polymerization. There are several kind of synthetic polymer obtained varying from very slow to very fast curing.

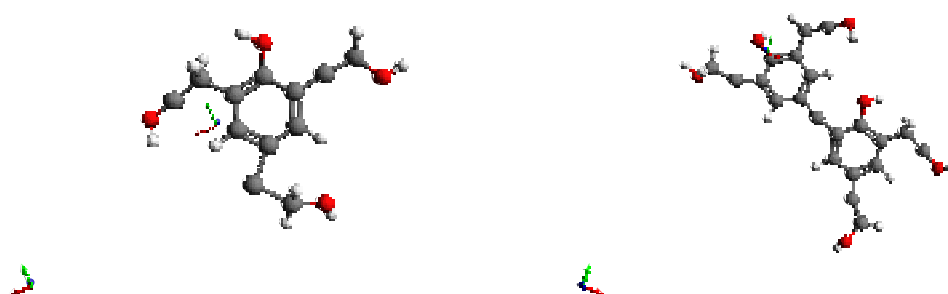


Figure A.3: Synthesis of bakelite a) b)

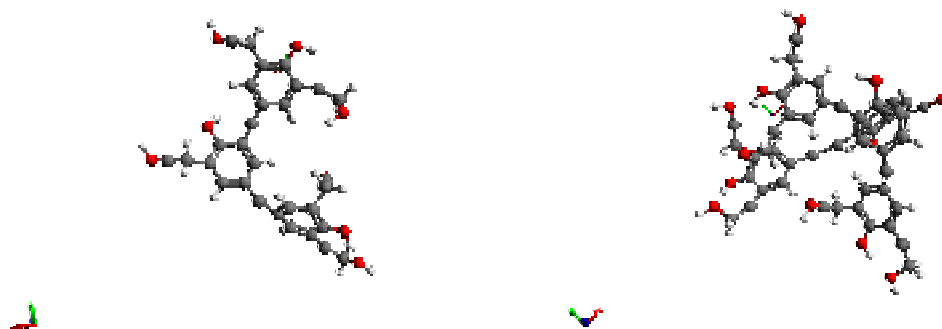


Figure A.4: Synthesis of bakelite c) d)

Melamine resin has a highly stable structure and is very versatile material that can be easily molded while warm.

Finally the RPC bakelite material is coated with Linseed oil in order to make smooth the inner surface in which the electrical field is applied. Linseed oil is a yellowish oil obtained from the dried ripe seeds of the flax plant¹. The oil is obtained by cold pressing, sometimes followed by solvent extraction. Linseed oil has the capability to polymerize into a solid form, and thanks to this peculiarity this oil does not need to be blended even if in several application this may help. Most applications of linseed oil exploit its drying properties, i.e. in the RPC bakelite preparation the initial material is liquid or at least pliable and the aged material is rigid but not brittle, moreover the water-repelling (hydrophobic) nature of the resulting hydrocarbon-based material is advantageous also because the RPC gas mixture contains 40% of relative humidity. Anyway commercially the use of linseed oil has declined over the past several decades with the increased use of synthetic alkyd resins, which are functionally similar but resist yellowing(61). From the chemical point of view the Linseed oil is an edible triglyceride², like other common fats. Linseed oil is distinctive in terms of fatty acid constituents of the triglyceride, which contain an unusually large amount of α -linolenic acid, which has a distinctive reaction toward oxygen in air. Specifically, the constituent fatty acids in a typical linseed oil are of the following types:

¹Linum usitatissimum, Linaceae.

²Linseed oil is generated from Glycerol and 3 fatty acid.

-
1. The triply unsaturated α -linolenic acid (51.9-55.2%);
 2. The triply unsaturated α -linolenic acid (51.9-55.2%);
 3. The monounsaturated oleic acid (18.5-22.6%);
 4. The doubly unsaturated linoleic acid (14.2-17%)

Having a high content of di-and triunsaturated esters, linseed oil is particularly susceptible to polymerization reactions upon exposure to oxygen in air. This polymerization, which is called "drying", results in the rigidification of the material. After this process it is still possible to modify the structure of the polymerized film by means of Oxidations (due to O₂ and light), interactions with metallic ions and hydrolysis of ester bonds. Globally the polymerized Linseed oil suffer the "aging effect" due to previous effects.

A. RPC APPENDIX

Appendix B

Radiation damage

B. RADIATION DAMAGE

The radiation damage concerns the interaction between particles and matter and the consequences of this interaction. Particles have a certain amount of energy; an Ionizing radiation (Fig. B.1) consists in one or more particles with energy high enough to detach electrons from atoms or molecules. Once the phenomenon takes place, since these ions have an excess of charge (negative or positive) because they were been ionized, they become chemically very reactive. These, so called, radicals tend to form molecules to stabilize their electronic structure.

The degree and nature of such ionization depends mostly on the energy of the individual particles (alpha, beta, photons, neutrons, muon..). In the absence of heating or multiple absorption of photons (a rare process), an intense flood of particles will not cause ionization if each particle does not carry enough individual energy to be ionizing. This is due to the fact that the minimum threshold energy to detach electrons is not reached and then there is no ionization process.

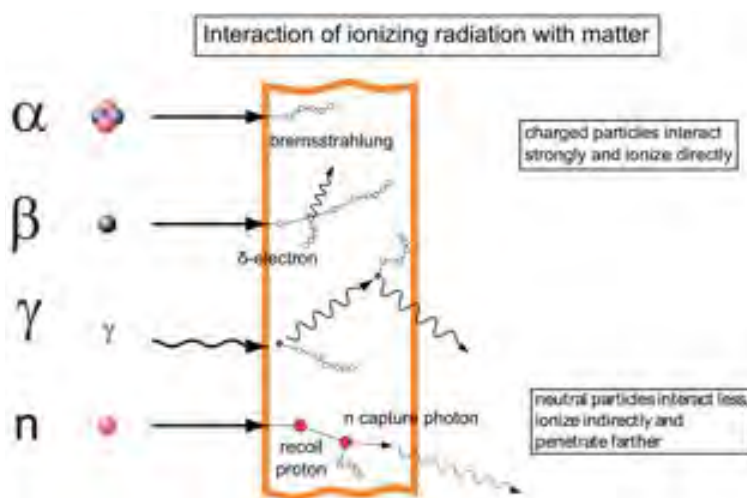


Figure B.1: Different ionizing radiations.

Ionizing radiations have several crucial effects on materials and devices, in particular the matter is deteriorated if submitted to high energy particle flux. Due to ionizing radiation the material may become radioactive, due to neutron activation; chemical bonds may be broken and cause de-polymerization, corrosion or physical change such as different electronic, optic or mechanical properties.

In electronics, ionizing radiations are utmost important because they provoke electrical breakdown in semiconductors with consequent irreversible damages. The term “radiation hard” was in fact invented to describe devices that may operate in ionizing environment such as High Energy Physics, Astrophysics, Nuclear Industry.

In gaseous particle detectors, radiation damage plays a very important role. The ageing factor is strongly correlated to the amount of ionizing radiation received by the detector itself. As discussed previously the free radicals generated during the Avalanche process may interact easily with detector’s materials inducing damages. For RPCs, for example the influence of fluorine can modify the detector behaviour interacting with bakelite surface where conductive compounds are collected depleting the electrical field locally.

B. RADIATION DAMAGE

Appendix C

ISR checklist

C. ISR CHECKLIST

Table C.1: ISR checklist - Chemical parameters

	Date	
	Time	
	Cycle Number	
	Phase Number	
ISR Env.		
	Temp. (°C)	
	RH (%)	
	P (mbar)	
Chemical		
	pH flask ₂ HV61, LiOH drops, Final pH	
	pH flask ₂ HV62, LiOH drops, Final pH	
	pH flask ₂ HV64, LiOH drops, Final pH	
	pH flask ₂ HV66, LiOH drops, Final pH	
	pH flask ₃ HV61, LiOH drops, Final pH	
	pH flask ₃ HV62, LiOH drops, Final pH	
	pH flask ₃ HV64, LiOH drops, Final pH	
	pH flask ₃ HV66, LiOH drops, Final pH	
	pH flask ₄ HV61, LiOH drops, Final pH	
	pH flask ₄ HV62, LiOH drops, Final pH	
	pH flask ₄ HV64, LiOH drops, Final pH	
	pH flask ₄ HV66, LiOH drops, Final pH	
	Flow HV61 (l/h)	
	Flow HV62 (l/h)	
	Flow HV64 (l/h)	
	Flow HV66 (l/h)	
Fresh Mix.		
	Total Flow (l/h)	
	C ₂ H ₂ F ₄ (%)	
	iC ₄ H ₁₀ (%)	
	SF ₆ (%)	
	Temp. (°C)	
	RH (%)	

Table C.2: ISR checklist - Rack parameters

CL mix			
	Temp. (°C), RH(%)		
	PT10, PT20		
	Stable p?, stop?		
Gas flow			
	A1, A2 (l/h)		
	A3, A4 (l/h)		
	A5, A6 (l/h)		
	A7, A8 (l/h)		
	A9, A10 (l/h)		
	HFC3, BUB98 (l/h)		
	FI1, FI2 (l/h)		
	FIC21, FIC22 (l/h)		
	FIC31, FIC34 (l/h)		
	PI30, PI99 (mbar)		
GC			
	He, Carrier (bar)		
	YV10 (run)		
	ZERO (at 0,240min)		
	AIR (at 0,320min)		
	SF ₆ (at 0,408min)		
	C ₂ H ₃ F ₃ (at 0,600min)		
	H ₂ O (at 0,636min)		
	C ₂ H ₂ F ₄ (at 0,643min)		
	iC ₄ H ₁₀ at 2,443min)		
	new peak?		
	HV83 (run)		
	AIR (at 0,320min)		
	SF ₆ (at 0,408min)		
	C ₂ H ₃ F ₃ (at 0,600min)		
	H ₂ O (at 0,636min)		
	C ₂ H ₂ F ₄ (at 0,643min)		
	iC ₄ H ₁₀ at 2,443min)		
	new peak?		

C. ISR CHECKLIST

Table C.3: ISR checklist - Chamber values

RPC CH			
	CH1 (kV), (μA)		
	CH2 (kV), (μA)		
	CH3 (kV), (μA)		
	CH4 (kV), (μA)		
	CH5 (kV), (μA)		
	CH6 (kV), (μA)		
	CH7 (kV), (μA)		
	CH8 (kV), (μA)		
	CH9 (kV), (μA)		
	CH10 (kV), (μA)		
	CH11 (kV), (μA)		
	CH12 (kV), (μA)		
	CH13 (kV), (μA)		
	CH14 (kV), (μA)		
	CH15 (kV), (μA)		
	CH16 (kV), (μA)		
	CH17 (kV), (μA)		
	CH18 (kV), (μA)		
	CH19 (kV), (μA)		
	CH20 (kV), (μA)		
	CH21 (kV), (μA)		
	CH22 (kV), (μA)		

Appendix D

RPC performance during the ISR data-taking

D. RPC PERFORMANCE DURING THE ISR DATA-TAKING

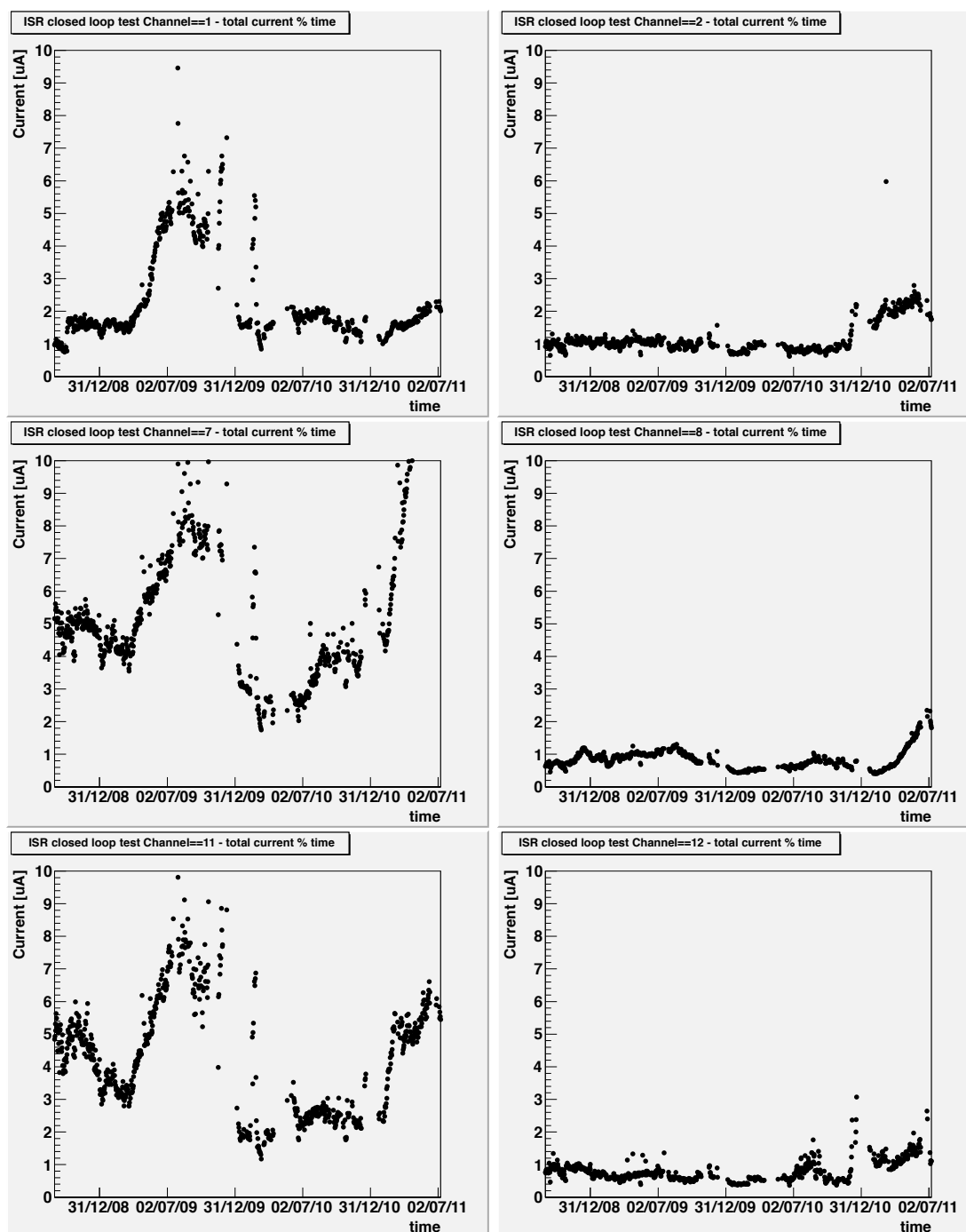


Figure D.1: Anodic total current Channels 1, 2, 7, 8, 11, 12 in CL during run 1 and 2.

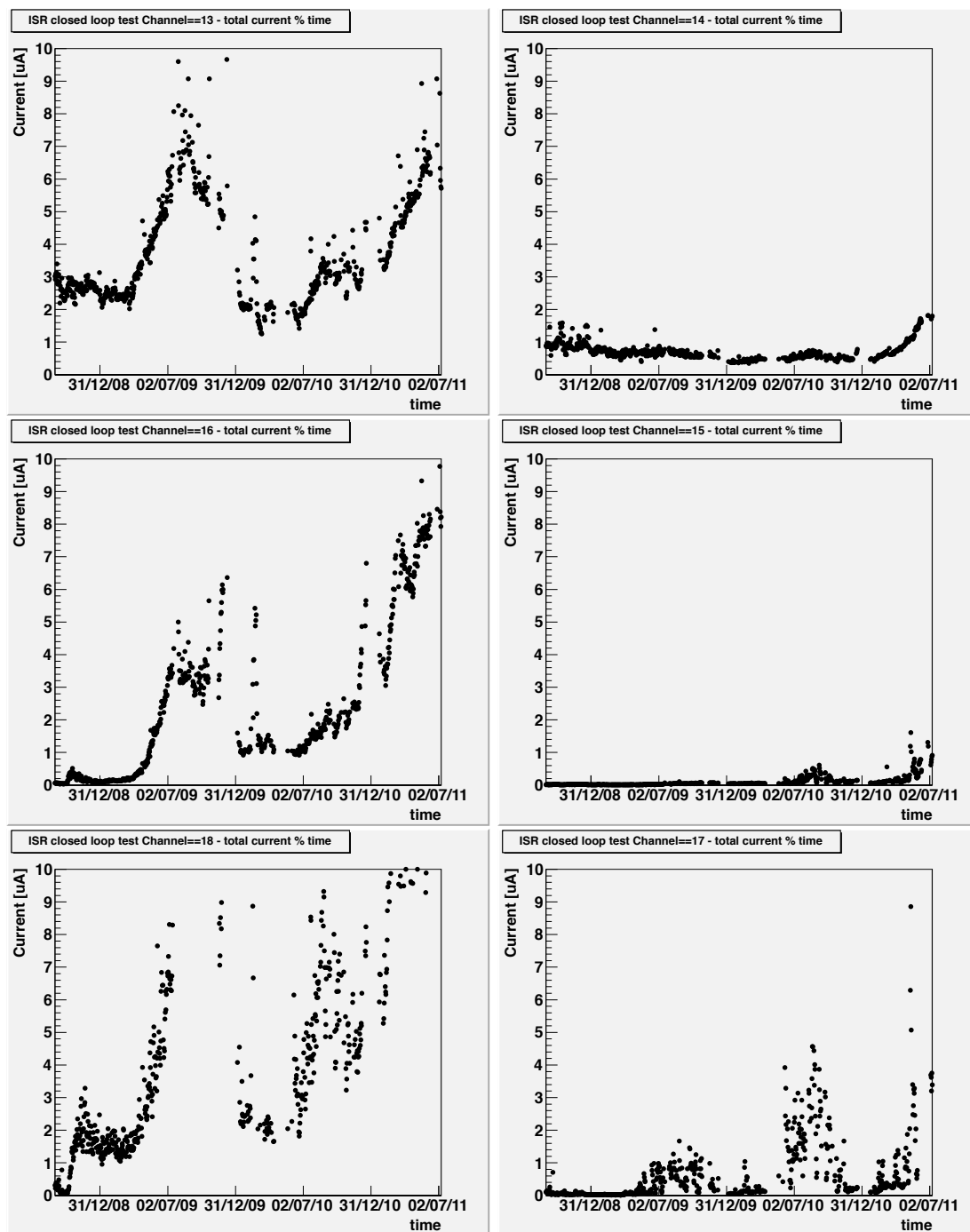


Figure D.2: Anodic total current Channels 13, 14, 15, 16, 17, 18 in CL during run 1 and 2.

D. RPC PERFORMANCE DURING THE ISR DATA-TAKING

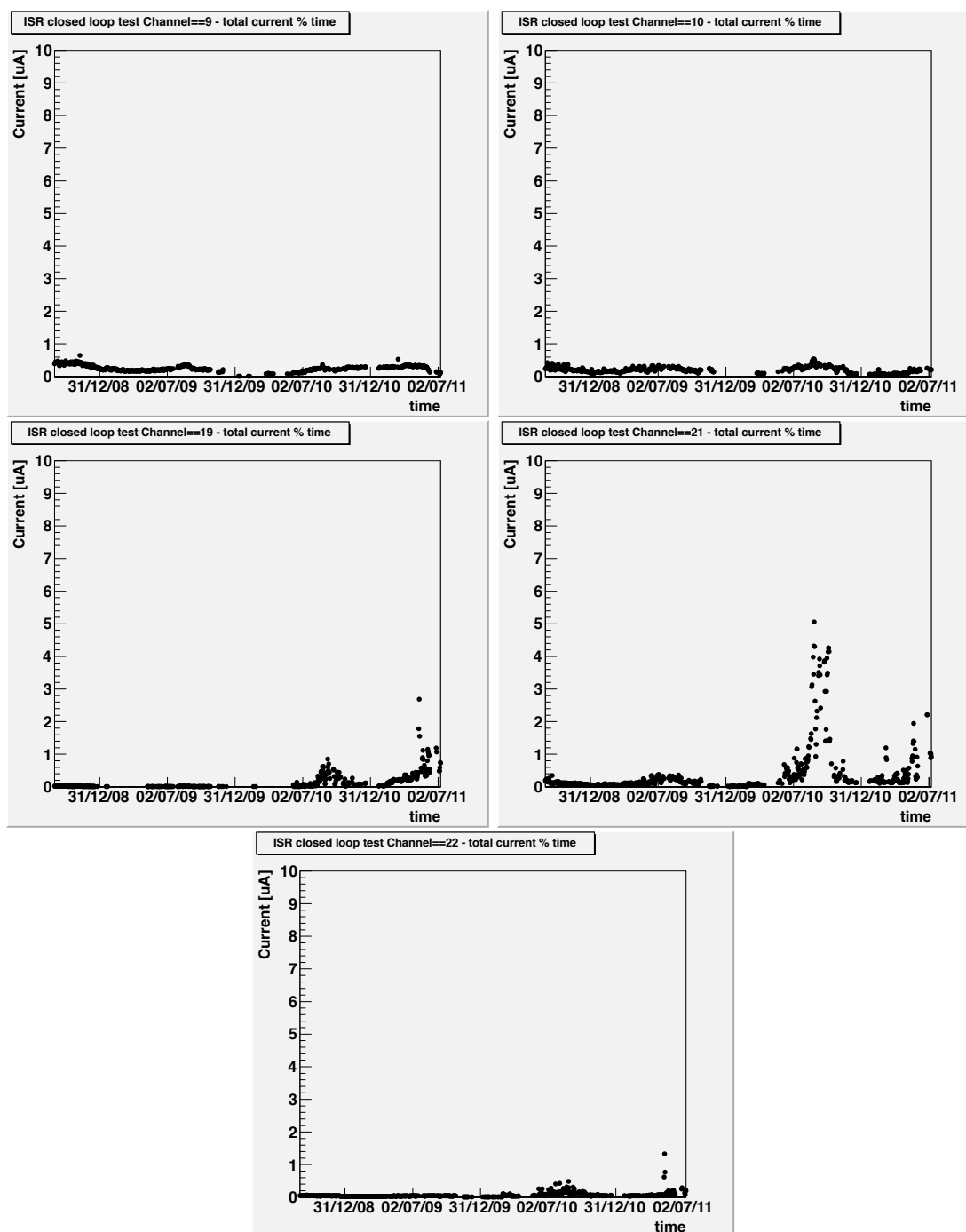


Figure D.3: Anodic total current Channels 9, 10, 19, 21, 22 in OL during run 1 and 2.

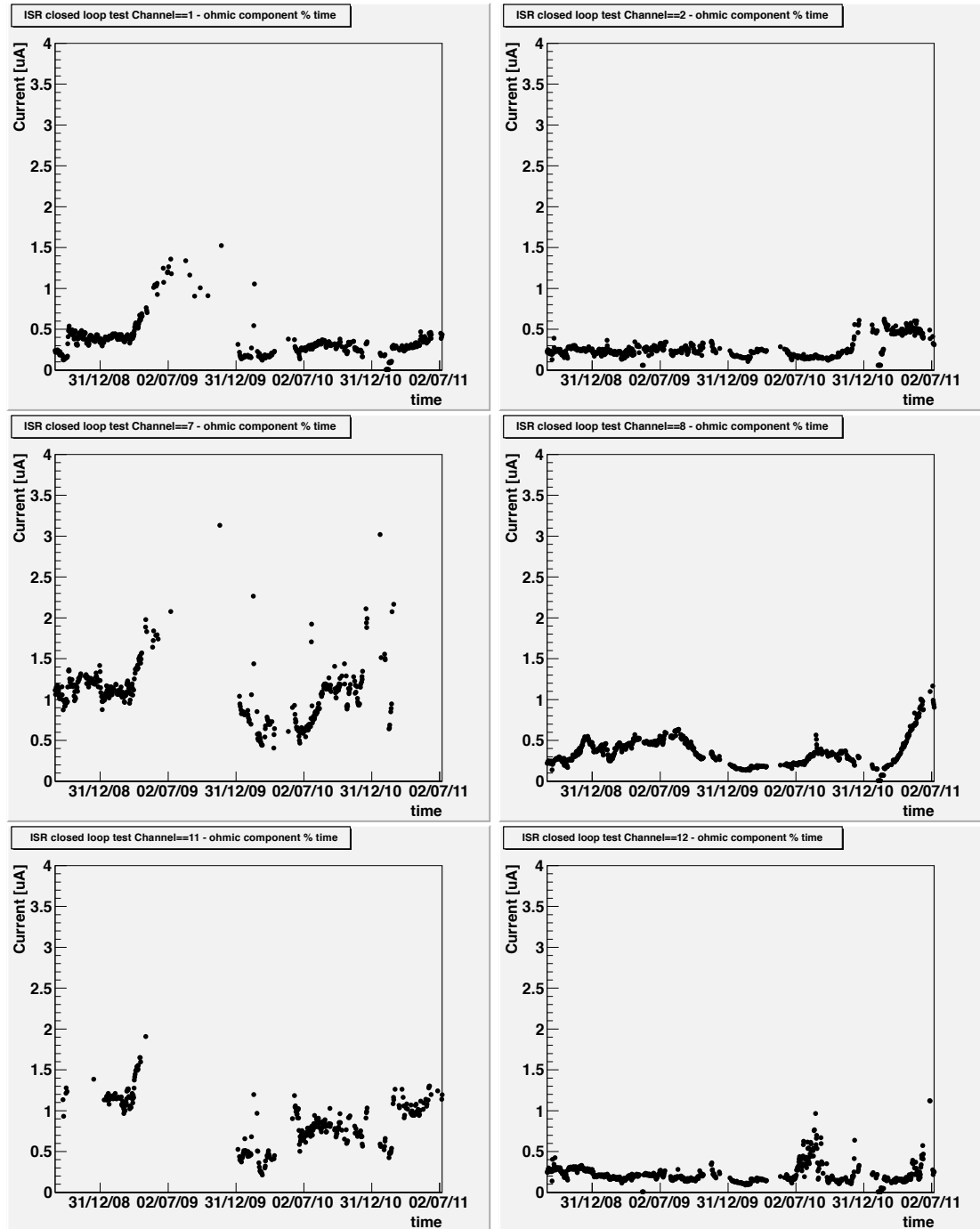


Figure D.4: Ohmic current Channels 1, 2, 7, 8, 11, 12 in CL during run 1 and 2.

D. RPC PERFORMANCE DURING THE ISR DATA-TAKING

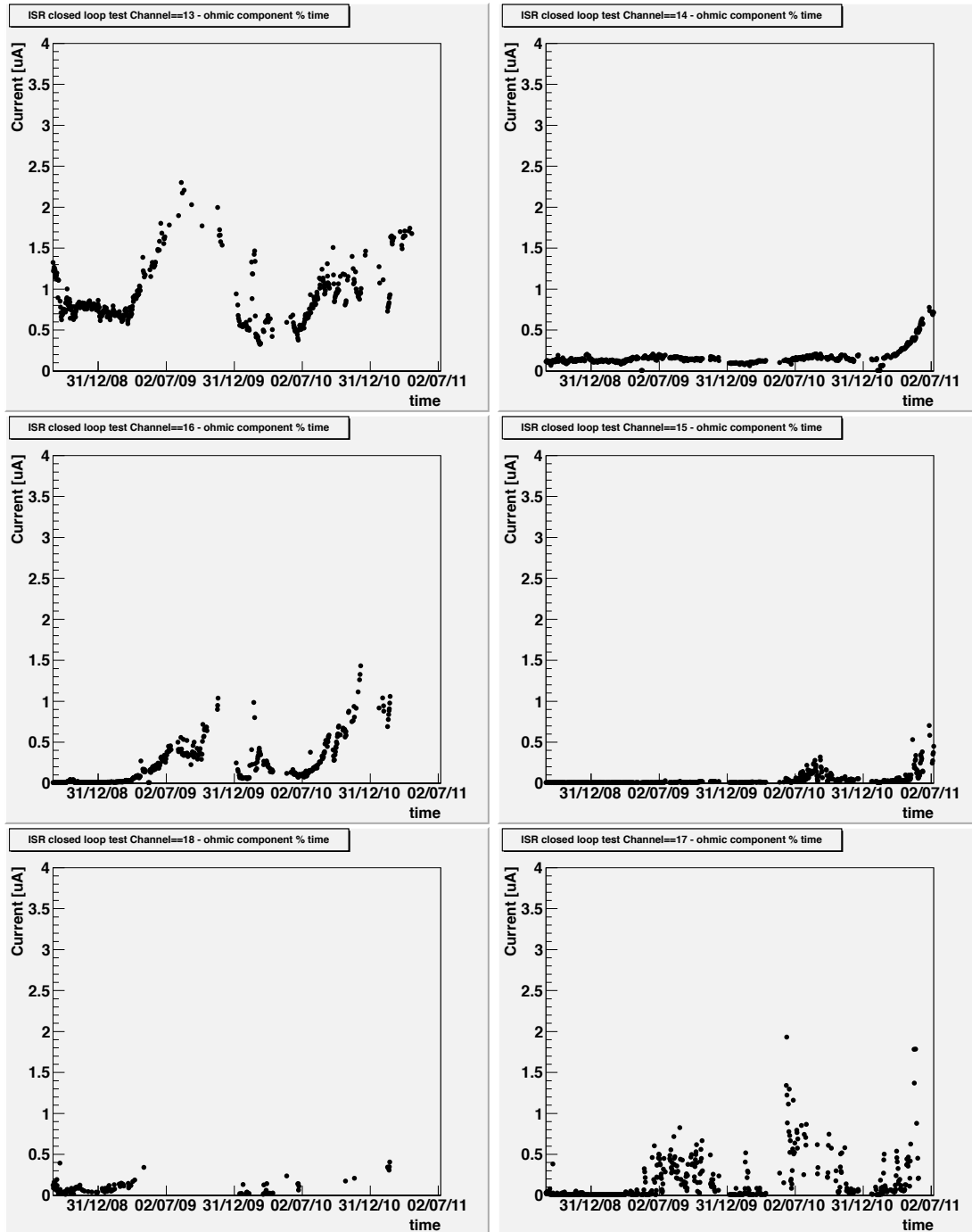


Figure D.5: Ohmic current Channels 13, 14, 15, 16, 17, 18 in CL during run 1 and 2.

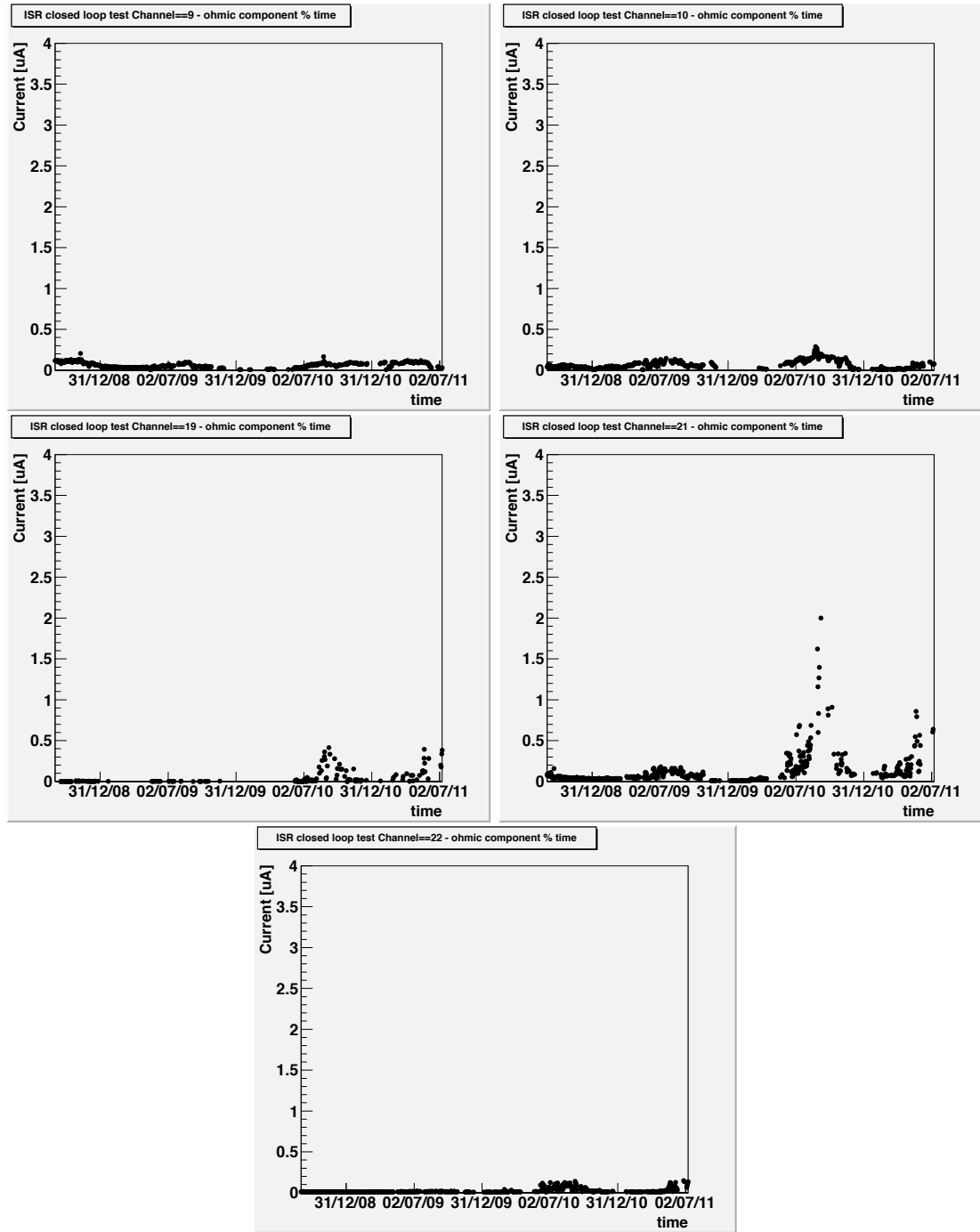


Figure D.6: Ohmic current Channels 9, 10, 19, 21, 22 in OL during run 1 and 2.

D. RPC PERFORMANCE DURING THE ISR DATA-TAKING

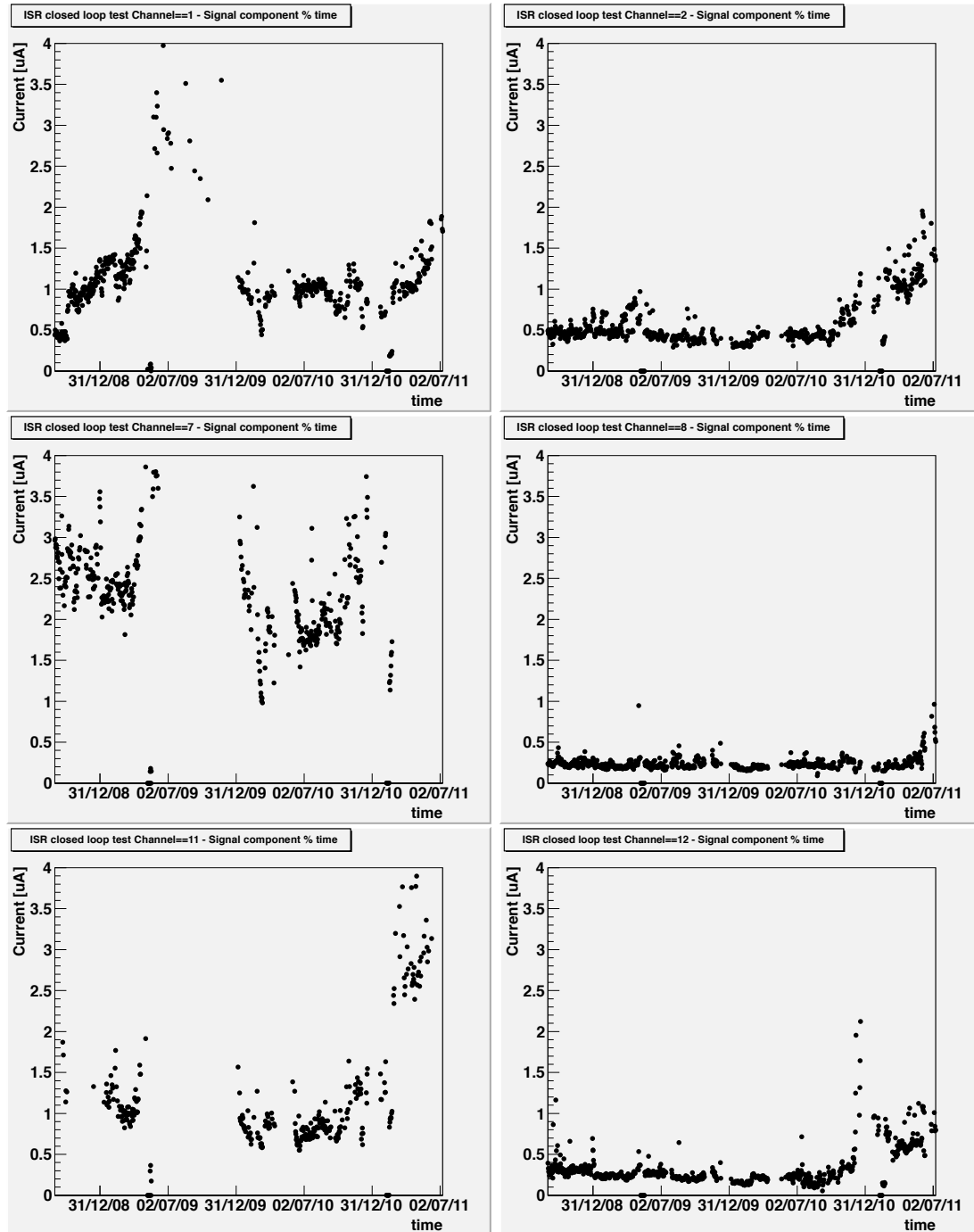


Figure D.7: Signal current Channels 1, 2, 7, 8, 11, 12 in CL during run 1 and 2.

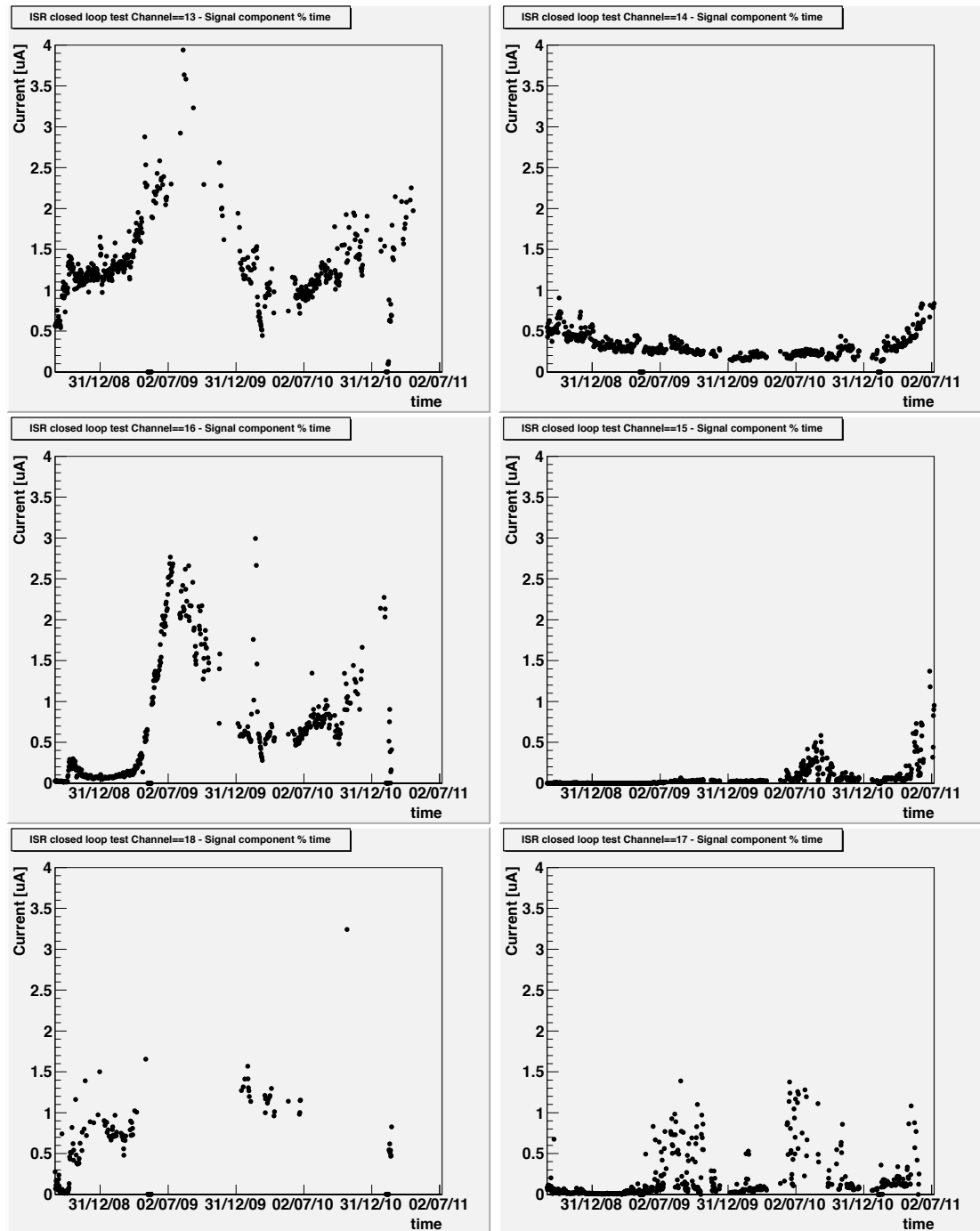


Figure D.8: Signal current Channels 13, 14, 15, 16, 17, 18 in CL during run 1 and 2.

D. RPC PERFORMANCE DURING THE ISR DATA-TAKING

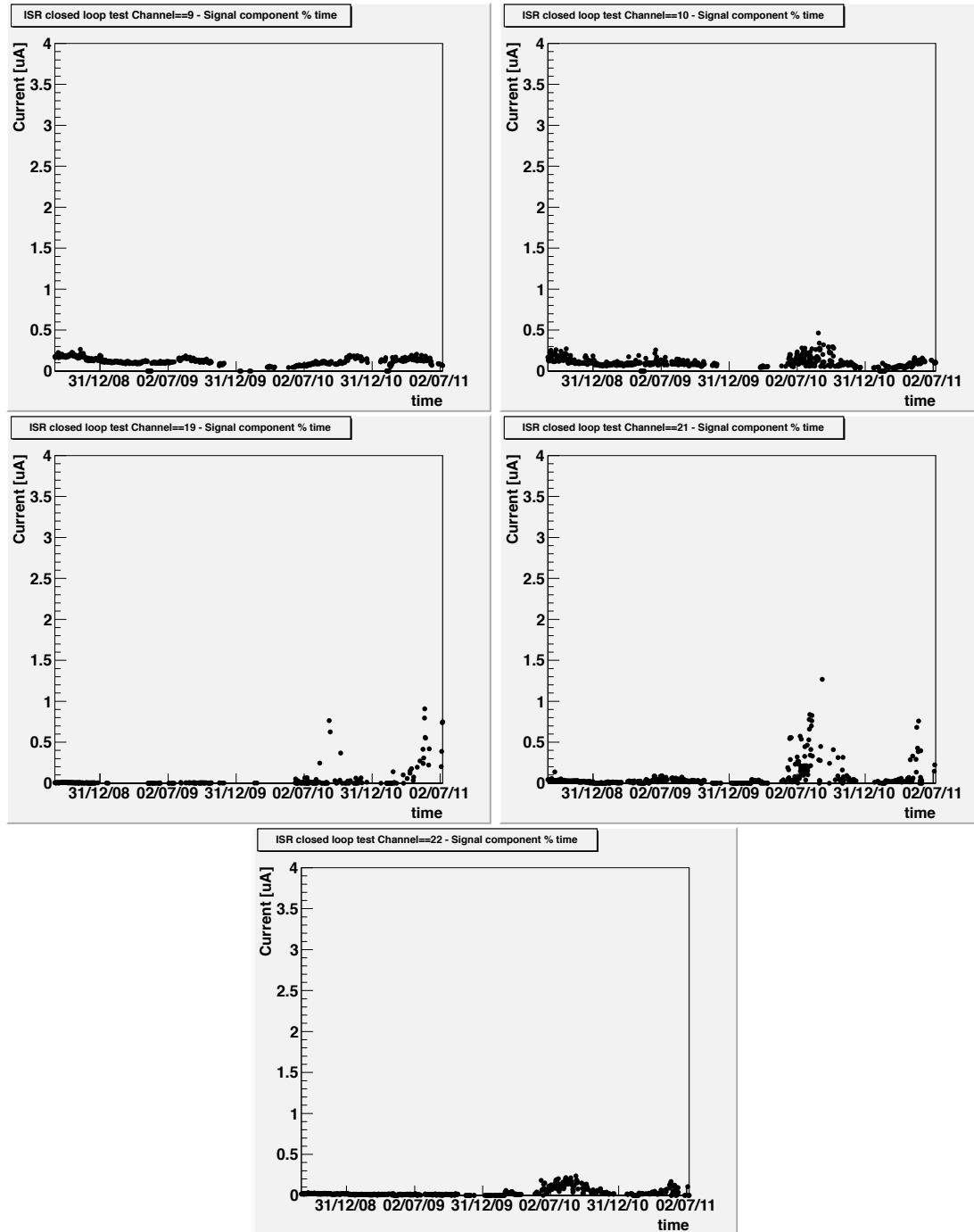


Figure D.9: Signal current Channels 9, 10, 19, 21, 22 in OL during run 1 and 2.

References

- [1] CMS Collaboration, "The CMS experiment at the CERN LHC", *JINST* **3** (2008) S08004. 2, 24
- [2] R. Santonico, "RPC: Status and perspectives", *In *Pavia 1993, Proceedings, The resistive plate chambers in particle physics and astrophysics* 1-11*. 10
- [3] CMS Collaboration, "The CMS muon project: Technical Design Report", CERN-LHCC-97-032 ; CMS-TDR-003. Geneva, CERN, 1997. 12
- [4] The ATLAS Collaboration, G. Aad *et al.*, The ATLAS Experiment at the CERN Large Hadron Collider , *JINST* **3** (2008) S08003. 12
- [5] G. D'Alì Staiti [ARGO-YBJ Collaboration], "The ARGO-YBJ experiment in Tibet," *Nucl. Instrum. Meth. A* **588** (2008) 7. 12
- [6] P. Fonte, "Applications and New Developments in Resistive Plate Chambers", *IEEE Transactions on Nuclear Science*, vol. 49, no. 3, June 2002. 12
- [7] M. Abbrescia *et al.*, "Effect of the linseed oil surface treatment on the performance of resistive plate chambers," *Nucl. Instrum. Meth. A* **394** (1997) 13. 13
- [8] J. Va'vra, "Physics and chemistry of aging: Early developments," *ICFA Instrum. Bull.* **24**, 1 (2002) *Nucl. Instrum. Meth. A* **515**, 1 (2003). 16
- [9] J. Va'vra, "Summary of session 6: Aging effects in RPC detectors," *Nucl. Instrum. Meth. A* **515**, 354 (2003). 16
- [10] R. Santonico and R. Cardarelli, "Development Of Resistive Plate Counters", *Nucl. Instrum. Meth.* **187** (1981) 377. 24
- [11] M. Bosteels *et al.*, "CMS Gas System Proposal", CMS Note 1999/018. 24
- [12] L. Besset, F. Hahn, S. Haider, C. Zinoni, "Experimental Tests with a Standard Closed Loop Gas Circulation System", CMS Note 2000/040. 24
- [13] M. Abbrescia *et al.*, "Gas analysis and monitoring systems for the RPC detector of CMS at LHC," LNF-06-34-P, LNF-04-25-P, Jan 2007. 9pp. Presented by S. Bianco on behalf of the CMS RPC Collaboration at the 2006 IEEE Nuclear Science Symposium (NSS), Medical Imaging Conference (MIC) and 15th International Room Temperature Semiconductor Detector Workshop, San Diego, California, 29 Oct - 4 Nov 2006. arXiv:physics/0701014. 24
- [14] M. Abbrescia *et al.*, "Proposal for a Systematic Study of the CERN Closed Loop Gas System Used by the RPC Muon Detectors in CMS", Frascati preprint LNF-06/27(IR), available at <http://www.lnf.infn.it/sis/preprint/> . 24
- [15] G. Saviano *et al.*, "Materials studies for the RPC detector in CMS ", presented at the RPC07 Conference, Mumbai (India), January 2008. 24
- [16] Manufactured by ZEOCHEM AG, Seestrasse 108, 8708 Uetikon (Germany). 28, 36
- [17] BASF Technical Bulletin. 28, 29, 36, 37
- [18] LEUNA Data Sheet September 9, 2003, Catalyst KL6526-T. 29, 36
- [19] S. Bianco *et al.*, " Chemical analyses of materials used in the CMS RPC muon detector", CMS NOTE 2010/006. 35
- [20] C.A.E.N. Costruzioni Apparecchiature Elettroniche Nucleari S.p.A. Via Vetraria 11 - 55049 Viareggio (Italy). 36
- [21] GRACE Davison Molecular Sieves data sheet. 36
- [22] LINDE Technical Bulletin. 36
- [23] Hanna Instruments, 584 Park East Drive, Woonsocket - Rhode Island 02895 (USA). 44
- [24] T. Greci, "Studio dei materiali utilizzati nel rivelatore di Muoni dell'esperimento CMS all'LHC collider di Ginevra." 57
- [25] A. Sharma,"Summary of RPC 2007 IX International Workshop", *Nucl. Instr. and Meth. A* **602** (2009), doi:10.1016/j.nima.2008.12.240. 58
- [26] Z. Malter, *Phys. Rev.* **50**, 48 - 58 (1936) 59
- [27] L. Benussi *et al.*, "The CMS RPC gas gain monitoring system: an overview and preliminary results", *Nucl. Instrum. Meth. A* **602** (2009) 805 [arXiv:0812.1108 [physics.ins-det]]. 61
- [28] M. Abbrescia *et al.*, "Cosmic ray tests of double-gap resistive plate chambers for the CMS experiment," *Nucl. Instrum. Meth. A* **550**, 116 (2005). 67
- [29] L. Benussi *et al.*, "Sensitivity and environmental behavior of the CMS RPC gas gain monitoring system," *JINST* **4** (2009) P08006 [arXiv:0812.1710 [physics.ins-det]]. 69
- [30] P. Darnell, "C : a software engineering approach", New York, NY : Springer, 1991. 69
- [31] R. Moser and L. Orsini, "TriDAS Trigger and Data Acquisition for CMS Experiment", developed at CERN in 2005. 70
- [32] Pico Technology, St Neots Cambridgeshire PE19 8YP, (UK) 71
- [33] S. Colafranceschi, SVN repository for GGM: "https://svn.cern.ch/repos/cmsrpcgmm", latest version available January 2011. 72
- [34] K. Doroud *et al.*, *Nucl. Instrum. and Meth. A* **602** (2009) 723-726. 78

REFERENCES

- [35] M. De Vincenzi *et al.*, Nucl. Instrum. and Meth. A **508** (2003) 94-97. 78
- [36] M. Bianco *et al.*, Nucl. Instrum. and Meth. A **602** (2009) 700-704. 78
- [37] L. Benussi *et al.*, "A new approach in modeling the behavior of RPC detectors" CMS NOTE 2010/076. 78
- [38] W. S. McCulloch, W. Pitts, "A logical calculus of the ideas immanent in nervous activity", Bulletin of Mathematical Biophysics **5** (1943) 115. 79
- [39] K. Hornik, M. Stinchcombe and H. White, "Multilayer Feedforward Networks are Universal Approximators?", Neural Networks, vol. 2, pp. 359, 1989. 79
- [40] S. Bose *et al.*, Nucl. Instr. and Meth. A **602** (2009) 839. 91
- [41] S. Biswas *et al.*, Nucl. Instr. and Meth. A **604** (2009) 310. 91
- [42] S. Biswas *et al.*, Nucl. Instr. and Meth. A (2009), doi:10.1016/j.nima.2009.06.076. 91, 94
- [43] F. Sauli, "GEM: A new concept for electron amplification in gas detectors", Nucl. Instrum. Meth. A **386**, 531 (1997). 98, 99
- [44] M. Villa *et al.*, "Progress on large area GEMs (VCI 2010)", arXiv:1007.1131 [physics.ins-det]. 99, 113
- [45] G. Antchev *et al.*, "The TOTEM detector at LHC," Nucl. Instrum. Meth. A **617** (2010) 62. 101, 121
- [46] A. A. Alves *et al.* [LHCb Collaboration], "The Lhcb Detector At The Lhc," JINST **3** (2008) S08005. 101
- [47] D. Abbaneo *et al.*, "Construction of the first full-size GEM-based prototype for the CMS high- η muon system," Nuclear Science Symposium Conference Record (NSS/MIC), 2010 IEEE, 10.1109/NSSMIC.2010.5874107 101
- [48] Dassault Systemes 900 Chelmsford Street Tower 2, 5th Floor Lowell, MA 01851 - United States. 103
- [49] D. Abbaneo *et al.*, "Characterization of GEM Detectors for Application in the CMS Muon Detection System", Nuclear Science Symposium Conference Record (NSS/MIC), 2010 IEEE proceeding, 10.1109/NSSMIC.2010.5874006 106, 127
- [50] M. Staib *et al.*, "Thermal Stretching of Large-Area GEM Foils Using an Infrared Heating Method", RD51 Technical Note in preparation, Nov 2010. 109
- [51] NEW FLEX TECHNOLOGY CO.,LTD. 306B-4L,BANWOL IND. COM.,1055,SINGIL-DONG, DANWON-GU, ANSAN-SI, GYEONGGI-DO; Ansan Danwon-gu; GYEONGGI-DO; 425839 111
- [52] D. Abbaneo *et al.*, "Gas Flow Simulations for gaseous detectors", contribution to N48-234 to this conference 113
- [53] P. Aspell *et al.*, "The VFAT production test platform for the TOTEM experiment". 114, 121
- [54] G. Bencivenni, "The GEM detector activity at the Frascati Laboratory", Nucl. Phys. A **827** (2009) 614C. 116
- [55] M. Alfonsi *et al.*, "Fast triggering of high-rate charged particles with a triple-GEM detector", Nucl. Instrum. Meth. A **535**, 319 (2004). 117
- [56] Twenty-Five Years of Chemical Engineering Progress, American Institute of Chemical Engineers Staff (1977). Ayer Publishing, pp. 216. ISBN 0836901495. 144
- [57] Wolfgang Hesse "Phenolic Resins" in Ullmann's Encyclopedia of Industrial Chemistry, 2002, Wiley-VCH, Weinheim. doi:10.1002/14356007. 144
- [58] "Formaldehyde - Compound Summary". The PubChem Project. USA: National Center of Biotechnology Information. 144
- [59] Mangum, Jeffrey G.; Darling, Jeremy; Menten, Karl M.; Henkel, Christian (2008), "Formaldehyde Densitometry of Starburst Galaxies", Astrophys. J. **673** (2): 83246, doi:10.1086/524354. 144
- [60] Manfred Weber, Markus Weber, Michael Kleine-Boymann "Phenol" in Ullmann's Encyclopedia of Industrial Chemistry 2004, Wiley-VCH. doi:10.1002/14356007. 145
- [61] F. Jones (2003), "Alkyd Resins", doi:10.1002/14356007. 148

Abstract

This thesis lays its foundation in both technological and theoretical studies carried out between several aspects of applied engineering. There are several original contributions within the material science. The first is the detailed studies about the CMS RPC gas filters, which required an intense 3 years data-taking and ended up with a complete characterization of purifier materials. On top of this a stable *ad – hoc* setup (GGM) has been developed for the CMS Experiment in order to monitor the RPC muon chamber working point. Finally a complete new detector has been designed, build and tested using new technology and new electronics establishing the word's record in size for this kind of detector, which is taken under consideration for the upgrade of the high- η region of the CMS Experiment.

Acknowledgements

I would like to acknowledge all the people who have helped me during these intense years.

Pour commencer je dois dire que cette thèse a été écrite grâce à l'amour et la patience de ma femme qui m'a donné l'inspiration et la force pour accomplir ce travail.

Then, I am indebted to my supervisors Stefano Bianco, Giovanna Saviano and Archana Sharma for their close support. Stefano Bianco at Frascati has thought me to get by in this world...of physicists. Giovanna Saviano has always supported my studies being my reference point at Università' la Sapienza; thanks to her charm and strong motivation I have learnt several lessons that were indispensable for this thesis.

A very big special thanks to Archana Sharma, my most important reference point at CERN: she has guided me since the beginning (actually many years ago..), teaching me life's lessons and providing always a strong help and a real support. This has been surely the most exciting time I could have ever desired.

Within the CERN group, I am really grateful to several people, starting from Duccio Abbaneo who has firmly supported me, making this thesis possible.

At CERN I had the possibility to be engaged in some International Collaborations: CMS-RPC, RD51 and GEMs. I cherish the memory of all the teamwork done together, especially during intense periods such as those of test beams!

Grazie inoltre alla mia famiglia che mi ha dato gli strumenti di base e trasmesso la curiosità di sapere.

Un grande grazie a tutti gli amici, di Roma, di Ginevra e della Normandia
per la loro amicizia che ha riempito tanti momenti importanti della vita.

Geneve,
February 16, 2012

Index

- adc, 66, 71
- avalanche, 54, 58, 67, 68
- bakelite, 12, 13, 15, 16, 18, 19, 24, 29, 45, 57, 61, 91, 94, 144, 146
 - applications, 144
 - Corporation, 144
 - fluorine, 153
 - grades, 147
 - Linseed oil, 57, 148
 - Novolax, 147
 - resol, 147
 - RPC surface, 147
 - silicon coating, 91
 - surface defects, 57
- carbolic acid
 - see Phenols, 145
- Closed Loop, 16, 18
 - Checklist, 43
 - checklist, 159
 - Chemical analysis, 31
 - data-taking, 46
 - Filter regeneration, 43
 - Fluorine monitoring, 41
 - Particulate filters, 52
 - Purifiers, 36
- CMS, 6, 9, 10, 12, 14–18, 24, 29, 37, 61, 62, 70, 72, 78, 80, 90, 92
 - Barrel, 11, 14, 104
 - commissioning, 97
 - conceptual design, 2
 - detector, 10
 - Endcap, 10, 11, 104
 - Experiment, 13, 17
 - filters, 18
 - Forward region, 104
 - gas system, 62
 - GE11, 120
 - GGM, 61
 - Muon system, 97, 103
 - RPC, 22
 - RPC chambers, 14
- electronics
 - APV, 136
 - GGM readout, 63
 - VFAT, 114, 116, 117, 121, 130, 134
- fluorine, 13, 16
- formaldehyde, 24, 146
 - natural, 144
- freon
 - see tetrafluoroethane, 13

- GEM
- foil stretching, 109, 110, 116, 118
 - Full-scale prototypes performances, 131
 - GE1/1 CAD view, 113
 - GE1/1 HV divider, 117
 - GE1/1 stretching, 115
 - Honeycomb-GEM, 109
 - Korean-GEM, 111
 - Magnetic field, 121
 - NS2-GEM, 110
 - SingleMask-GEM, 108
 - Small prototypes performances, 127
 - Test beam setup, 120
 - timing-GEM, 107
- GGM
- ADC, 64
 - ADC distribution, 66
 - anodic charge, 80
 - DST, 70
 - Environmental control, 71
 - HV feedback, 76
 - PVSS, 72
 - Sensitivity, 67
 - Single gap efficiency, 67
 - Software development, 69
 - XDAQ, 70
- honeycomb
- GEM frame, 116
 - GEM spacers, 109
 - muon-grapy, 130
- Hydroxyl
- group, 145
- hydroxymethyl, 146
- ionizing radiation, 152
- effects, 152
 - neutron activation, 152
 - radicals, 152
- isobutane, 13, 91
- ISR, 24, 29, 30, 92–94
- experimental setup, 24
- Kapton, 99
- LHC, 5, 12, 14
- Linseed oil, 148
- linoleic acid, 148
 - polymerization, 149
 - triunsaturated esters, 149
- Magnet
- Beam Test, 121
- mask
- double, 101, 106, 113, 128, 129
 - photolithography, 101
 - single, 101, 108, 109, 113, 114, 121, 123, 125, 128, 129, 139
- Melamine
- resin, 147, 148
- Methanal
- see formaldeide, 144
- methane
- oxidation, 144
- methanol, 144
- oxidation, 144
- methylene, 146
- glycol oligomers, 146

INDEX

- Muon System
 - see CMS, 11
- Neural Network, 78, 79, 90
- phenol
 - formaldehyde, 144, 146
 - formaldehyde molar mass ratio, 147
 - hydroxymethyl, 146
 - plastic conversion, 146
- phenolic
 - bakelite, 147
 - resin, 146
 - sheet, 144
- Phenyl
 - group, 145
- photolithography, 101, 147
- polymerization
 - step-growth, 146
- polyimide, 99, 101
- radicals
 - see ionizing radiation, 152
- resistivity, 29
- RPC, 9–18, 24, 35, 36, 39, 44, 48, 61, 62,
70–72, 78, 80, 90, 91, 93, 94, 101
 - charge, 80
 - gas mixture, 148
 - ionizing radiation, 153
 - Neural Network approach, 78
 - working principle, 12
- streamer, 58, 67, 68
- tetrafluoroethane, 91
- tracker
 - GEM, 131
- Zeolite, 25, 27, 38, 50, 51
 - designing, 27
 - natural, 27
 - porous structure, 25
 - synthetic, 27